

Two-photon calcium imaging of neocortical projection neurons in whisker somatosensory cortex during goal-directed sensorimotor learning

THÈSE N° 8922 (2018)

PRÉSENTÉE LE 16 OCTOBRE 2018
À LA FACULTÉ DES SCIENCES DE LA VIE
LABORATOIRE DE TRAITEMENT SENSORIEL
PROGRAMME DOCTORAL EN NEUROSCIENCES

ÉCOLE POLYTECHNIQUE FÉDÉRALE DE LAUSANNE

POUR L'OBTENTION DU GRADE DE DOCTEUR ÈS SCIENCES

PAR

Dimitra Angeliki VAVLADELI

acceptée sur proposition du jury:

Prof. B. D. McCabe, président du jury
Prof. C. Petersen, directeur de thèse
Prof. A. Holtmaat, rapporteur
Dr L. Bourdieu, rapporteur
Prof. J. Gräff, rapporteur



ÉCOLE POLYTECHNIQUE
FÉDÉRALE DE LAUSANNE

Suisse
2018

Acknowledgements

Firstly, I would like to express my sincere gratitude to my supervisor Prof. Carl Petersen for the continuous support of my PhD study, for his patience, motivation, and knowledge. 5 years ago, he gave me the opportunity to join the lab as an intern, and soon after, to continue as a PhD student. His constant enthusiasm and curiosity for neuroscience was inspiring for me and helped me to develop as a scientist.

Besides my supervisor, I would like to thank Sylvain Crochet for his support and encouragement during my project. At many stages in the course of this research project I benefited from his advice, particularly when I was exploring new ideas and analyzing data.

I thank all my labmates for the stimulating discussions, and for all the fun we have had during these years.

I am thankful to Eloise Charriere and Katia Galan not only for their technical help on my experiments, but mostly for the encouragement and friendship, as well as the support during the tough times of my PhD.

I would like to thank Prof. Anthony Holtmaat, Prof. Laurent Bourdieu, Prof. Johannes Graff for accepting my invitation to serve as my PhD jury committee, as well as Prof. McCabe for serving as president of the committee.

Last but not least, I would like to thank my family, especially my parents, my brothers, my grandmother, and my parents in law for supporting me and constantly caring for my well-being and happiness throughout my PhD and my life in general.

Finally, to my beloved husband Stefanos, my warmest and most grateful “Ευχαριστώ” goes to you, for always believing in me, supporting me, encouraging me, and sharing my joys and frustrations during this whole journey.

Abstract

Excitatory projection neurons of the neocortex are thought to play important roles in perceptual and cognitive functions of the brain by directly connecting diverse cortical and sub-cortical areas. However, many aspects of the anatomical and functional organization of these inter-areal connections are unknown. The mouse primary somatosensory whisker barrel cortex (S1) serves as an important model for investigating the mammalian neocortex, and, here, I firstly investigate the structure and secondly the function of a specific subset of S1 cortico-cortical long-range projection neurons.

In the first part of my thesis, I studied long-range axonal projections of excitatory layer 2/3 neurons with cell bodies located in S1. As a population, these neurons densely projected to secondary whisker somatosensory cortex (S2) and primary/secondary whisker motor cortex (M1/2), with additional axon in the dysgranular zone surrounding the barrel field, perirhinal temporal association cortex and striatum.

The execution of a goal-directed behavior requires the brain to process incoming sensory information from the environment in a context-, learning- and motivation-dependent manner in order to perform specific motor actions. Cortico-cortical communication in the context of goal-directed sensorimotor transformation has begun to be studied, but little is known about how signaling between interconnected cortical areas is modified by sensorimotor learning, as well as in response to changes in reward contingencies. Hence, in the second part of my thesis, I studied cortico-cortical dynamics in primary whisker somatosensory barrel cortex (S1) of mice during a combined whisker and auditory task. Using transgenic mice expressing GCaMP6f combined with two-photon microscopy and retrograde labeling techniques, I chronically monitored the activity of excitatory layer 2/3 neurons in S1 projecting to M1 or S2, while mice learned the behavioral switch task. The results demonstrated that both classes of neurons responded after whisker and auditory stimulation. However, the whisker stimulus evoked response was stronger than the auditory stimulus evoked response. Neurons projecting to S2 exhibited stronger responses compared to neurons projecting to M1 neurons. Those responses remained relatively stable across training sessions and under different reward conditions. Furthermore, both

classes of neurons responded during spontaneous licking, but neurons projecting to S2 had larger licking-related responses compared to neurons projecting to M1.

This work therefore furthers our knowledge of the structure and function of specific types of cortical projection neurons, which is a necessary step towards detailed understanding of how sensory information might be signaled from primary sensory areas to downstream brain regions for further processing.

Keywords: Neocortex, Whisker primary somatosensory cortex, Whisker motor cortex, Whisker secondary somatosensory cortex, Projection neurons, Cortico-cortical connectivity, Two-photon calcium imaging, Sensorimotor learning, Retrograde labelling, Genetically encoded calcium indicators

Resume

Les neurones de projection excitateurs du néocortex jouent un rôle important dans les fonctions perceptuelles et cognitives du cerveau en connectant directement différentes zones corticales et sous-corticales. Cependant de nombreux aspects anatomiques et fonctionnels de ces connexions demeurent inconnues. Le cortex somatosensoriel primaire des vibrisses (vS1) chez les rongeurs – également appelé cortex en tonneau – est un modèle de choix pour étudier le néocortex des mammifères. Dans le cadre de mes travaux de thèse, j'ai examiné la structure et la fonction d'un sous-ensemble spécifique de neurones de projections cortico-corticales dans vS1.

Dans la première partie de ma thèse, j'ai étudié les projections axonales longues des neurones des couches 2/3 de vS1. En tant que population, ces neurones se projettent fortement vers le cortex somatosensoriel secondaire des vibrisses (vS2) et le cortex moteur primaire/secondaire des vibrisses (vM1/M2), avec des axones additionnels dans la zone dysgranulaire entourant le champ des tonnaux de vS1, le cortex d'association périrhinal temporal et le striatum.

L'exécution d'un comportement motivé demande au cerveau de traiter l'information sensorielle issue de l'environnement externe en fonction du contexte, des connaissances et de la motivation du sujet, dans le but d'accomplir des actions motrices les mieux adaptées. Le rôle de la communication cortico-corticale dans ces transformations sensorimotrices commence à être étudiée, mais peu de choses sont connues sur la manière dont la communication entre les aires corticales est modifiée par l'apprentissage ou en réponse à changement de règle quant à l'obtention de récompense. Par conséquent, dans la seconde partie de ma thèse, j'ai étudié la dynamique cortico-cortical dans vS1 chez des souris exécutant une tâche combinant un stimulus tactile (vibrisse) et auditif. J'ai utilisé des souris transgéniques exprimant un marqueur fluorescent sensible à la concentration intracellulaire de calcium (GCaMP6f) ainsi que de la microscopie biphotonique et des techniques de marquage rétrograde. J'ai pu ainsi suivre l'activité des neurones excitateurs des couches 2/3 de vS1 projetant vers vM1 et vS2, pendant que la souris apprenait la tâche de comportement alterné. Les résultats ont démontré que les

deux classes de neurones répondaient après la stimulation des vibrisses et de l'audition. Cependant la réponse provoquée par le stimulus de la vibrisse était plus forte que la réponse provoquée par le stimulus auditif. Les neurones se projetant vers vS2 ont montré des réponses plus marquées comparées à celles des neurones se projetant vers vM1. Ces réponses sont restées relativement stables tout au long des sessions d'entraînement et sous différentes conditions de récompenses. En outre les deux classes de neurones ont répondu pendant la réponse motrice spontanée (léchage), mais les neurones se projetant vers vS2 ont des réponses plus longues que les neurones se projetant vers vM1.

Par conséquent, ce travail a approfondi nos connaissances sur la structure et la fonction de types spécifiques de neurones à projection corticale, ce qui est un pas nécessaire vers la compréhension détaillée de la manière dont l'information sensorielle peut être signalée par les zones sensorielles primaires vers les régions en aval du cerveau pour un traitement ultérieur.

Mots-clés: néocortex, cortex somatosensoriel primaire des vibrisses, cortex moteur des vibrisses, cortex somatosensoriel secondaire des vibrisses, neurones à projection, connectivité cortico-corticale, imagerie calcique biphotonique, apprentissage sensorimoteur, marquage rétrograde, indicateurs calciques génétiquement codés.

Table of Contents

ACKNOWLEDGEMENTS.....	III
ABSTRACT	V
RESUME	VII
CHAPTER 1 INTRODUCTION	13
1.1 NEOCORTICAL MICROCIRCUITRY : FROM NEURONS TO NEURONAL NETWORKS	13
1.2 SENSORY PERCEPTION IN THE BRAIN	16
1.2.1 Sensation and perception	16
1.2.2 Coding sensory information	17
1.3 WHISKER-BARREL CORTICAL NETWORK.....	18
1.3.1 Pathway from the whiskers to barrel cortex	18
1.3.2 Microstructure of the barrel cortex	21
1.3.3 Excitatory neurons in barrel cortex.....	22
1.3.4 Excitatory synaptic input-output in L2/3 barrel cortex	23
1.4 LONG-RANGE CORTICAL DYNAMICS IN BARREL CORTEX	24
1.5 WHISKER DETECTION TASK.....	26
1.6 TWO-PHOTON LASER-SCANNING MICROSCOPY	29
1.6.1 Fundamental principles of two-photon microscopy	29
1.6.2 A two-photon laser-scanning microscope setup	30
1.7 CHRONIC IN-VIVO TWO-PHOTON CALCIUM IMAGING	32
1.7.1 Fundamental principles of calcium imaging	32
1.7.2 Calcium indicators	33
1.7.3 Genetically encoded calcium indicators	34
1.8 AIMS OF THE PHD THESIS	37
CHAPTER 2 DIVERSE LONG-RANGE AXONAL PROJECTIONS OF EXCITATORY LAYER 2/3 NEURONS IN MOUSE BARREL CORTEX	41
ABSTRACT	41
2.1 INTRODUCTION	42
2.2 MATERIALS AND METHODS	43

2.2.1	Viral injections and histological analysis	43
2.2.2	Imaging and processing of brain sections	44
2.2.3	Single-cell electroporation, staining and tracing of neurites	44
2.3	RESULTS	46
2.3.1	Viral expression of tdTomato to label neurons in L2/3 of wS1	46
2.3.2	Single-cell anatomy of neurons retrogradely labeled from wS2	49
2.3.3	Single-cell anatomy of neurons retrogradely labeled from wM1	52
2.3.4	Comparison of M1p and S2p neurons	55
2.4	DISCUSSION	59
2.4.1	Axonal projections based on viral injections	59
2.4.2	Axonal projections of individual S2p and M1p neurons	61
2.4.3	Limitations and future perspectives	62
CHAPTER 3 TWO-PHOTON CALCIUM IMAGING OF LAYER 2/3 PROJECTION NEURONS IN WHISKER BARREL CORTEX DURING LEARNING OF A WHISKER AND AUDITORY DETECTION TASK		65
	ABSTRACT	65
3.1	INTRODUCTION	66
3.2	MATERIALS AND METHODS	67
3.2.1	Design and assembly of a two-photon microscope setup	67
3.2.2	Mouse head-post implantation	70
3.2.3	Intrinsic signal optical imaging	71
3.2.4	Craniotomy and chronic cranial window implantation	72
3.2.5	Expression of calcium indicator and retrograde labeling of projection neurons	74
3.2.6	Whisker and auditory detection task	76
3.2.7	Two-photon calcium imaging	81
3.2.8	Calcium imaging analysis	81
3.3	RESULTS	82
3.3.1	Whisker and auditory detection task	82
3.3.2	Two-photon calcium imaging during task learning	86
3.4	DISCUSSION	113
CHAPTER 4 CONCLUSIONS.....		119
REFERENCES		121
CURRICULUM VITAE		143

“The brain is the organ of destiny. It holds within its humming mechanism secrets that will determine the future of the human race.”

Wilder Penfield

Chapter 1

Introduction

1.1 Neocortical Microcircuitry: from neurons to neuronal networks

Since the classic neural doctrine was first described by S. R. y Cajal in the first decade of 1900s, the field of neuroscience has been revolutionized. Particularly after the 1970s, advances in microscopy, brain imaging, electrophysiology and genetics have enormously expanded our understanding of brain structure and function. Regarding the structural organization of the brain, there are four major areas: brainstem (medulla, pons, midbrain), cerebellum, diencephalon (thalamus and hypothalamus), and cerebral hemispheres or telencephalon (cerebral cortex, basal ganglia, hippocampal formation, amygdala and corpus callosum) (**Figure 1.1.a**). The cerebral cortex is anatomically subdivided into four lobes: frontal, parietal, temporal and occipital lobe. With respect to the functional organization of the cortex, different brain areas are specialized for different types of information processing. The cortex comprises three major functional regions: sensory, motor and association areas. In the primary sensory areas, information from mainly one sensory modality is processed, such as visual, auditory, somatosensory, while in higher association areas information from various sensory modalities is integrated, such as audio-visual, visuo-tactile or even audio-visuo-tactile inputs. Neurons within these areas are functionally interconnected forming specific neural networks.

The major cell types that participate in neural microcircuits of the neocortex are: pyramidal cells, interneurons and glial cells. Pyramidal cells are characterized by their triangular-shaped soma, long axons, apical and basal dendrites, and the presence of dendritic spines. Pyramidal neurons exert an excitatory effect on postsynaptic neurons, releasing the neurotransmitter glutamate. Interneurons are characterized by their short axons and the formation of local connections with other neurons. Interneurons exert either an excitatory or inhibitory effect on postsynaptic neurons. The most prominent excitatory interneuron is the spiny stellate cell, which is characterized by several dendrites arising from the soma forming a star-like shape. However, the vast majority of

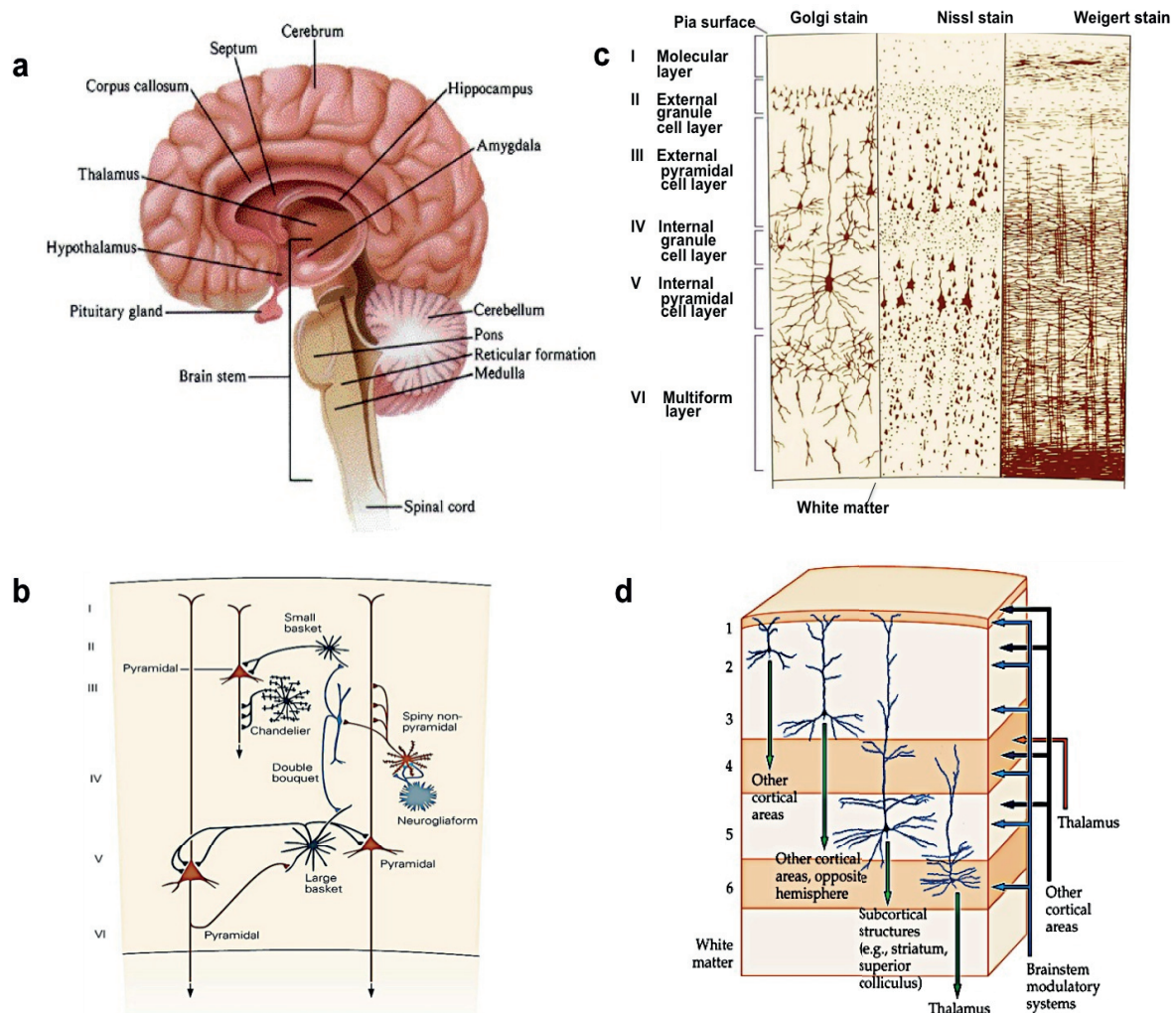


Figure 1.1: Brain anatomy, neocortical microstructure and microcircuitry. (a) The main divisions of the mammalian brain. (b) GABAergic interneurons and their connections (Kandel, 2011). Different types of GABA-ergic neurons (dark gray) and putative GABA-ergic neurons (light gray) have different connections in the neocortex. The chandelier cells terminate exclusively on the axons of pyramidal cells; the large and small basket cells axons terminate mainly on other cell bodies; the double bouquet and neurogliaform cells may also be GABA-ergic. (c) The laminar microstructure of the neocortex (Kandel, 2011). The Golgi stain displays cell bodies, axons, and dendritic trees of neurons; the Nissl stain reveals cell bodies and proximal dendrites; the Weigert stain shows the axonal pattern of myelinated fibers. (d) Canonical neocortical microcircuitry (Purves, 2008).

interneurons are inhibitory neurons that release the neurotransmitter gamma-amino butyric acid (GABA) from their presynaptic specialisations. Several types of GABAergic interneurons have been found in the neocortex depending on their pattern of connections (**Figure 1.1.b**). It has been estimated that 80% of the total number of neurons in the neocortex are excitatory glutamatergic neurons and 20% are inhibitory GABAergic interneurons. Finally, glial cells are characterized by their function to provide support and maintain homeostasis to the neural tissue, and are mainly classified into astrocytes, oligodendrocytes and microglia.

Many studies have focused on the neocortex, as it seems to be involved in higher cognitive functions including sensory perception, associative learning, perceptual decision making and motor planning. The mammalian cerebral cortex varies in thickness, with the thickest area found in motor cortex, which is about 4.5 mm thick in humans, while in fissures it is only 1mm thick (DeFelipe, 2011). The neocortex is a layered structure composed of interconnected columns. In particular, the neocortex consists of the following six layers (**Figure 1.1.c**), each of which contains different cell types in terms of size, shape, inputs and outputs:

- Layer I (L1)-Molecular layer: consists of dendrites and axons of neurons from deeper layers, as well as a few sparsely distributed cells of small size, most of which are GABAergic interneurons.
- Layer II (L2)-External granule cell layer: consists of densely packed small size pyramidal and stellate neurons.
- Layer III (L3)-External pyramidal cell layer: consists of medium-size pyramidal neurons and interneurons.
- Layer IV (L4)-Internal granule cell layer: consists of numerous pyramidal and stellate neurons (major input for sensory afferents).
- Layer V (L5)-Internal pyramidal cell layer: consists of large pyramidal cell bodies and some interneurons.
- Layer VI (L6)-Multiform layer: is a highly heterogeneous layer, consisting of a mixture of large pyramidal neurons and numerous small spindle-like pyramidal and multiform neurons. This layer fuses into the white matter.

Within the neocortical layers, synaptically connected neurons tend to be vertically aligned, forming a column-like organization (vertical cylinders), which is a hallmark of

all cortical areas (Mountcastle et al., 1997, Hubel et al., 1968). The microcircuitry underlying a cortical column is of key importance for processing afferent (input) and efferent (output) signals of subcortical and intracortical areas. According to the canonical microcircuit (Douglas et al., 2007) (**Figure 1.1.d**), thalamic input is mainly relayed to L4 of the neocortex. Pyramidal neurons in the superficial layers make local connections and also project to other cortical areas. L4 excitatory spiny stellate neurons make synapses with pyramidal and inhibitory neurons in L4 and other layers. Inhibitory neurons that are found in all cortical layers are locally connected with excitatory neurons and with each other. Finally, pyramidal cells in deeper layers both make local connections and project to subcortical structures (thalamus, striatum, superior colliculum, brainstem).

With the purpose of understanding neocortical function, one needs to investigate this system from both a micro-scopic (local columnar microcircuits) and a macroscopic view (connections of distant cortical columns) in different behavioral contexts (Feldmeyer et al., 2013). The mouse whisker-barrel system is one of the most well studied sensory model systems. Single cell analysis of the synaptic circuitry and columnar network activity at the population level, combined with behavioral studies, within the mouse barrel cortex, appears a promising approach for the investigation of neocortical function.

1.2 Sensory perception in the brain

1.2.1 Sensation and perception

In most sensory modalities (vision, hearing, touch), the energy of a stimulus is transformed into electrical signals by specialised receptors (photoreceptors, mechanoreceptors, thermal receptors) (Kandel, 2011). The electrical signals that receptors produce are called receptor potentials, and can be either depolarizing or hyperpolarizing signals. The sensory information is then transmitted to the central nervous system via specific sensory pathways, consisting of nerve fibers with numerous axons that make synapses with millions of neurons. In particular, somatosensory information is sequentially relayed in the spinal cord, brain stem, thalamus, and finally cerebral cortex. However, perception is not just a passive transmission of sensory signals, but is formed in higher brain areas by feeding back information to earlier stages of processing. The modification of incoming sensory signals is mediated by learning, memory and attention mechanisms. Thus, perception involves both bottom-up processing of sensory input and top-down ef-

fects influencing sensory processing.

The spatial domain in which a stimulus activates a sensory neuron is called its receptive field (Purves et al., 2008). For example, the region of the skin where a tactile stimulus evokes a response in a touch sensory neuron determines its receptive field. At the level of the sensory organ, each receptor encodes the sensory information applied to the receptive field in terms of magnitude and temporal properties of the stimulus. Thus, the intensity and duration of the stimulus are encoded by the amplitude and time course of the receptor potential as well as by the total number of receptors activated. At the level of the brain, neurons also have specific receptive fields. However, the activity of brain neurons is more complex and variable from trial to trial compared to that of sensory neurons in the periphery.

1.2.2 Coding sensory information

The information detected by sensory receptors has to travel over a long distance to finally reach the central nervous system. However, passive propagation is not sufficient to transmit the sensory signal to the brain. Transformation of the sensory information into action potentials (all-or-none signal) enables its propagation to the central nervous system.

Neurons use sequences or trains of action potentials to transmit sensory information in the brain, based on different coding schemes (Gerstner et al., 1997; Shadlen et al., 1994). Two of them are the rate code and the temporal code. In the rate code, the information is encoded based on the average number of action potentials per unit time (firing rate). In the temporal code the information is encoded based on the precise timing of single action potentials. However, there is still a debate whether rate code or temporal code is used or if both are applied and how trial-to-trial variability of the spiking pattern is compensated.

Trial-to-trial variability of neuronal spiking pattern can be reduced using population coding. In this coding scheme, stimuli are represented using the activity of a number of neurons. The two-photon calcium imaging method with the use of calcium indicators enables monitoring the activity of populations of neurons within an area.

Finally, in the sparse coding scheme, a stimulus is encoded only by a small set of neurons at any given point in time. Sparseness might be temporal, meaning that activity is only present during only a small number of time periods, or sparseness might refer to a small number of activated neurons within a population. There is increasing experi-

mental evidence for neuronal sparse coding in the supragranular layer II/III of the neocortex (Barth et al. 2012; Crochet et al., 2011; Huber et al., 2008; Houweling et al., 2007). In this layer, pyramidal neurons have lower firing rates than pyramidal neurons in deeper layers for both spontaneous and stimulus evoked activity (Petersen and Crochet, 2013). However, there is a small subset of neurons with high firing rates (Kerr et al., 2007; O'Connor et al., 2010; Margolis et al., 2012), many of which are inhibitory interneurons (Gentet et al., 2010; O'Connor et al., 2010; Crochet et al., 2011). The activity of this subset of inhibitory neurons might be responsible for the reduction in the firing rate of pyramidal neurons that ultimately leads to sparse responses.

1.3 Whisker-barrel cortical network

1.3.1 Pathway from the whiskers to barrel cortex

The whisker system is an important sensory system for rodent survival and navigation. Whiskers serve as highly sensitive detectors of tactile information about the nearby environment. By using their whiskers, rodents can locate an object and collect information about its features, such as size, shape and texture, by sweeping their whiskers backwards and forwards across the object at (5-10Hz), a movement known as whisking. Many whisker-related tasks have been developed recently, underlying the functional abilities of this sensory system: whisker deflection detection, object detection, texture discrimination, two-alternative forced-choice (O'Connor et al., 2010; Crochet et al., 2011; Huber et al., 2012; Petreanu et al., 2012; Xu et al., 2012; Chen et al., 2013a; Chen et al., 2013b; Mayrhofer et al., 2013; Sachidhanandam et al., 2013; O'Connor et al., 2013).

The whiskers on the snout of the rodent are arranged in horizontal rows (labeled as A-E) and columns (labelled as 1, 2, 3, etc) (**Figure 1.2.a**). Additionally, there are four posterior whiskers between two consecutive rows, called straddler whiskers (α , β , γ , δ) (Woolsey and Van der Loos, 1970). Each whisker follicle contains numerous mechanoreceptors innervated by sensory neurons located in the trigeminal ganglion. These specialized receptors transform mechanical energy produced by vibration of the whisker into electrical signals. The primary sensory neurons in the trigeminal ganglion transmit signals (via the trigeminal nerve) generated from single whiskers towards the trigeminal nuclei of the brainstem. The trigeminal nuclei complex consists of the princi-

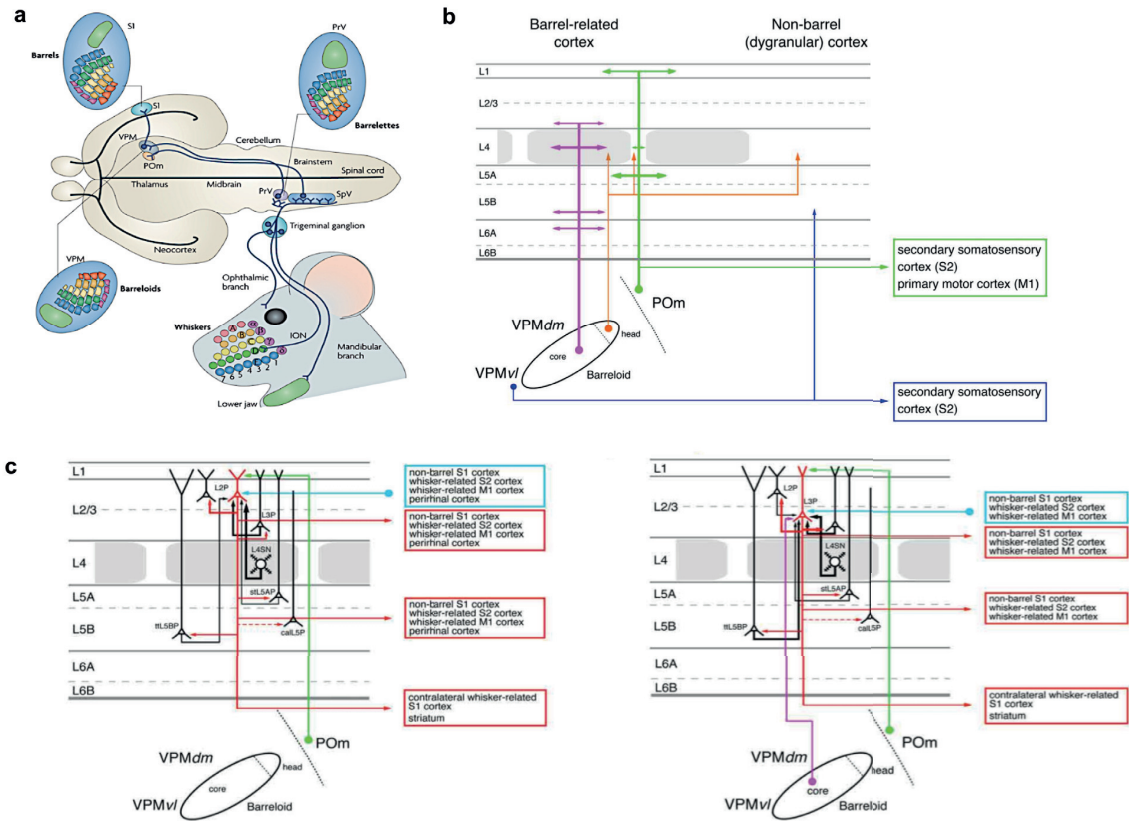


Figure 1.2: Synaptic pathway from whiskers to the primary somatosensory cortex. (a) Whisker mapping in the mouse brain (Erzurumlu (2010)). The whiskers on the snout of the rodent are arranged into rows (AE) and columns (1, 2, 3, etc), including four posterior whiskers the straddles (α , β , γ , δ). The maxillary branch of the trigeminal ganglion nerve fiber relays signals to the trigeminal nuclei of the brainstem, where neurons are clustered into barrelettes. Sensory signals are then conveyed from the trigeminal nuclei to the thalamus, where neurons in VPM form barreloids. From the thalamic station, sensory information is relayed to the neocortex into the identifiable barrels. PrV: principal trigeminal nucleus, SpV: spinal trigeminal nucleus, ION: infraorbital branch of the maxillary nerve. (b) Schematic representation of the pathways from the thalamus to S1 (Feldmeyer, 2012): lemniscal 1 (magenta), lemniscal 2 (orange), extralemniscal (blue), and paralemniscal (green). The thalamic relay station is divided in VPM area, where neurons are clustered into barreloids, and POM. A barreloid is subdivided into a head, core, and tail region. (c) Excitatory circuitry in L2 (left) and L3 (right) of the barrel cortex (Feldmeyer, 2012) POM: posterior medial thalamic nucleus; VPM: ventral posterior medial thalamic nucleus; VPMdm: dorsomedial section of VPM; VPMvl: ventrolateral section of VPM.

pal nucleus (PrV) and three spinal trigeminal nuclei (oralis, SpVo; interpolaris, SpVi; caudalis:SpVc). At this brain location, neurons are clustered into barrelettes, each of which represent a single whisker and all together forming a complete map of the whisker layout on the snout of the rodent. At the level of trigeminal nuclei, there are neurons that integrate sensory signals from multiple whiskers, as well as neurons that respond to a single whisker. Subsequently, sensory information is relayed from the trigeminal nuclei to the thalamic nuclei (the ventroposterior medial nucleus (VPM) and posteromedial nucleus (POM)). At the level of the thalamus, neurons in VPM are clustered into anatomically defined areas called barreloids that are somatotopically arranged according to the whisker pad. Thalamocortical neurons then relay the sensory information to the cortex via at least four ascending pathways (a brief description is given below) (Petersen, 2007; Diamond et al., 2008; Deschenes et al., 2010; Bosman et al., 2011; Feldmeyer et al., 2012; Feldmeyer et al., 2013). Similar to the trigeminal nuclei and thalamus, neurons in the cortex form aggregates called barrels with analogous arrangement to the whiskers layout on the contralateral side of the animals snout. At the level of the cortex, sensory information is predominantly directed to the primary somatosensory cortex (S1). In addition, sensory input is distributed in other cortical areas, such as the secondary somatosensory cortex and the motor cortex (M1). Considering all the relay stations of the whisker pathway to the cortex, for each whisker there is a corresponding trigeminal barrelette, a thalamic barreloid, and a cortical barrel (**Figure 1.2.a**).

The four trigemino-thalamo-cortical pathways (lemniscal 1, lemniscal 2, extralemniscal, and paralemniscal), which differ in terms of brainstem origin, thalamic relay station, and cortical target layer/compartment, are described below (**Figure 1.2.b**):

- The lemniscal 1 pathway: Neurons in the PrV barrelettes convey sensory signals generated from single whiskers to the corresponding barreloids in the dorsomedial region of VPM (VPMdm). The structure of thalamic barreloids is divided into the head, core and tail, which constitute different thalamic relay stations for each pathway. In this thalamic pathway, sensory information is relayed into the core of a barreloid, in which neurons project to L4, L3, L5B, and L6A of the analogous barrels in S1.
- The lemniscal 2 pathway: Neuronal projections from the PrV convey sensory signals from multiple whiskers to the head region of the corresponding VPMdm bar-

reloid. Afferents from this region innervate the L4 septal regions between the barrels.

- The extralemniscal pathway: Neurons located in barrelettes of the caudal part of the SpV (SpVic), which carry information from multiple whiskers, send projections to the ventrolateral part of the VPM (VPMvl) (the tail region of the barreloids where no clear neuronal clustering is observed). Neuronal afferents from VPMvl terminate in L3, L4 and L6A of the dysgranular zone in S1, as well as in L4 and L6 in S2.
- The paralemniscal pathway: Multi-whisker neurons in the rostral part of SpVi (SpVir) (no barrelette structures observed in this area) send projections to the POM nucleus of the thalamus. Neurons located in the POM target their axons to L1 and L5A barrel regions, as well as to L4 septal regions of the S1. Furthermore, POM projects to S2 and M1.

1.3.2 Microstructure of barrel cortex

The term barrel was used by Woolsey and Van der Loos (1970) to describe neuronal clusters observed in L4 of the mouse primary somatosensory cortex. These neuronal formations are characterised by high density of cell bodies of small stellate neurons surrounding a region filled with dendrites, thalamic axons and glial cells (like a barrel 'hollow'). A barrel column is defined as a cylindrical structure (in mice it is about 300 μ m in diameter) of vertically aligned neurons of the six cortical layers to each barrel in L4 (Feldmeyer et al., 2013). Whisker barrels are separated from each other by areas in L4 called septa. Neurons that are vertically aligned above and below septa form septal columns (Alloway et al., 2007). The area surrounding the barrel field is called dysgranular zone.

Neurons within the barrel system can be activated by providing a rapid deflection to the whiskers, but this response depends on the state/position of the whiskers. Deflection of a single whisker which corresponds to a specific barrel column, the so-called principal whisker, evokes a robust response (Petersen 2007). The direction of whisker deflection elicits distinct neuronal responses (Andermann & Moore, 2006; Kremer et al., 2011; Tsytsarev et al., 2010). In addition, deflection of the surrounding whiskers also elicits responses in neurons within this barrel column. However, different neurons preferentially respond to certain surround whiskers, so that on average the response is considera-

bly weaker than the principal whisker response. Moreover, multi-whisker deflections with different stimulation patterns induces distinct response patterns in L2/3 barrel cortex neurons (Estebanez et al., 2016). In particular, uncorrelated multi-whisker stimulation induces stronger neuronal responses in the center of barrel columns, whereas correlated and anti-correlated multi-whisker stimulation evokes stronger responses in the barrel-septal borders, forming rings of multi-whisker responding neurons.

1.3.3 Excitatory neurons in barrel cortex

About 6500 neurons are estimated to compose a barrel column, the vast majority of which are excitatory (89%) (Lefort et al., 2009). The thickness of the mouse barrel cortex was found to be about 1154 μm , and the depth of each individual layer (distance from the pia to the lower boundaries) was measured as: L1= 128 μm , L2 = 269 μm , L3 = 418 μm , L4 = 588 μm , L5 = 708 μm , L6 = 1154 μm .

Different types of excitatory neurons, in terms of dendritic and axonal morphology, have been found within the mouse barrel column according to laminar location of their cell bodies (Lefort et al., 2009; Feldmeyer et al., 2012). L2 contains densely packed pyramidal neurons that have short apical dendrites with large tufts in L1. These neurons have a long axon extending down to the white matter, with local horizontal projections in L2/3, deeper projections in L5, and long-range horizontal collaterals covering the entire barrel field, in some cases even reaching distant cortical areas like S2 and M1. L3 pyramidal neurons have a longer apical dendrite in L1 with less extensive tufts, and a long axon with long-range projections as for L2 pyramids. L4 mostly contains small spiny stellate neurons with dendrites mainly located within a barrel in L4, and columnar axonal projections innervating all the layers within the column, predominantly L4, L2 and L3. Moreover, L4 includes star pyramidal and pyramidal cells with an apical dendrite reaching the superficial layers. L5 contains large soma excitatory neurons of two morphological types: pyramidal neurons that have long apical dendrites with slender tufts and few axon collaterals in L1 (mostly found in L5A), pyramidal neurons with apical dendrites that have thick tufts (mostly found in L5B). L6A contains pyramidal neurons with vertically aligned untufted dendrites, and pyramidal cells with tufted dendrites that terminate in L4. Additionally in this layer, pyramidal cells with inverted dendritic orientation have been observed. L6B is a highly heterogeneous layer containing pyramidal cells with diverse dendritic arborisations.

1.3.4 Excitatory synaptic input-output in L2/3 barrel cortex

The activity pattern of pyramidal cells in L2/3 depends on their location (barrel or septa) and depth (superficial L2 or deeper L3) in the barrel cortex (Shepherd et al., 2005; Petersen & Crochet, 2013). Electrophysiological recordings in L2/3 in the mouse barrel cortex during active whisker touch have shown that pyramidal neurons located deeper in L3 responded fast, with short latency and large amplitude (Crochet et al., 2011). However, superficial excitatory neurons located in L2 responded with smaller amplitude, and longer latency and duration. The fast and large responses of L3 neurons might be driven by three input sources: the direct thalamocortical projections from the VPM (lemniscal 1 pathway), the strong recurrent excitatory connections between L3 pyramidal cells, and the axons collaterals coming from L4 excitatory neurons (Lefort et al., 2009; Feldmeyer et al., 2012). On the other hand, the small and slow responses of L2 neurons might be due to the lack of input from the thalamus, as well as to the higher density in GABAergic neurons compared to L3 (**Figure 1.2.c** (right panel)). The sensory responses of L2 pyramidal neurons are likely to be driven primarily by intracortical excitatory inputs from L2, L3, L4 and L5 (**Figure 1.2.c** (left panel)). In addition, both L2 and L3 pyramidal neurons, which have apical dendrites in L1, receive input from POM projections in L1 (paralemniscal pathway), with L2 neurons forming more synaptic connections due to their larger dendritic tufts. The apical tufts of L2/3 neurons also receive input from M1 projections in L1 (M1 is involved in voluntary control of whisker movements) (Matyas et al., 2010; Mao et al., 2011). Thus L2/3 synaptic connections in L1 with POM and M1 might integrate signals related to whisker position and movement. Furthermore, neurons in superficial L2/3 are innervated by long-range axonal collaterals of neurons in the S2.

Considering the morphological properties of L2/3 excitatory neurons, the output signals of these neurons are directed locally within L2/3, vertically to deeper cortical layers, horizontally across the entire barrel field, as well as to other cortical regions. As previously mentioned, pyramidal cells in L2/3 have a long axon extending down to deeper cortical layers, which forms strong synaptic contacts mainly with the basal dendrites of interconnected L5A and L5B pyramidal neurons (the prominent cortical output layer) (Lefort et al., 2009; Petreanu et al., 2012). Furthermore, L2/3 excitatory neurons make local connections with neighboring L2/3 pyramidal neurons [Lefort et al., 2009; Feldmeyer et al., 2006]. Long-range horizontal collaterals of L2/3 neurons extend

across the barrel field making contacts with surrounding cortical columns, thus being in a position to coordinate synaptic activity with respect to the neighboring barrel columns (Adesnik et al., 2010).

Additionally to the horizontal axon collaterals within S1, L2/3 pyramidal neurons project to other cortical areas. Long-range projections to the contralateral barrel field via the corpus callosum have been found, predominantly targeting L2/3, L5A and L5B and to a less extend L6 neurons (Petreanu et al., 2007; Aronoff et al., 2010). S1 reciprocally innervates S2 via large-scale horizontal collaterals emerging from pyramidal neurons in L2/3 and L5 of the barrel cortex (Aronoff et al., 2010). Moreover, L2/3 and L5 neurons in S1 send long-range axonal projections to M1 innervating preferentially L2/3, and as mentioned earlier, M1 neurons project back to S1, forming a feedback loop. It has been shown that both S1 neurons projecting to M1 and S1 neurons projecting to S2 have distinct functional properties in behaving animals (Matyas et al., 2010; Petreanu et al., 2012; Chen et al., 2013a; Yamashita et al., 2013).

1.4 Long-range cortical dynamics in barrel cortex

Long-range connections between cortical areas play an important role in sensorimotor processing and behavior (Buzsaki, 2010; Kopell et al., 2014; Fries, 2015). However, the exact role and function in cortical dynamics remain an open question. In recent years, progress has been made in understanding cortico-cortical dynamics by studying functional interactions between S1 and M1 as well as between S1 and S2.

Studies have shown that interactions between S1 and M1 appear to have several functions (**Figure 1.3.a**). Electrophysiological recordings of neurons in S1 projecting to M1 (M1p) demonstrated that passive tactile stimulation evoked faster and larger postsynaptic potentials (PSPs), as well as phasic action potential firing, while repetitive active touch evoked strongly depressing PSPs and only transient firing (Yamashita et al., 2013). M1p neurons reliably encoded texture related fine kinematic features such as whisker angle, stick-slip events and curvature changes. (Chen et al., 2015). Furthermore, input from S1 to M1 can affect whisker movement, (Sreenivasan et al., 2016). Optogenetic inactivation of S1 excitatory neurons caused hyperpolarization of membrane potential and reduced firing rate in M1, along with reduced whisking activity. On the contrary, optogenetic excitation of S1 drove activity in M1 neurons, as well as

evoked long-latency M1-dependent whisking (Sreenivasan et al., 2016). Thus, the S1 to M1 pathway might be involved in initiating motor plans after stimulus detection and probably in responses to specific stimulus features.

Regarding the M1 to S1 pathway, studies on trained mice on a whisker-based object localisation task have shown that calcium activity of axons from neurons in M1 projecting to S1 carries mixed information about whisker kinematic features, object location, and touch (Petreanu et al., 2012). Thus, neurons in S1 receive motor and sensory information from M1, which is critical for object identification and navigation by ac-

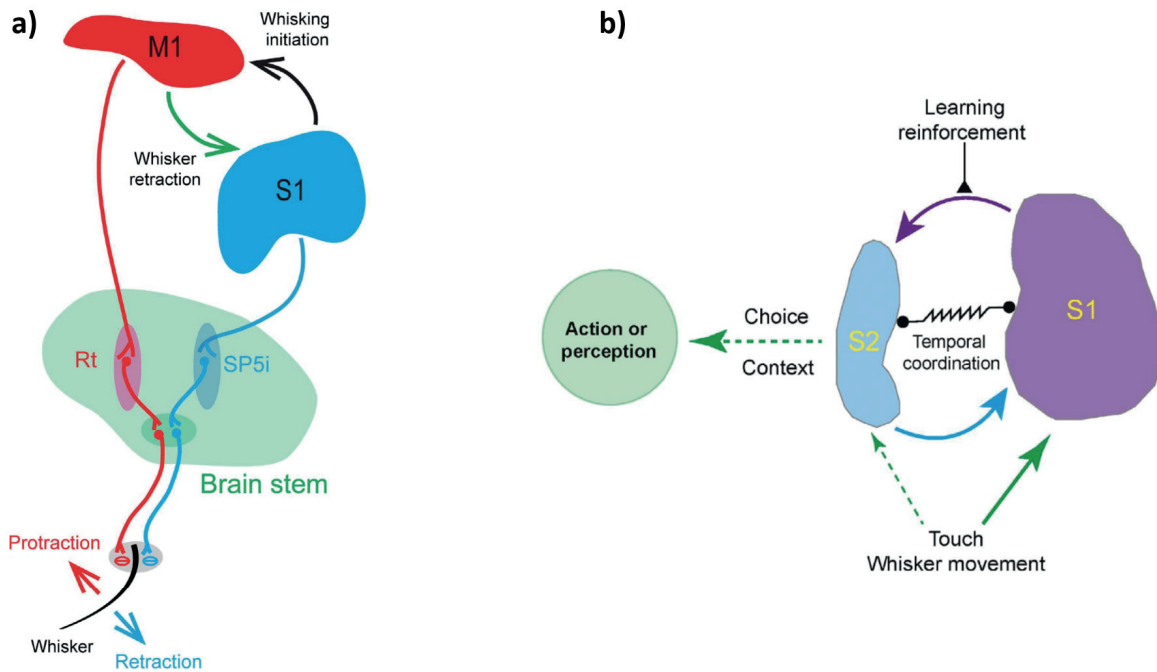


Figure 1.3: a) Functional interactions between S1 and M1. b) Functional interactions between S1 and S2 (Ni & Chen, 2017).

tive touch. Moreover, axonal projections from M1 to S1 are thought to mediate whisker retraction (Matyas et al., 2010). Dendritic imaging of L5 pyramidal neurons in S1 in mice performing an object localization task has shown large-amplitude calcium signals along the apical tuft dendrites when active touch occurred at specific object locations or whisker angles. These calcium signals require both vibrissal sensory input and primary

motor cortex activity (Xu et al., 2012). These findings suggest that M1 to S1 pathway facilitates whisker-based object localisation and possibly other functions that require sensorimotor integration.

On the other hand, interactions between S1 and S2 areas appear to serve different functions (**Figure 1.3.b**). Whole-cell recordings of neurons in S1 projecting to S2 (S2p), in contrast to M1p neurons, demonstrated sustained firing in response to passive whisker stimulation and accumulated responses to repetitive active touch (Yamashita et al., 2013). This might indicate that S2p neurons have the ability to integrate sensory information over time, which might be essential for object feature recognition. In addition, during texture discrimination S2p neurons exhibited stronger responses and enhanced choice-related activity compared to other S1 neurons, as well more accurately encoding of different textures (Chen et al., 2013). During learning of a texture discrimination task, only S2p neurons developed activity patterns correlated with the animal's decision, contrary to M1p neural responses that reliably and stably encoded basic kinematic features (Chen et al., 2015). In a single whisker stimulus detection task, learning evoked licking-related depolarization in S2p neurons, which was correlated with the animal's decision (Yamashita & Petersen, 2016). Therefore, S2p neurons might be related to the acquisition of choice- or context-related responses during behavioral learning. Regarding the S2 to S1 pathway, imaging S2 axonal responses in S1 in mice performing a whisker detection task showed that activity encoding touch and choice were present in S2 and propagates in a S1-S2 loop such that S2 cortical feedback might reinforce feedforward input from S1 (Kwon et al., 2016).

1.5 Whisker detection task

A standard method for studying the function of neocortical activity is the coupling of single-cell and/or neuronal populations analysis with behavioural studies underlying higher cognitive functions such as sensory perception and decision-making. Perceptual decisions can be studied using different conditions and sets of stimuli, for instance different amplitudes or frequencies of a sound stimulus, or different orientations of moving bars. Psychometric functions are then used to describe the subject's performance to certain stimulus features. A psychometric curve plots the percentage of times the subject reports detecting the stimulus as a function of stimulus amplitude. The main characteristics of a psychometric curve are the threshold and the slope. The sensory threshold denotes

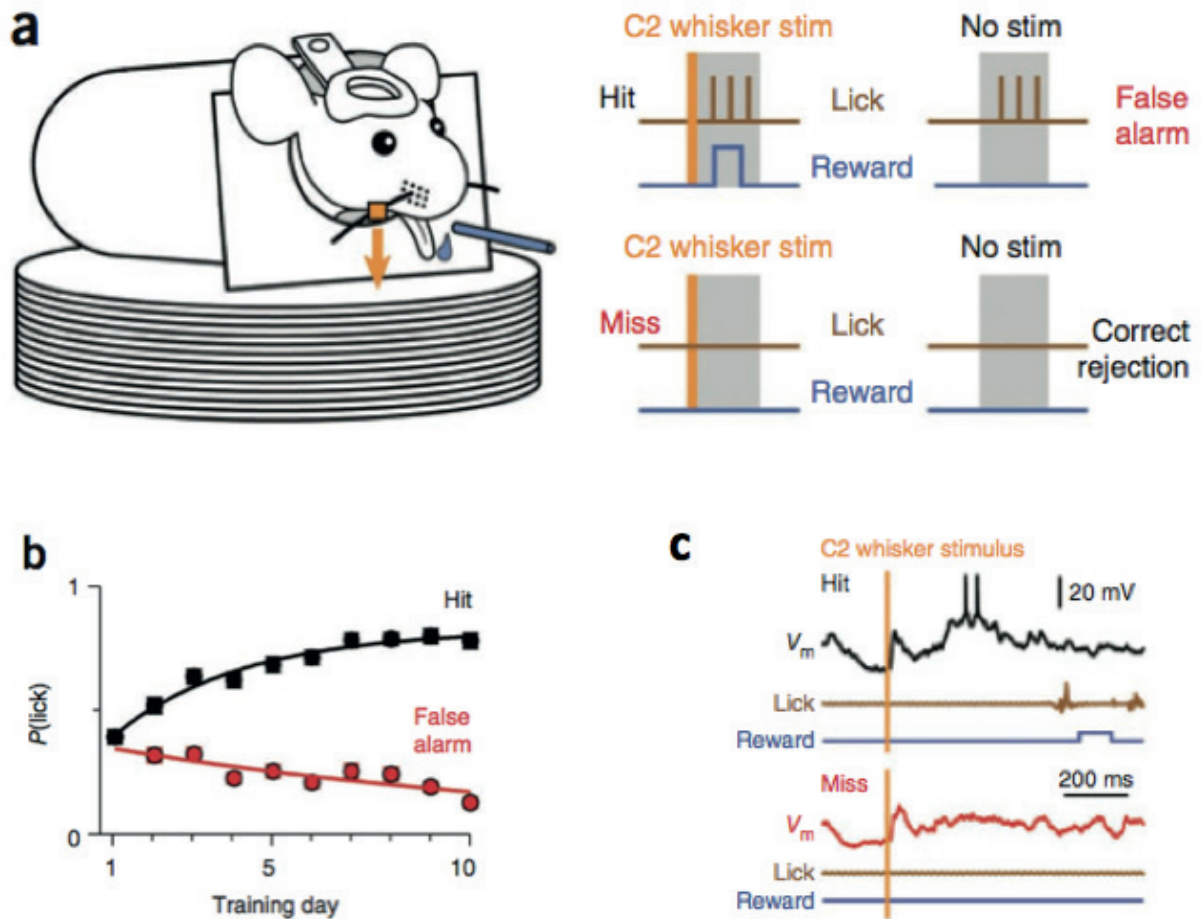


Figure 1.4: The detection task (Sachidhanandam et al., 2013). (a) The experimental setup, paradigm and time sequence of an individual trial. (b) The probability of licking in trials with stimulus (hit) and in trials without stimulus (false alarm) over daily training sessions. (c) Early phase and late depolarization in example hit and miss trials during whole-cell V_m recordings.

the stimulus strength that gives a 50% response. The slope of a psychometric curve indicates how sensitive the sensory system is in detecting a stimulus feature. On the other hand, neurometric curves are used to describe neuronal responses to certain stimulus features during a decision task. The comparison of psychometric and neurometric curve helps the understanding of the mechanisms underlying perceptual decision-making (Stuttgen et al., 2011).

In a simple tactile whisker-dependent detection task (Sachidhanandam et al., 2013), head-restrained mice are trained to detect single C2 whisker deflections, and report sensory perception via licking a waterspout so as to receive a reward (**Figure 1.4.a**). Whisker deflections of 1ms are provided by magnetic stimulation of iron particles attached to the C2 whisker. Stimulus arrives at random time points with an intertrial interval in the range of 2-8 s, and without any preceding cue. In order to control for spontaneous licking, catch trials (no stim) are intermixed with stimulus trials (C2 whisker stim), where no stimulus is applied and no reward is delivered. A typical training period, where the mice have learned to perform the task reaching stable psychometric performance is about 7 to 10 days (**Figure 1.4.b**).

Whole cell recordings of neurons in the barrel cortex during the detection task have revealed membrane potential correlates of sensory perception (**Figure 1.4.c**) (Sachidhanandam et al., 2013). In particular, whisker stimulation induces an early and reliable sensory response within less than 50 ms, whereas a late depolarization is observed at 50 to 400 ms after the stimulus onset, which is enhanced on hit trials compared to misses. In another study, whole cell recordings were performed on neurons in S1 projecting to either S2 (S2p) or M1 (M1p) during the whisker detection task, in expert as well as in naïve mice (Yamashita & Petersen, 2016). They found that whisker stimulation in expert mice, evoked the strongest response in S2p neurons correlated with task performance. The largest difference in activity during task performance between S2p and M1p neurons was observed during the lick period, which was 250-1000 ms upon whisker stimulation. Furthermore, electrophysiological recordings from GABAergic inhibitory neurons in L 2/3 of S1 were performed during the execution of the whisker detection task (Sachidhanandam et al., 2016). In this study, they observed distinct neuronal properties amongst parvalbumin-expressing (PV), vasoactive intestinal peptide-expressing (VIP), and somatostatin-expressing (SST) neurons during task performance. Calcium imaging experiments have shown enhanced decision-related signaling in S2p neurons during a whisker detection task (Kwon et al., 2016; Yang et al.,

2016), which might be supported through reciprocal neuronal excitation of S1 and S2 areas.

1.6 Two-photon laser-scanning microscopy

1.6.1 Fundamental principles of two-photon microscopy

Two photon-excited fluorescence laser-scanning microscopy (Denk et al., 1990) is a high-resolution non-linear imaging technique that allows cellular imaging up to ~1000 μm depth in living tissues. Two-photon imaging in combination with calcium indicators enables monitoring neuronal activity within a population of neurons both *in-vitro* and *in-vivo* (Stosiek et al., 2003; Helmchen et al., 2005; Svoboda et al., 2006; Konig et al., 2000). Compared to linear imaging techniques, where light interacts with a single photon in the elementary process, non-linear microscopy is based on higher-order light matter interactions, where multiple photons are involved in the signal generation process. Two-photon microscopy is based on the physical phenomenon of fluorescence excitation by two-photon absorption, where a fluorescence molecule is excited to a higher energy state when two simultaneously arriving photons (within 0.5 fs) are absorbed. Subsequently, the excited fluorophore returns to its baseline via fluorescent emission of a single photon, the energy of which is slightly less than the sum of the energies of the two absorbed photons (**Figure 1.5.a**).

The probability of this phenomenon to occur is extremely low, and depends on the square of the photon density of the excitation light. Therefore, the excitation light has to be concentrated in space and time. Concentration in space requires high numerical aperture (NA) objectives for focusing the laser beam in order to achieve high spatial densities of photons. Concentration in time requires the use of lasers producing ultra-short pulses (about 100 fs) of light. Typical lasers used for two-photon microscopy provide pulses of width ~100 femtoseconds at a rate of about 80 MHz. There are primarily two advantages of two-photon over confocal microscopy (single photon absorption) for long-term imaging in highly scattering tissue, such as the neocortex of living animals: firstly, in two-photon microscopy the energy of each of the two photons used to excite a fluorophore is almost half the energy of the emitted photon, whereas in confocal microscopy the energy of the excitation photon should be higher than the energy of the emitted photon. Typically, the light spectra used for two-photon excitation lies in the

range of 700-1000 nm (near infrared), whereas for single-photon is within the 300 - 500 nm range (ultraviolet and visible). The wavelength of the emitted photons depends on the type of fluorophore used, and commonly occurs in the visible spectral range (400-700 nm). The main advantages of using near infrared light is deeper penetration into scattering tissue (up to 1000 μ m) due to the longer wavelength, and less phototoxicity due to lack of endogenous one-photon absorbers in this optical window of cells and tissues. Secondly, in two-photon microscopy, the fluorescence signal originates mainly from the point that the laser beam has been focused on after passing the objective (**Figure 1.5.b**), due to the fact that two-photon absorption depends on high photon densities (light intensity). However, in confocal microscopy single photon excitation occurs within the whole light cone of the focused laser beam, thus, a pinhole is utilized to exclude out-of-focus background signal from detection. The localization of excitation in two-photon microscopy is of great importance, as all the emitted fluorescence photons originate from the focal plane provide useful signal (no need of a pinhole), even those photons that have been scattered and eventually turn back to the detection path (**Figure 1.5.c**). Additionally, light above and below the focal plane causes less bleaching and phototoxicity, than in confocal microscopy.

1.6.2 A two-photon laser-scanning microscope setup

In two photon laser-scanning microscopy, an image is generated by moving the focal point of a laser beam over the sample using a pair of scanning mirrors, where at each mirror position, the fluorescent emitted light is collected by a photo multiplier tube (PMT), and finally assigned to certain pixels of the image (Konig, 2000; Helmchen & Denk, 2005; Svoboda & Yasuda, 2006). The typical optical pathway of a two-photon microscope (**Figure 1.5.d**) starts from the laser source, which is an ultrafast pulsed-laser providing near- infrared (700-1000 nm) ultrashort pulses of ~100 fs width and ~80 MHz rate. Because the laser beam is linearly polarized, the intensity can be adjusted by using a $\lambda/2$ waveplate and a polarizer. In addition, acousto- or electro-optical devices (Pockels cell or Acousto-Optic Modulator (AOM)) can be used to adjust laser beam intensity, by modifying the phase, frequency, polarization or amplitude of the laser. Such devices can also be used to automatically compensate for power loss with depth (Helmchen & Denk, 2005; Kremer et al., 2008; Akemann et al, 2015). The laser beam size is then expanded using a telescope (pair of curved lenses). Then, the beam is deflected in x-y directions by a scanning device (pair of galvanometric or resonant scan

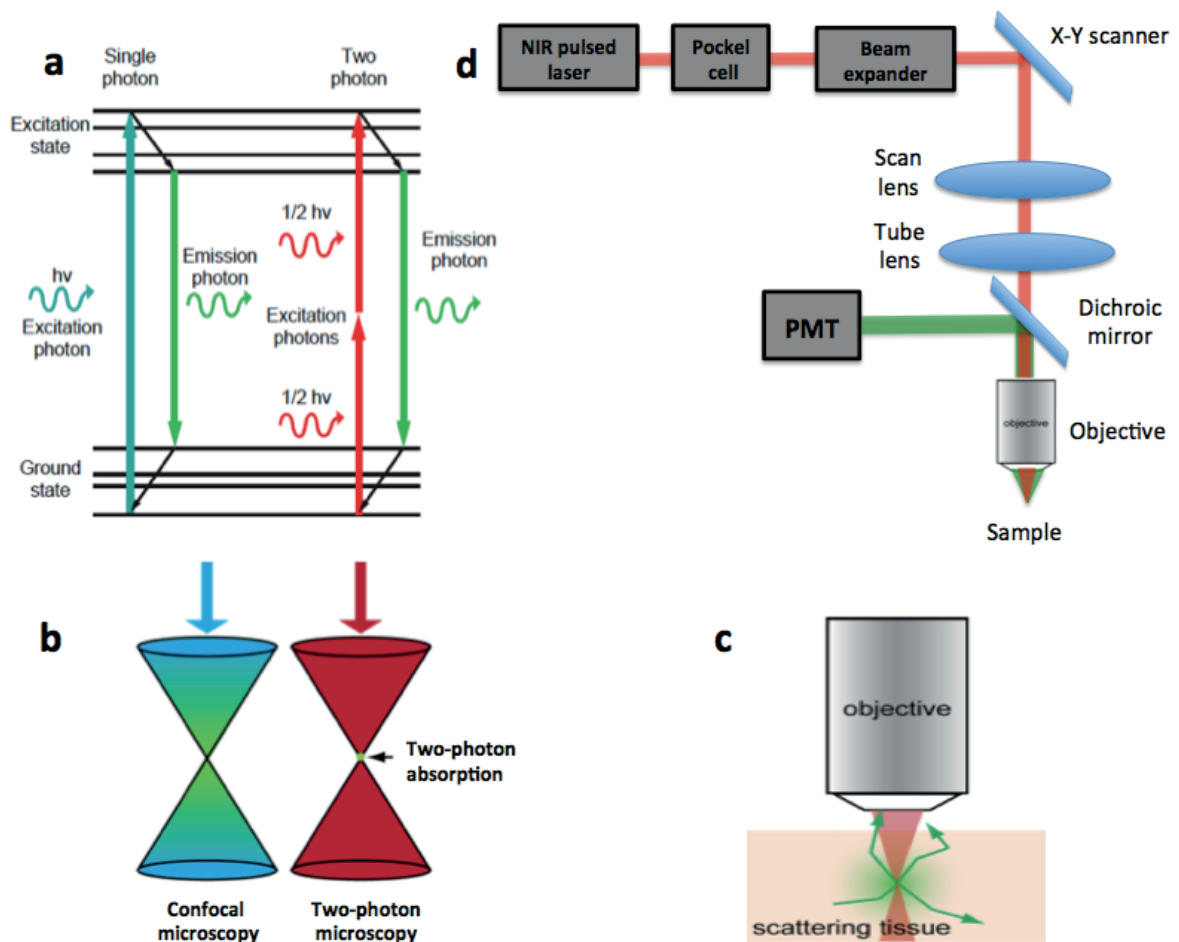


Figure 1.5: Two-photon laser scanning microscopy. (a) Simplified Jablonski diagram of single photon and two-photon excitation process. (b) In single-photon microscopy an entire cone of fluorescence light (green) is generated, whereas in two-photon microscopy fluorescent signal is localized only in the perifocal region. (c) In scattering tissue, photons emitted in directions outside the aperture angle can still be collected if they return to the detection path. (d) Basic elements of a two-photon microscope: pulsed near-infrared laser, pockels cell, beam expander, X-Y scanners, scan lens, tube lens, dichroic mirror, objective, photomultiplier tube (PMT).

ners or acousto-optic deflectors (AODs)) (Helmchen & Denk, 2005; Kremer et al., 2008; Grewe and Helmchen, 2014; Akemann et al, 2015), and further expanded by passing through a pair of scan and tube lens, in order to fill the back aperture of the objective. After passing through the objective, the beam focuses into the sample, and fluorescence emission occurs within a certain area defined by the scanning amplitude of the mirrors. The fluorescent light passes through the objective (following the opposite direction of the excitation light), then is reflected by 90 degrees using a dichroic mirror (beamsplitter), and finally is collected by the PMT.

1.7 Chronic *in-vivo* two-photon calcium imaging

1.7.1 Fundamental principles of calcium imaging

Cells maintain concentration gradients for particular ions across their cell membranes through ion-specific pumps (Kandel et al., 2011). These ionic gradients develop the electrical membrane potential of a cell, which can be altered when the cell is electrically excited by temporarily changing its permeability for certain ions via gateable transmembrane channels. Particularly in neurons, changes in membrane potential accompanied with action potentials are associated with movement of calcium ions from the extracellular space to the cytoplasm leading to an increase in intracellular calcium concentration. Neurons at rest have a calcium concentration of about 50 - 100 nM, but when electrically activated this level increases up to 10 times (Grienberger et al., 2012). This transient increase of the intracellular calcium concentration, termed a calcium transient ($\Delta[\text{Ca}]$), is characterised by a sharp rise followed by an exponential decay with a time constant of around 100-200 ms for neuronal somata. Calcium influx from the extracellular compartment to the cytosol is mediated by voltage-gated calcium channels (VGCC), ionotropic glutamate receptors (Ca^{2+} permeable AMPA-R, NMDA-R), nicotinic acetylcholine receptors (nAChR), and transient receptor potential type (TRP) channels. Calcium efflux from the cytosol to the extracellular space is mediated by the plasma membrane calcium ATPase (PMCA), and sodium-calcium exchanger (NCX). Additionally, calcium exchange within the cell is established by internal stores such as the endoplasmic reticulum (ER) and mitochondria. In particular, calcium release from the ER occurs via inositol trisphosphate receptors (IP3R) and ryanodine receptors (RyR). Calcium influx from the cytosol to the ER is maintained by the sarco-endoplasmic reticulum calcium

ATPase (SERCA) (**Figure 1.6.a**) (Grienberger et al., 2012). The free calcium concentration within the cytosol is determined by the three following processes: (1) calcium balance of influx and efflux between extracellular space and cytosol, (2) calcium exchange from internal storages, (3) calcium buffering by calcium-binding proteins (parvalbumin, calbindin and calretinin). A key aspect is that only free intracellular calcium ions are biologically active, and calcium-binding properties determine their dynamics within the cytosol.

1.7.2 Calcium indicators

As mentioned above, membrane potential changes in neurons are accompanied by changes in intracellular calcium concentration. Small fluorescent molecules that change their optical properties based on fluctuations of calcium concentration, called calcium indicators, have been widely used to explore neuronal activity. In particular, calcium indicators bind to free calcium ions forming a Ca^{2+} -Indicator complex (Grynkiewicz et al., 1985). Both the formation of the Ca^{2+} -Indicator complex as well as the reverse process should be faster than calcium influx in order to maintain equilibrium in the binding process:



The affinity of the calcium indicator is given by the dissociation constant K_D , which is a relation among the concentration of indicator molecules, calcium ions and calcium-indicator complex:

$$K_D = \frac{[Ca^{2+}] \cdot [\text{Indicator}]}{[\{\text{Indicator} - Ca^{2+}\}\text{complex}]}$$

When a neuron is filled with an indicator at a certain concentration $[\text{Indicator}]$, its baseline fluorescence F_0 depends on the concentration of free intracellular calcium ions $[Ca^{2+}]_{rest}$ under resting conditions (50-100 nM). When the neuron is activated calcium enters the cytosol increasing the total intracellular calcium concentration (10 to 100 folds), leading to changes in fluorescence intensity of the indicator due to calcium binding. At any time point, calcium signals translate into fluorescence signals, which typically are expressed as fluorescence changes relative to the baseline fluorescence signal (Smetters et al., 1999; Peterlin et al., 2000):

$$\frac{\Delta F}{F} = \frac{F_t - F_0}{F_0}$$

or when someone takes into account the background fluorescence signal, which can be measured in blood vessel lumen (Kerr et al., 2005):

$$\frac{\Delta F}{F} = \frac{(F_t - B_t) - (F_0 - B_0)}{(F_0 - B_0)}$$

where F_0 is the baseline fluorescence defined as the average fluorescence signal during a time period when the cell is at rest, F_t is the fluorescence signal at time t , B_0 the average background signal at rest and B_t the background fluorescence at time t .

There are two major types of indicators for measuring calcium transients in neurons: the fluorescent chemical (or synthetic) calcium indicators (Grynkiewicz et al., 1985, Tsien et al., 1989; Paredes et al., 2008) and the genetically encoded calcium indicators (GECIs) (Looger et al., 2011; Tian et al., 2012; Knopfel et al., 2012). Synthetic calcium indicators (e.g, Fura-2, Calcium Green, Fluo-4, or Oregon Green BAPTA), often referred to as traditional dyes, have been widely used in two-photon calcium imaging as they are very sensitive (easily two-photon excited at wavelengths between 800-900 nm) and can be loaded into neurons using several chemical or physical methods (targeted single-cell electroporation, local electroporation, multi-cell bolus loading, transgenesis) (Tsien, 1981; Frostig et al., 2009; Grienberger et al., 2012). However, synthetic sensors cannot easily be targeted to specific cell types and populations, and their loading methods are highly invasive and can be damaging to tissue. Also, they cannot be used for chronic *in vivo* imaging. On the other hand, genetically encoded calcium indicators, are engineered proteins that are artificially expressed in targeted cell types after introducing them through DNA sequences (by using viral infection or transgenesis). Genetically encoded calcium indicators are used for non-invasive long-term imaging of identified neurons and neuronal populations (Grienberger et al., 2012; Rochefort et al., 2008).

1.7.3 Genetically encoded calcium indicators

The development of genetically encoded calcium indicators (Miyawaki et al., 1997) emanated from the achievement of three important steps: the discovery of green fluorescent protein (Shimomura et al., 1962), the engineering of GFP color variants (Heim

and Tsien, 1996), and the study of biochemical interaction between the calcium-binding protein calmodulin (CaM) and the calmodulin-binding peptide M13 (CaM-M13 complex). (Porumb et al., 1996).

There are two major types of genetically encoded calcium indicators (McCombs et al., 2008; Looger et al., 2011; Tian et al., 2012; Knopfel et al., 2012, Koldenkova and Nagai, 2013; Lin and Schnitzer, 2016; Ni et al., 2017), those involving Forster resonance energy transfer (FRET) and the single-fluorophore ones. FRET sensors, such as FIP- CB_{SM} (Romoser et al., 1997) and Yellow Cameleon (Miyawaki et al., 1997), change the emission spectra depending on the relative orientation and distance (should be less than 10 nm) between a donor and an acceptor fluorophore. In the case of Yellow Cameleon 3.60 (**Figure 1.6.b**), the donor is the enhanced cyan fluorescent protein (ECFP) and the acceptor is the circularly permuted Venus protein. These two proteins are linked together by the CAM-M13 complex. When there is no calcium influx the emission is dominated by the blue ECFP fluorescence. When the cell is activated, calcium ions bind to the CaM-M13 complex of the sensor, and conformational changes occur leading to the reduction of the distance between the donor and the acceptor. This

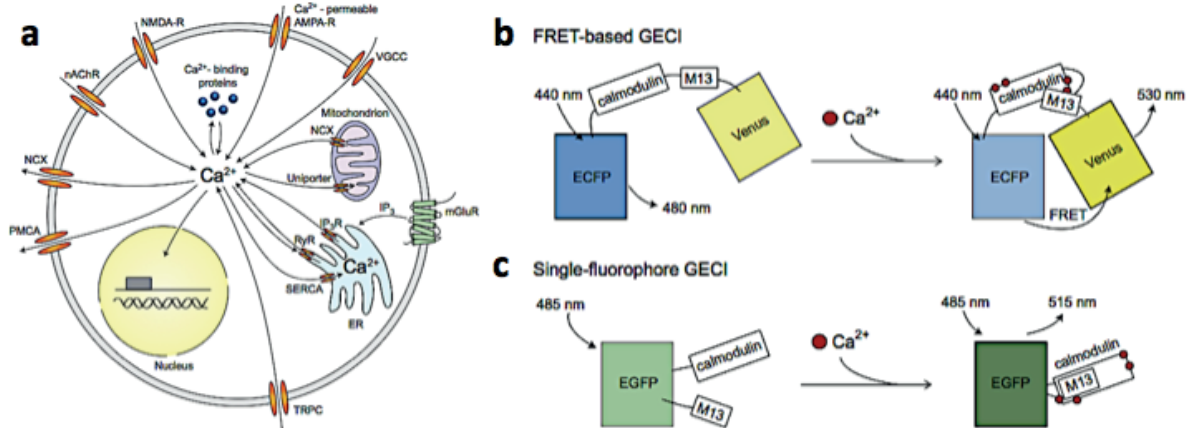


Figure 1.6: Neuronal calcium imaging (Grienberger et al., 2012). (a) Calcium signaling in neurons. Sources of calcium influx and efflux in neurons, calcium exchange from internal sources, and calcium binding proteins. (b) FRET-based genetically encoded calcium indicators. (c) Single fluorophore calcium indicators (GCaMP family).

results in excitation of the Venus protein due to FRET and the emission of yellowish photons (about 530 nm). The calcium signal is expressed as the ratio of the acceptor signal over the donor signal. The single-fluorophore sensors also contain the CAM-M13 complex, which is connected to the circularly permuted enhanced green fluorescent protein (EGFP) (**Figure 1.6.c**). Again, in the presence of calcium, CaM-M13 interactions lead to conformational changes that stimulate fluorescence emission. The GCaMP family are single-fluorophore GECIs that are widely used in calcium imaging experiments, including GCaMP-2 (Akerboom et al., 2009), GCaMP-3 (Tian et al., 2009), GCaMP-5 (Akerboom et al., 2012), GCaMP-6 (Chen et al., 2013d) and the recently developed GCaMP-X (Yang et al., 2018). GCaMP-6 is an ‘ultrasensitive’ calcium sensor that enables the detection of single action potentials in neuronal somata and dendritic spines under optimal recording conditions. The GCaMP6 sensor has three versions, which differ in terms of kinetics (GCaMP6s, 6m and 6f for slow, medium and fast kinetics respectively), with the GCaMP6f version being the fastest with sensitivity similar to synthetic indicators (single AP rise time: 45 ± 4 ms, decay time: 142 ± 11 ms) (Chen et al., 2013d). Recently, an ultrafast GCaMP6_{f_u} version has been developed that displays fluorescence rise and decay times 9 and 22-fold faster than GCaMP6f respectively (Helassa et al., 2016). Furthermore, red-shifted GECI’s have been used in the last decade to monitor neuronal activity, facilitating in-vivo deep-tissue calcium imaging (Zhao et al., 2011; Collot et al., 2012; Akerboom et al., 2013; Wu et al., 2014; Inoue et al., 2015; Dana et al., 2016). The red calcium sensors are based on circularly permuted red fluorescent proteins (RFPs), a calcium-binding protein (calmodulin) and a binding peptide (M13 or cckap).

When choosing a GECI for two-photon calcium imaging, there are three important criteria to consider: the affinity, the kinetics, and the dynamic range (the maximum signal change at calcium saturation) of the sensor. Low-affinity sensors provide greater dynamic range, which is useful for measuring large calcium transients (e.g., from high-frequency spike trains). High-affinity sensors are chosen for generating large amplitude fluorescence changes enabling the detection of small calcium transients (e.g., from single action potentials), but they tend to saturate more easily as they buffer more Ca^{2+} . The kinetics of the indicator depends on the calcium extrusion but also on the cell size and the buffering properties of the calcium indicator. Due to the fact that the calcium indicator acts as an additional calcium buffer, calcium transients are reduced and prolonged with increasing concentration. This effect depends on the calcium buffering

capacity (ratio of the change in buffered calcium and the change in free calcium following calcium influx) of the indicator (K_{dye}) and the endogenous calcium binding proteins (K_s).

1.8 Aims of the PhD thesis

The primary somatosensory whisker barrel cortex (S1) is a specialized region in somatosensory cortex responsible for processing whisker sensory information (Woolsey and Van der Loos, 1970; Petersen, 2007; Diamond et al., 2008; Feldmeyer et al., 2013). Excitatory projection neurons in S1 are thought to play important roles in sensory perception and goal-directed behavior by directly connecting diverse cortical and subcortical areas (Chen et al., 2013, 2015; Yamashita et al., 2013; Kwon et al., 2016; Yamashita and Petersen, 2016). However, many aspects of the anatomical and functional organization of these inter-areal connections are unknown.

Anterograde tracers have been used to track long-range axonal projections from S1 to other brain areas, and axons were found in several locations (White and DeAmicis, 1977; Welker et al., 1988, 1996; Aronoff et al., 2010; Zakiewicz et al., 2011; Zingg et al., 2014). It has been observed that long-range projections of neocortical excitatory neurons vary according to the layer in which the cell body is located (Harris and Shepherd, 2015; Zeng and Sanes, 2017). Pyramidal neurons located in L5/6 of the neocortex send their axons to many cortical and subcortical targets, whereas, currently there is no study on long-range projections of L2/3 pyramidal neurons. Thus, in the first part of my thesis I investigate long-range axonal projections of layer 2/3 excitatory neurons with cell bodies located in S1.

The execution of a goal-directed behavior requires the brain to process incoming sensory information from the environment, and then transfer it to other brain areas through excitatory long-range projection neurons, in order to perform specific motor actions. Cortico-cortical communication in the context of goal-directed sensorimotor transformation has begun to be studied (Chen et al., 2013; Chen et al., 2015; Kwon et al., 2016; Yamashita & Petersen, 2016), but little is known about how signaling between interconnected cortical areas is modified by learning (Holtmaat & Caroni, 2016), as well as in response to changes in reward contingencies. Hence, in the second part of my thesis, I study the function of a subset of S1 cortico-cortical long-range projection neurons during a whisker and auditory task. Using transgenic mice expressing GCaMP6f

combined with two-photon microscopy and retrograde labeling techniques, I chronically monitored the activity of excitatory layer 2/3 neurons in S1 projecting to whisker motor cortex (M1p) or secondary somatosensory cortex (S2p), while mice learned the whisker and auditory task.

In this task, at the first part of training, mice learned to lick a water reward spout in response to detected auditory stimuli. After several days of training in the auditory detection task, whisker stimuli were introduced in randomly interleaved trials. Licking in response to whisker stimuli were also rewarded, and mice rapidly learned to lick on both whisker and auditory trials. Subsequently, when mice were experts in the detection of both sensory modalities, they underwent 2 days of extinction learning on whisker trials, in which licking in response to whisker stimulation was not rewarded. Finally, reward was reinstated in whisker trials. The first part of training, in which mice learned the detection of only auditory stimuli, was implemented in order to establish a stable baseline behavior before the phase of whisker detection learning. During this first phase, mice are habituated onto the behavioral setup, and are engaged into the behavioural training procedure, in which they learn how to lick from the water spout in response to detected stimuli of a different sensory modality than tactile. In this way, we wanted to dissociate from reward-based tactile associative learning possible effects caused by habituation learning on the setup under head-restrained conditions, as well as lick learning from the water spout. In addition, auditory detection during the whole training process enable us to control for sessions of unexpected behavioral performance, for example sessions in which mice were not thirsty, thus were not motivated to perform the task for water reward (e.g after a short break of 1-2 sessions of unrestricted access to water), or extinction sessions in which mice could possibly lose motivation after a number of unrewarded trials.

In order to better understand the function S2p and M1p neurons in S1 during goal-directed behavior, and how this is modified by learning, analysis of the results was based on answering the following questions:

- How whisker and auditory stimulus are represented by S2p and M1p L2/3 neurons in S1 in mice performing the whisker and auditory detection task?
- How licking behavior affects S2p and M1p sensory evoked responses?
- How spontaneous unrewarded licking is represented by S2p and M1p neurons in S1?

- Does learning affect S2p and M1p neuronal responses?
- How stable is the activity of these two cell types across training sessions?
- How stable is the activity of these two cell types under different reward conditions?

Chapter 2

Diverse long-range axonal projections of excitatory layer 2/3 neurons in mouse barrel cortex

The text of this chapter directs to the following published journal article:

Yamashita, T., Vavladeli, A., Pala, A., Galan, K., Crochet, S., Petersen, S. S. A. and Petersen, C. C. H. (2018). Diverse long-range axonal projections of excitatory layer 2/3 neurons in mouse barrel cortex. Frontiers in Neuroanatomy 12, 33.

My contribution to this work was the study of axonal projections of L2/3 neuronal populations based on viral injections. In particular, I performed neuronal labeling, sample preparation, as well as data analysis of population data.

Abstract

Excitatory projection neurons of the neocortex are thought to play important roles in perceptual and cognitive functions of the brain by directly connecting diverse cortical and subcortical areas. However, many aspects of the anatomical organization of these interareal connections are unknown. Here, we studied long-range axonal projections of excitatory layer 2/3 neurons with cell bodies located in mouse primary somatosensory barrel cortex (wS1). As a population, these neurons densely projected to secondary whisker somatosensory cortex (wS2) and primary/secondary whisker motor cortex (wM1/2), with additional axon in the dysgranular zone surrounding the barrel field, perirhinal temporal association cortex and striatum. In three-dimensional reconstructions of 6 individual wS2-projecting neurons and 9 individual wM1/2-projecting neurons, we found that both clas-

ses of neurons had extensive local axon in layers 2/3 and 5 of wS1. Neurons projecting to wS2 did not send axon to wM1/2, whereas a small subset of wM1/2-projecting neurons had relatively weak projections to wS2. A small fraction of projection neurons solely targeted wS2 or wM1/2. However, axon collaterals from wS2-projecting and wM1/2-projecting neurons were typically also found in subsets of various additional areas, including the dysgranular zone, perirhinal temporal association cortex and striatum. Our data suggest extensive diversity in the axonal targets selected by individual nearby cortical long-range projection neurons with somata located in layer 2/3 of wS1.

1.1 Introduction

The mouse primary somatosensory barrel cortex (wS1) is an anatomically-defined brain region specialized in processing whisker sensory information (Woolsey and Van der Loos, 1970; Petersen, 2007; Diamond et al., 2008; Feldmeyer et al., 2013). Excitatory projection neurons in wS1 make monosynaptic connections to other neurons in many parts of the brain where sensory information is further processed to achieve sensory perception and sensorimotor coordination required for specific behaviors (Ferezou et al., 2007; Mao et al., 2011; Chen et al., 2013, 2015; Yamashita et al., 2013; Guo et al., 2014; Sippy et al., 2015; Kwon et al., 2016; Yamashita and Petersen, 2016). However, little is currently known about the anatomical organization of these inter-areal connections. Single-cell reconstructions of wS1 neurons in previous studies rarely revealed axonal morphology outside of wS1 (Zhang and Deschênes, 1997; Brecht et al., 2003; Petersen et al., 2003; Bruno et al., 2009; Oberlaender et al., 2011; Pichon et al., 2012; Narayanan et al., 2015). Recently, using a brain-wide imaging system (Gong et al., 2016), the whole axonal structure of more than 100 cortico-fugal projection neurons in layers 5 and 6 (L5/6) of wS1 were reconstructed at the single-cell level to reveal their axonal projection patterns and target preferences (Guo et al., 2017). However, to date, only two long-range projection neurons with cell bodies located in L2/3 of wS1 have been fully reconstructed (Yamashita et al., 2013). The target locations and density of long-range axonal arborizations of wS1 L2/3 projection neurons thus remain to be elucidated.

In previous anatomical studies, anterograde tracers have been injected into rodent wS1 and long-range axonal projections were found in ipsilateral whisker motor cortex, orbitofrontal cortex, whisker secondary somatosensory cortex, a dysgranular zone sur-

rounding wS1, perirhinal temporal association cortex, dorsolateral striatum, thalamus, zona incerta, anterior pretectal thalamus, superior colliculus and pontine nuclei, along with a contralateral projections to somatosensory cortex, perirhinal temporal association cortex, striatum and spinal trigeminal nuclei (White and DeAmicis, 1977; Chapin et al., 1987; Hoogland et al., 1987, 1991; Welker et al., 1988, 1996; Koralek et al., 1990; Fabri and Burton, 1991; Deschênes et al., 1998; Kim and Ebner, 1999; Veinante et al., 2000; Miller et al., 2001; Hoffer et al., 2003, 2005; Aronoff et al., 2010; Zakiewicz et al., 2011; Oh et al., 2014; Zingg et al., 2014). The long-range projections of neocortical excitatory neurons vary according to the layer in which the cell body is located (Larsen et al., 2008; Harris and Shepherd, 2015; Zeng and Sanes, 2017). Whereas infragranular (L5/6) pyramidal neurons project to many cortical and subcortical targets, L2/3 pyramidal neurons are only thought to project to other cortical regions and striatum. On the other hand, excitatory L4 neurons are considered local interneurons lacking long-range projections. Here, we used *Rasgrf2*-dCre mice (Harris et al., 2014; Madisen et al., 2015) to specifically investigate the long-range axonal projections of L2/3 neurons in wS1, finding multiple targets across cortex and striatum, consistent with current understanding. Individual L2/3 projection neurons could send axon to one specific target, or single L2/3 neurons could project to multiple targets. To begin to address this question, we labeled single L2/3 wS1 neurons in vivo, and, after fixation and staining, we traced their axonal and dendritic arborisations, finding extensive diversity in their long-range axonal projections, with some neurons projecting strongly to multiple targets.

1.2 Materials and methods

All animal procedures were performed in accordance with protocols approved by the Swiss Federal Veterinary Office.

2.2.1 Viral injections and histological analysis

Male adult 8- to 10-week-old *Rasgrf2*-dCre mice (Harris et al., 2014; Madisen et al., 2015) were implanted with a light-weight metal head-holder and a chamber under isoflurane anesthesia. The location of the left wS1-C2 barrel column was functionally identified through intrinsic optical imaging as previously described (Ferezou et al., 2007). For selective labeling of wS1 L2/3 pyramidal neurons, AAV9.CAG.Flex.tdTomato.WPRE.bGH

(25 nl of 1:10 dilution of virus with an initial titer of 2.7×10^{13} viral genome copies / ml) was injected into the left wS1-C2 barrel column of Rasgrf2-dCre mice, at the depth of 200–250 μ m. Subsequently, dCre recombinase activity was induced by intraperitoneal injection of trimethoprim (TMP) (0.25 mg/g body weight) for 3 consecutive days. After injection of AAV, the craniotomy was covered with a silicone elastomer (Kwik-Cast, WPI) and a layer of dental cement added over the elastomer, and the animals were returned to their home cages. The virus was allowed to express for 25–28 days in order to achieve strong labeling of axons. After transcardial perfusion and postfixation for 8–12 h using 4% paraformaldehyde in 0.1 M phosphate buffer (pH 7.4), we cut the fixed brains in coronal slices on a vibratome Leica VT1000 (section thickness: 100 μ m). Slices were mounted on Superfrost slides using DABCO.

2.2.2 Imaging and processing of brain sections

Brain sections were imaged with an automated slide scanner (VS120 Virtual Slide, Olympus) using a 10x objective lens so that overall morphology as well as labeled neurons and axons could be seen. Identified locations of axonal projections of labeled L2/3 neurons in wS1-C2 were further imaged with a confocal laser-scanning microscope (ZEISS LSM-700) using a 20x objective lens to achieve improved image resolution. The alignment of z-stack image slices was performed with MultistackReg v1.45 plugin, which is based on Turboreg ImageJ plugin (Thévenaz et al., 1998) for stack registration of multiple image channels. The digital z-stack image series of whole-brain fluorescence is available at the CERN database Zenodo (<https://zenodo.org/communities/petersen-lab-data>) with direct link <http://doi.org/10.5281/zenodo.1220711>.

2.2.3 Single-cell electroporation, staining and tracing of neuritis

Male adult 8- to 15-week-old C57BL6J mice were implanted with a light-weight metal head-holder and a chamber under isoflurane anesthesia. The location of the left wS1-C2 barrel column was functionally identified through intrinsic signal optical imaging as previously described (Ferezou et al., 2007). In some experiments, secondary whisker somatosensory cortex (wS2) of the left hemisphere was also identified with intrinsic optical imaging (Yamashita et al., 2013). For retrograde labeling of wS1 projection neurons, cholera toxin subunit B (CTB) conjugated with Alexa-Fluor 594 (0.5%, weight/volume, Invitrogen) was injected into primary whisker motor cortex (wM1: 1 mm anterior, 1 mm lat-

eral from Bregma; Sreenivasan et al., 2016) of the left hemisphere or left wS2 (Yamashita et al., 2013). Injection volume of the CTB solution was 50 nl for wM1 and 25 nl for wS2 at the depths of 300 and 800 μm , giving a total volume of 100 nl for wM1 and 50 nl for wS2. After injection of CTB, the craniotomy was covered with a silicone elastomer (Kwik-Cast, WPI) and a layer of dental cement added over the elastomer, and the animals were returned to their home cages.

In vivo electroporation was targeted to a single CTB-labeled neuron per mouse in the center of the C2 barrel column 6–9 days after CTB injection under isoflurane anesthesia (Yamashita et al., 2013; Pala and Petersen, 2015). Glass pipettes having resistances of 10–17 M Ω were filled with a solution containing (in mM): 135 potassium gluconate, 4 KCl, 10 HEPES, 10 sodium phosphocreatine, 4 MgATP, 0.3 Na3GTP (adjusted to pH 7.3 with KOH) to which 100 μM Alexa 488 and 5–10 ng/ μl of pCAG-EGFP plasmid DNA (Addgene plasmid 11150, kindly provided by Connie Cepko) were added. A small craniotomy (around 1 mm in diameter) was made over the wS1-C2 barrel column without durotomy. Using shadow imaging under two-photon microscopy (Kitamura et al., 2008), the pipettes were brought into close contact with the cell body of the CTB-labeled neuron and 50 pulses of negative voltage step (0.5 ms, -10 V) were delivered at 50 Hz using a pulse generator (Axoporation 800A, Molecular Devices). The craniotomy was then covered with a silicone elastomer (Kwik-Cast, WPI) and animals were returned to their home cages for 3–4 days before perfusion.

After transcardial perfusion and postfixation for 2–4 h using 4% PFA, we cut the fixed brains in coronal slices on a vibratome Leica VT1000 (section thickness: 80 μm). Slices were washed in PBS (0.9% NaCl, 0.01 M phosphate buffer, pH 7.4) for 10 min, and endogenous peroxidases were then quenched by 15 min incubation with 0.3% H2O2. The slices were subsequently washed three times with 2% normal goat serum (NGS) and 0.5% Triton X-100 and then incubated with primary anti-GFP antibody (rabbit polyclonal, 1:500) together with 2% NGS and 0.5% Triton X-100 for 4 days at 4°C. The slices were then washed with PBS containing 2% NGS and 0.5% Triton X-100 and further incubated with biotinylated goat antibody against rabbit IgG (1:500) together with 2% NGS and 0.5% Triton X-100 for 1.5 hr. The slices were then rinsed in PBS three times and were conjugated with avidin-biotinylated peroxidase following the manufacturer's instructions (Vectastain, Vector Labs) for 1.5 h. Slices were then washed three times with PBS, and subsequently GFP-expressing neurons were visualized under a reaction with 0.4 mg/ml DAB and 0.03% H2O2 for 10 min. The reaction was stopped by rinsing the

sections in PBS. Finally, the slices were mounted on gelatinised Superfrost slides using Mowiol. Axonal and dendritic processes were subsequently reconstructed from the serial sections using Neurolucida software (MBF Bioscience).

The DAB-stained neurons were reconstructed using an Olympus BX51WI microscope using an oil 60x lens (Olympus PlanApo 60x Oil NA 1.42) along with Neurolucida 64 bit software (version 11.09, MBF Biosciences). Students from the EPFL Faculty of Life Sciences were trained to become experts at neuronal reconstruction. The S2p and M1p neurons were distributed blindly to the students to avoid bias. Brain slice contours, somas, dendrites and axons were reconstructed in each brain slice, and then aligned and stitched with neighboring sections to give a complete 3D dataset using the “serial section manager” function of Neurolucida. Throughout the entire process of the reconstruction, thorough quality control was performed, checking for accuracy in x, y and z-axes, general alignment and completeness. Quality control was carried out by an independent team member and, in addition to checking the correctness of the traced axon in three dimensions through digital superposition upon the stained axon in the section, we also searched all adjacent fields of view for additional axon, and at lower magnification we re-examined the entire section. Nonetheless, we cannot exclude that some axons might have been incompletely traced, and it is likely that some axons were incompletely labeled. Analysis of dendritic and axonal structure was carried out in Neurolucida Explorer. All values are presented as mean \pm SD. The digital neuronal reconstructions of all neurons together with the associated brain contours are freely available at the CERN database Zenodo (<https://zenodo.org/communities/petersen-lab-data>) with direct link <http://doi.org/10.5281/zenodo.1220711>. The data have also been submitted to [NeuroMorpho.Org](#) (Akram et al., 2018).

1.3 Results

2.3.1 Viral expression of tdTomato to label neurons in L2/3 of wS1

We bred Rasgrf2-dCre mice (Harris et al., 2014; Madisen et al., 2015) together with LSL-tdTomato reporter mice (Madisen et al., 2010) and injected trimethoprim to induce recombinase activity. In agreement with previous reports (Harris et al., 2014; Madisen et al., 2015), we found that tdTomato-expressing cells were almost exclusively restricted to

L2/3 with a large fraction of neurons being labeled in that cortical layer (**Figure 1.a**). We localized the C2 whisker representation in barrel cortex of Rasgrf2-dCre mice using intrinsic signal optical imaging (Grinvald et al., 1986; Ferezou et al., 2007) and targeted that location with an injection of an adenoassociated virus expressing tdTomato in a Cre-dependent manner (AAV-FLEX-tdTomato). After 25-28 days, the mice were perfused with PFA and the fixed brain cut into 100 μ m thick coronal sections. In 5 mice, neuronal somata expressing tdTomato were highly localized in a small region of wS1 and restricted to L2/3 neurons (**Figure 2.1.b**). Hot-spots of long-range axonal projections from these L2/3 neurons were identified across mice in striatum and various cortical regions (**Figures 2.1, 2.2**). The estimated centers of these hot-spots of axon were computed as mean \pm standard deviation ($n = 5$ mice) relative to the injection site (targeted to the C2 barrel column) (**Figure 2.2.c, Table 2.1**) or relative to Bregma according to the reference frame of a standard mouse brain atlas (Paxinos and Franklin, 2001) (**Figure 2.2.d, Table 2.1**).

In frontal cortex, we found an elongated column of dense axonal arborisations in wM1, with less dense axon extending anteriorly into secondary whisker motor cortex (wM2) (**Figures 2.1.d, 2.1.f**). We were not able to resolve separation of axonal arborisations in wM1 and wM2. The wM1/2 projection extended from $\sim 1.98 \pm 0.39$ mm to $\sim 0.36 \pm 0.05$ mm anterior to Bregma as a column of axon about ~ 0.8 mm lateral of the midline, in agreement with previous findings (Sreenivasan et al., 2016). The center of wM1/2 projection was estimated to be located at 2.70 ± 0.09 mm anterior and 2.21 ± 0.12 mm medial relative to the wS1 injection site (**Figure 2.2.c, Table 2.1**) or 1.04 ± 0.09 mm anterior and 0.81 ± 0.09 mm lateral relative to Bregma (**Figure 2.2.d, Table 2.1**).

There was further dense axonal labeling in a location ~ 1 mm lateral to the viral injection site (**Figure 2.1.c**), consistent with the expected location of secondary whisker somatosensory cortex (wS2). We found that wS2 was located at 0.02 ± 0.05 mm anterior and 0.82 ± 0.06 mm lateral relative to the injection site (**Figure 2.2.c, Table 2.1**); equivalent to 1.63 ± 0.11 mm posterior and 3.83 ± 0.06 mm lateral relative to Bregma (**Figure 2.2.d, Table 2.1**). Posterior to wS2, we found two additional more weakly labeled zones, which we termed the posterolateral regions (PL1 and PL2) (**Figures 2.1.i, 2.1**).

We found additional hotspots of axon in a region immediately medial to the barrel field, termed the dysgranular zone (Koralek et al., 1990; Veinante and Deschênes, 2003). One such projection zone was located just anterior and medial to the barrel field and we therefore denote this region as the anteromedial (AM) dysgranular zone (**Figures**

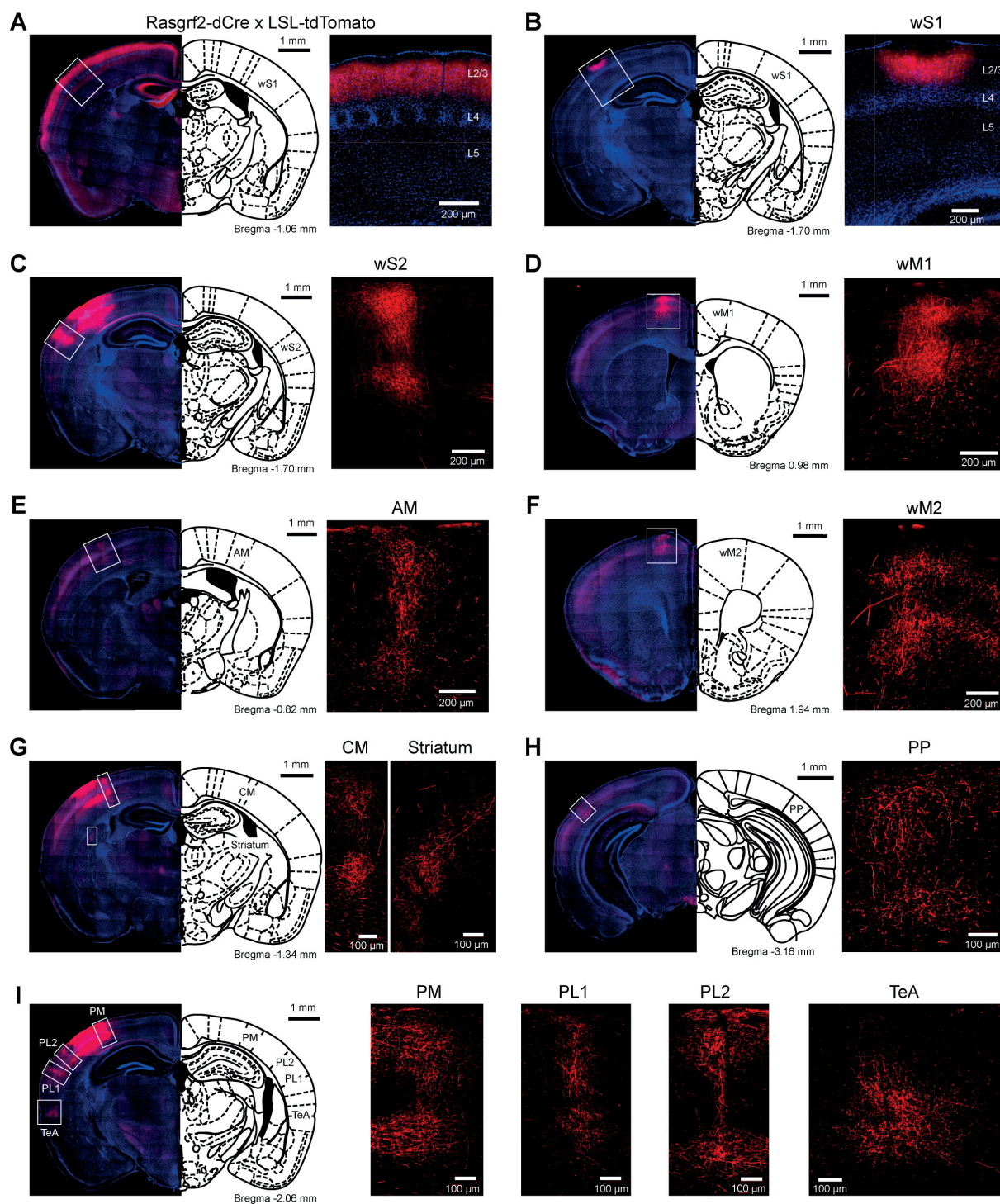


Figure 2.1: Selective labeling of wS1 L2/3 neurons and their long-range axonal projections. (a) L2/3 neurons selectively expressed tdTomato in Rasgrf2-dCre mice crossed with LSL-tdTomato mice. (b) An example injection of AAV-FLEX-tdTomato targeted to the C2 whisker representation of Rasgrf2-dCre mice to express tdTomato in L2/3 neurons of wS1. (c–i) In the same mouse as panel B, increasing the camera exposure time allowed axonal fluorescence to be observed in wS2 (c), wM1 (d), AM (e), wM2 (f), CM and striatum (g), a posterior region (PP) presumably overlapping with visual cortex (h), and PM, PL1/2 and TeA (i).

2.1.e, 2.2; Table 2.1). Slightly posterior and medial to this region, we found another hotspot of axon, which we label centromedial (CM) dysgranular (**Figures 2.1.g, 2.2; Table 2.1**), and further posteriorly there was a hotspot of axon in a posteromedial (PM) dysgranular zone (**Figures 2.1.i, 2.2; Table 2.1**). These areas were not completely segregated, and the locations represent estimated local peaks in the spatial density of axon.

Further posteriorly, presumably overlapping with visual areas (Wang and Burkhalter, 2007; Olcese et al., 2013), we found a weak axonal projection to a region we term PP (Posterior to PL1/2) (**Figure 2.1.h**), located at 1.49 ± 0.22 mm posterior and 0.49 ± 0.04 mm lateral relative to the injection site (**Figure 2.2.c, Table 2.1**), and 3.14 ± 0.25 mm posterior to Bregma and 3.51 ± 0.03 mm lateral of the midline (**Figure 2.2.d, Table 2.1**).

An important further locus of relatively high density axon was found in a region near the rhinal sulcus, typically labeled as perirhinal temporal association cortex (TeA) (Paxinos and Franklin, 2001; **Figure 2.1.i**). The projection zone was centered at around 2.01 ± 0.07 mm posterior to Bregma and 4.45 ± 0.06 mm lateral of the midline (**Table 2.1**), with a long extent along the anterior-posterior axis from $\sim 1.50 \pm 0.30$ mm to $\sim 2.20 \pm 0.30$ mm posterior to Bregma (**Figure 2.2.b**).

The dorsolateral striatum was the only subcortical region in which we observed axon originating from L2/3 wS1 neurons (**Figure 2.1.g**). The projection was centered at around 1.36 ± 0.10 mm posterior to Bregma and 2.83 ± 0.12 mm lateral of the midline (**Table 1**). The axonal density in the striatum varied across the dorsolateral striatum and extended from $\sim 0.30 \pm 0.20$ mm to $\sim 1.70 \pm 0.10$ mm posterior to Bregma, which roughly corresponds to the area where neurons with functional responses to somatosensory stimuli were previously reported (Reig and Silberberg, 2014; Sippy et al., 2015).

Whereas the callosal axonal fiber tract was brightly fluorescent, we found only a low density of axon distributed across a broad area of contralateral somatosensory cortex. The corpus callosum could present a diffusional barrier, and it is possible that contralateral axonal arborisations were not completely filled with tdTomato. Because of the paucity of contralateral labeling, we did not further investigate contralateral axon.

2.3.2 Single-cell anatomy of neurons retrogradely labeled from wS2

In agreement with previous studies, our viral tracing data suggest that the two cortical regions receiving the most prominent axon from wS1 were the frontal region wM1 and

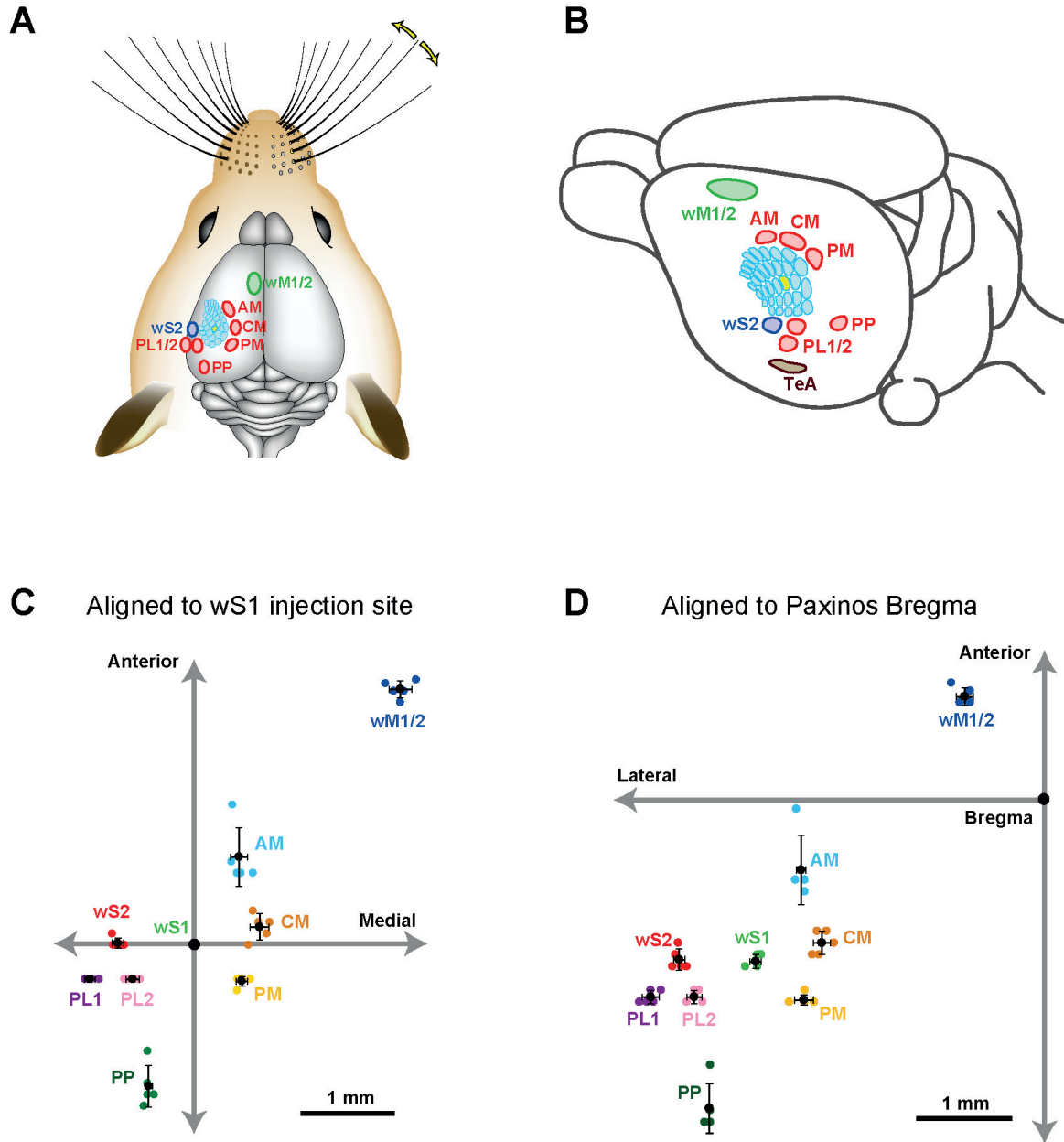


Figure 2.2: Hotspots of axonal projections of wS1 L2/3 neurons in dorsal sensorimotor cortex. (a) Schematic drawing showing the approximate locations of the major hotspots of long-range axon in the dorsal cortex from wS1 L2/3. (b) An oblique view of (a) showing schematic locations of long-range projections. (c) The estimated center of each projection in sensorimotor cortex relative to the center of the injection site in wS1. (d) The estimated center of each projection in sensorimotor cortex relative to the Bregma (Paxinos and Franklin, 2001).

Mean \pm SD (mm)	Relative to wS1 injection site		Relative to Bregma	
	Medio-Lateral	Anterio-Posterior	Medio-Lateral	Anterio-Posterior
wS1	0	0	-3.02 ± 0.06	-1.65 ± 0.07
wS2	-0.82 ± 0.06	0.02 ± 0.05	-3.83 ± 0.06	-1.63 ± 0.11
wM1/2	2.21 ± 0.12	2.70 ± 0.09	-0.81 ± 0.09	1.04 ± 0.09
PL1	-1.12 ± 0.06	-0.36 ± 0.00	-4.13 ± 0.09	-2.01 ± 0.07
PL2	-0.66 ± 0.07	-0.36 ± 0.00	-3.67 ± 0.08	-2.01 ± 0.07
AM	0.48 ± 0.09	0.93 ± 0.31	-2.54 ± 0.05	-0.72 ± 0.35
CM	0.70 ± 0.10	0.19 ± 0.14	-2.32 ± 0.09	-1.46 ± 0.12
PM	0.51 ± 0.06	-0.38 ± 0.05	-2.51 ± 0.10	-2.04 ± 0.05
PP	-0.49 ± 0.04	-1.49 ± 0.22	-3.51 ± 0.03	-3.14 ± 0.25
TeA	-1.43 ± 0.04	-0.36 ± 0.00	-4.45 ± 0.06	-2.01 ± 0.07
Striatum	0.18 ± 0.14	0.29 ± 0.07	-2.83 ± 0.12	-1.36 ± 0.10

Table 2.1: Estimated location of the centers of axonal projections from L2/3 projection neurons located in primary somatosensory cortex labeled through injection of AAV virus targeted to the C2 whisker representation across 5 mice.

the lateral region wS2. In order to label neurons projecting to wS2 and wM1, we injected the fluorescent retrograde tracer, cholera toxin subunit B (CTB) conjugated to Alexa fluorophores into the target zone, and allowed 6–9 days for retrograde transport. Targeting the C2 barrel column through intrinsic signal optical imaging, we then electroporated DNA encoding GFP into single CTB-labeled projection neurons in L2/3 of wS1 under visual control offered by a two-photon laser scanning microscope (Kitamura et al., 2008; Yamashita et al., 2013; Pala and Petersen, 2015). After allowing several days for expression and diffusion, the mice were perfused with PFA and the fixed brains sectioned coronally. DAB-visualized GFP-antibody staining revealed extensive dendritic and axonal arborisations of single neurons ($n = 15$ in total), which were traced in three dimensions across consecutive sections.

We first reconstructed 7 single neurons in L2/3 wS1, which had been selected based on retrograde fluorescent labeling of CTB injected into wS2 (**Figures 2.3, 2.4**). All these neurons had axonal processes in wS2, consistent with the retrograde CTB labeling. Six of the seven neurons had rich arborisations in wS2, and we term these neurons as wS2-projecting (S2p). The other neuron (neuron TY369) had a more prominent axonal projection to wM1 compared to wS2, and we therefore classified this neuron as wM1-projecting (M1p). In addition to projecting to wM1/2, this M1p neuron also sent axon to posterior and lateral areas consistent with the location of PL and PP. All of the S2p neurons had extensive local axon in wS1 of L2/3 and L5 (**Figures 2.3, 2.4**). This pattern is consistent with previous reports of axonal structure of individual L2/3 neurons labeled in brain slices (Feldmeyer et al., 2006; Larsen and Callaway, 2006). Typically one or more branches of the local L5 axon traveled through L5/6 to wS2, where it formed a branching column of axon in wS2. The axon of one of the S2p neurons (neuron AP049, **Figure 2.4.a**) predominantly made arborisations in superficial layers, whereas the axon branches of another S2p neuron (neuron AP046, **Figure 2.4.b**) were predominantly found in deep layers (**Figure 2.4**). The region with the densest axonal arborisations of these neurons appears to correspond to wS2 (**Figure 2.4**). However one neuron (AP046, **Figure 2.4.b**) appeared to primarily target a more posterior region, perhaps corresponding to PL1/2. In addition to wS2, three of these S2p neurons (neuron AP046, **Figure 2.4.b**; neuron AP047, **Figure 2.4.c**; neuron TY300, **Figure 2.4.d**) also projected to a posterior and medial region, consistent with the location of PM in the dysgranular zone. In one S2p neuron (neuron AP049; **Figures 2.3, 2.4.a**) we found extensive axon in dorsolateral striatum (**Figure 2.3**). Five S2p neurons had a callosal axon reaching the midline, and one S2p neuron (AP049) had axon in the external capsule, but did not reach the midline. Typically, we were not able to follow the axon across the corpus callosum, and we found very little axon labeled on the contralateral hemisphere.

2.3.3 Single-cell anatomy of neurons retrogradely labeled from wM1

Next, we traced the axonal and dendritic arborisations from 8 wS1 neurons which had been retrogradely labeled by injection of CTB into wM1, targeted through stereotactic coordinates of 1 mm anterior and 1 mm lateral to Bregma (Sreenivasan et al., 2016).

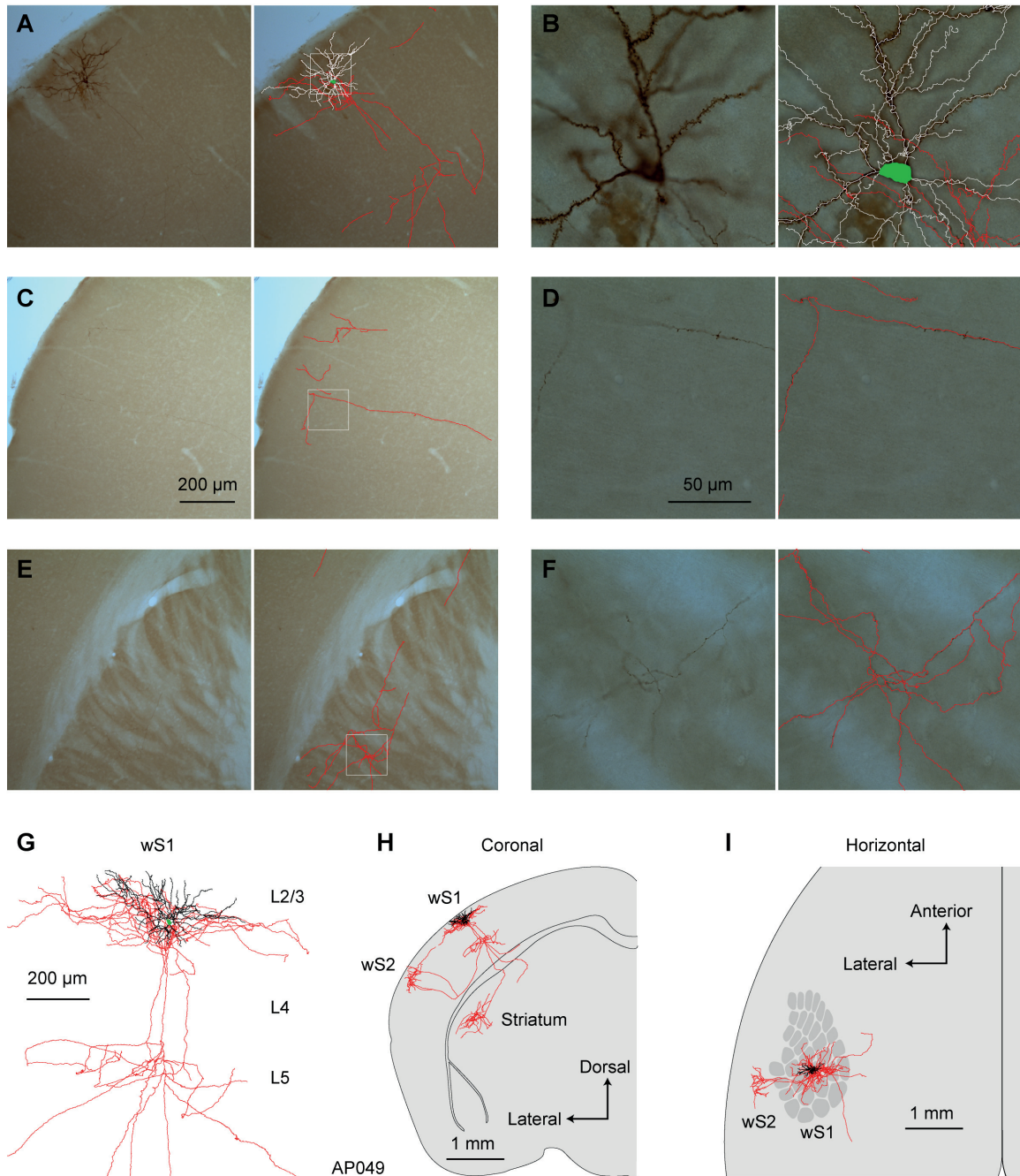


Figure 2.3: Morphology of an individual S2p neuron. (a) The dendrites, soma and local axonal arborisations in wS1 of an example neuron (AP049) viewed at low magnification (left) with 3D reconstruction of neurites in that section superimposed (right; red: axon; white: dendrite; green: soma). (b) At higher magnification in wS1, spines become obvious on dendrites, and the axon can be seen to be labeled with high-contrast at a specific facial plane (left). The 3D tracing of the whole section was superimposed (right). (c) Same as (a), but in wS2. (d) Same as (b), but for wS2 (e) Same as (a), but in dorsolateral striatum. (f) Same as (b), but in dorsolateral striatum. (g) Local axon, dendrite and soma of this neuron. (h) Coronal projection of this neuron's structure. (i) Horizontal projection of this neuron's structure. The wS1 barrel field is schematically indicated.

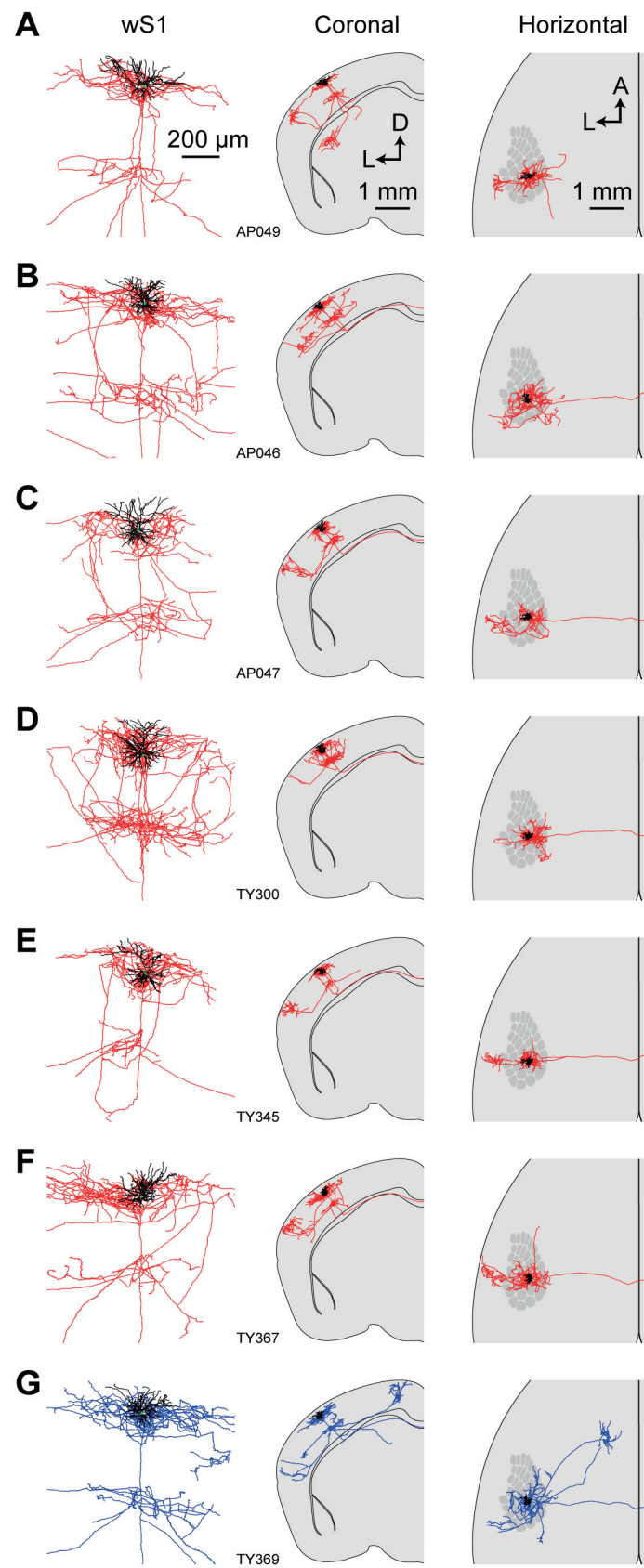


Figure 2.4: Axonal and dendritic structure of neurons retrogradely-labeled from wS2. (a-g) Dendritic (black) and axonal (red in a–f, blue in G) arborisations of different individual neurons viewed locally in wS1 (left), in coronal projection (center) and in horizontal projection (right). The wS1 barrel field is schematically indicated (right).

Similar to S2p neurons, these neurons also had extensive local axonal arborisations in L2/3 and L5 (**Figures 2.5, 2.6**). All neurons had axon projecting to the frontal cortex, and typically had extensive axonal branching in wM1 and wM2. However, one neuron (TY288, **Figure 2.6.d**) had a long axonal projection without extensive branching in any specific target within the frontal cortex. In addition to projecting to wM1, one neuron (TY220, **Figure 2.6.b**) also projected strongly to TeA. Another M1p neuron (TY310, **Figure 2.6.f**) projected to the dorsolateral striatum. Interestingly, this neuron also extended a long-range axon to the most anterior and dorsal aspect of the amygdala, but did not appear to branch in this region. Most M1p neurons (7 out of 9 cells) projected to one or more targets other than wM1/2, with several neurons showing a relatively dense axon in CM and PM (for example, neurons TY220, TY288 and TY302; **Figures 2.6.B, 2.6.D, 2.6.E**). Among the 9 M1p neurons, callosal axonal projections could be traced across the midline for three neurons, but typically we lost the axon in the callosum. In one neuron (AP042) the axon reached the external capsule, but we could not follow it to the midline. Five neurons did not appear to have a callosally-projecting axon. It is thus possible that some M1p neurons do not project to the contralateral hemisphere, however, as mentioned earlier, we are concerned about the completeness of the labeling of callosal axons.

2.3.4 Comparison of M1p and S2p neurons

In order to gain a visual impression of the differences in the axonal projections of M1p and S2p neurons, we overlaid 2D projections of the traced neurons of each group separately. Locally in wS1, dense axon is present in L2/3 and L5, appearing to be less dense in L4 and L6 (**Figure 2.7.a**). For S2p neurons viewed in a coronal projection, an obvious column of axons is located lateral to wS1 consistent with the location of wS2, whereas M1p neurons send their axon to a more medial column, consistent with the location of wM1 (**Figure 2.7.b**). Viewed in a horizontal projection, the axonal projections of S2p neurons are targeted prominently to wS2, ~1 mm directly lateral to the injection site of the C2 whisker representation in wS1 (**Figure 2.7.c**). Dense axonal arborisations of

M1p neurons were seen in a frontal region centered ~1 mm anterior and ~1 mm lateral to Bregma, consistent with the location of wM1 (**Figure 2.7.c**).

We quantified total dendritic length (S2p: 8.1 ± 0.8 mm, $n = 6$ cells; M1p: 8.5 ± 0.7 mm, $n = 9$ cells), the number of dendritic trees attached to the soma (S2p: 8.3 ± 1.6 , $n = 6$ cells; M1p: 8.0 ± 1.4 , $n = 9$ cells) and the number of dendritic branch points (nodes) (S2p: 64 ± 10 , $n = 6$ cells; M1p: 63 ± 4 , $n = 9$ cells) (**Figure 2.7.d**). We also quantified the total length of traced axon (S2p: 66.7 ± 14.5 mm, $n = 6$ cells; M1p: 80.7 ± 9.9 mm, $n = 9$ cells) (Figure 7E and Supplementary Data File 1).

In order to visualize the diversity of the long-range projection targets of the different neurons, we made a thresholded and color-coded matrix of cell-by-cell axonal length in different brain regions, with each column representing the axon of a single cell. Dark colors show regions where > 10 mm of branching axon was found and light colors indicate > 1 mm of branching axon (**Figure 2.7.f**). For each neuron there was a large length of branching axon in wS1: 41.7 ± 1.1 mm for S2p neurons ($n = 6$) and 40.0 ± 3.8 mm for M1p neurons ($n = 9$) (**Figure 2.7.g**). These axonal lengths are comparable to previous quantifications of axon within wS1 showing: 38.6 mm for L2/3 neurons in rat wS1 (Bruno et al., 2009); 39.8 mm for L2 neurons in rat wS1 (Narayanan et al., 2015); and 49.2 mm for L3 neurons in rat wS1 (Narayanan et al., 2015). S2p neurons on average had 12.2 ± 7.4 mm of branching axon in wS2, whereas M1p neurons only had 1.6 ± 2.7 mm of branching axon in wS2. Conversely M1p neurons had 20.8 ± 11.7 mm of branching axon in wM1/2, whereas the S2p neurons did not have any axon collaterals in this brain region. For each neuron the combined branching axonal length in wS1, wS2 and wM1/2 was $> 75\%$ of the total length of branching axon. Individual neurons could nonetheless have dense axonal arborisations in other specific targets. For example, the striatum received 12.5 mm of branching axon from neuron AP049 and 16.9 mm of branching axon from neuron TY310. TeA received 7.7 mm of branching axon from neuron TY220. The distinction between dysgranular zone and wS1 was unfortunately not clear in these analyses, and therefore we could only make rough estimates of axon length in PL, AM, CM, and PM.

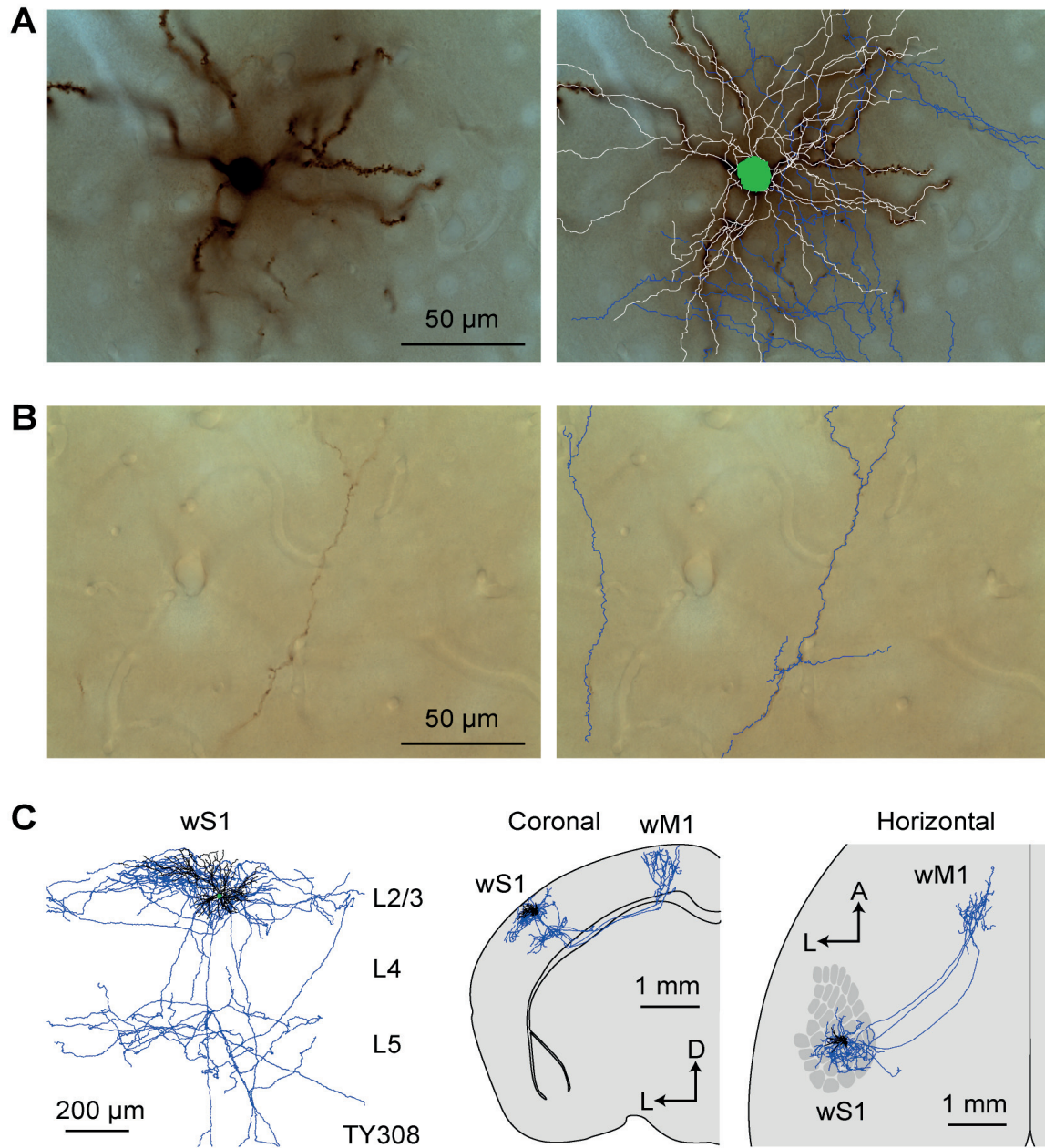


Figure 2.5: Morphology of an individual M1p neuron. (a) The dendrites, soma and local axonal arborisations in wS1 of an example neuron (TY308) (left) overlaid with 3D reconstruction of neurites (right; blue: axon; white: dendrite; green: soma). (b) Example axonal arborisations in wM1 from this neuron (left) overlaid with 3D reconstruction (right). (c) Local axon, dendrites and cell body of this neuron (left). Coronal (middle) and horizontal (right) projection of this neuron's structure together with the schematic wS1 barrel field (right).

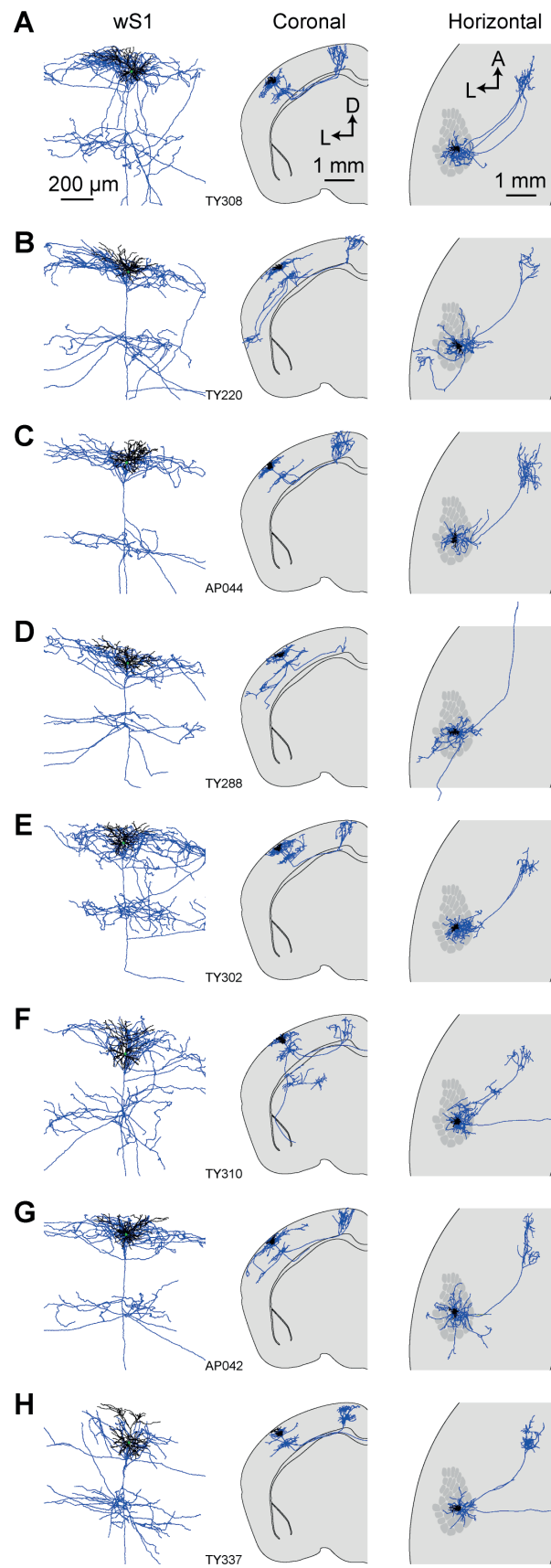


Figure 2.6: Axonal and dendritic structure of neurons retrogradely-labeled from wM1. (a–h) Dendritic (black) and axonal (blue) arborisations of different individual neurons viewed locally in wS1 (left), in coronal projection (center) and in horizontal projection with the schematic wS1 barrel field (right).

1.4 Discussion

Through viral injections we found that excitatory L2/3 pyramidal neurons in wS1 send axon to wS2, wM1/2, several regions of the dysgranular zone, PP, TeA, and striatum. Three-dimensional reconstruction of the axonal projections of individual excitatory L2/3 pyramidal neurons in wS1 revealed extensive diversity, with individual neurons appearing to select subsets of long-range projection targets.

2.4.1 Axonal projections based on viral injections

We specifically studied the projections of L2/3 neurons in wS1 through use of transgenic mice and viral injections targeted to the functionally mapped C2 whisker representation. Long-range axonal projections were found in cortex and striatum, but not in other subcortical brain areas, consistent with current understanding of cortical organization (Harris and Shepherd, 2015; Zeng and Sanes, 2017). In agreement with previous studies without genetically-defined layer-specific labeling (White and DeAmicis, 1977; Welker et al., 1988; Miller et al., 2001; Hoffer et al., 2003, 2005; Aronoff et al., 2010; Zakiewicz et al., 2011), the densest regions of cortical projections appeared to be wS2 and wM1. Important, but less dense, axon was also found in TeA and striatum. Some axon was observed posteriorly in an area we label PP, which is likely part of secondary visual cortex called area RL (Wang and Burkhalter, 2007; Wang et al., 2012) where visual and somatosensory information are integrated (Olcese et al., 2013).

In addition, we found several hotspots of axon in the dysgranular zone surrounding the barrel field, in agreement with previous studies (Broser et al., 2008). These regions surrounding wS1 could in some way be homologous to the regions surrounding mouse V1 (Wang and Burkhalter, 2007; Andermann et al., 2011; Marshel et al., 2011; Glickfeld et al., 2013). Further work is needed to investigate the organization of these target zones in the dysgranular cortex. In future experiments, it would be of great interest to make multiple injections with different colors of tracers to study the

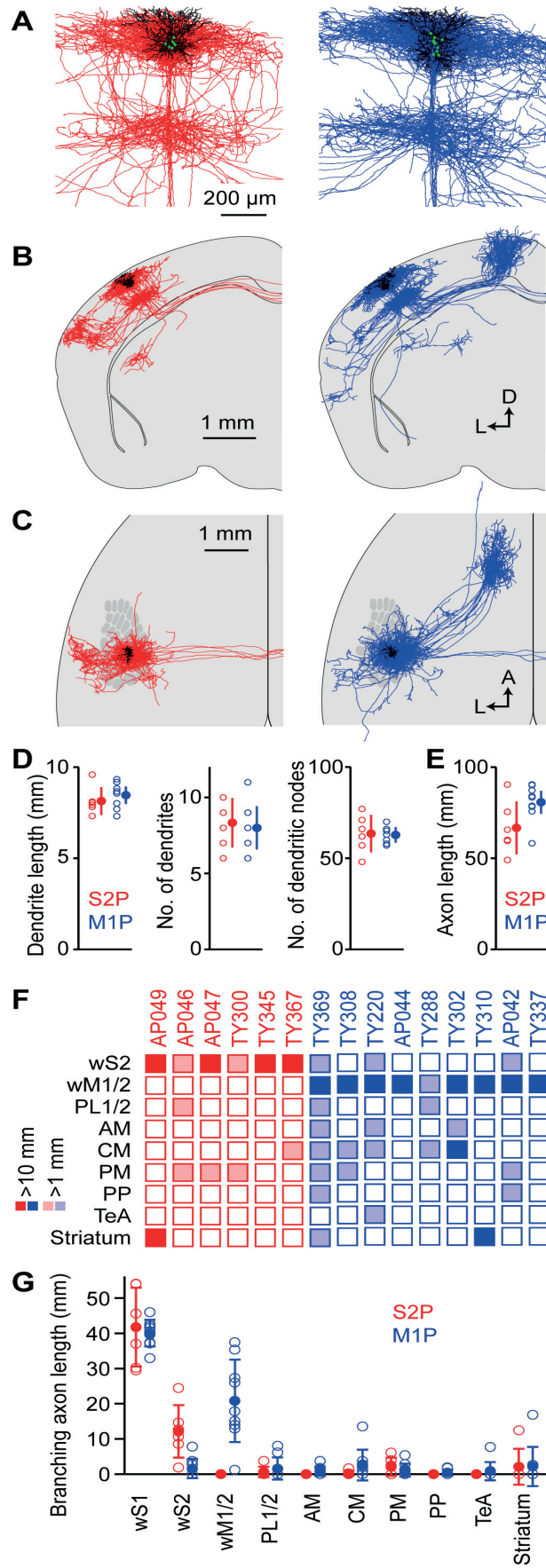


Figure 2.7: Comparison of the structures of S2p and M1p neurons. a) Overlay of dendrites (black) and local axon (red for S2p, blue for M1p) from all S2p (left) and M1p (right) singly-labeled neurons in individual brains. The superimposed neurons were vertically aligned to the pia and horizontally aligned with respect to the main descending axon. b) Overlay of dendrites (black) and axonal structures (red for S2p, blue for M1p) for S2p (left) and M1p (right) neurons shown in coronal projection. c) Same as (b), but in horizontal projection with the schematic wS1 barrel field. d) Quantification of dendritic length (left), number of dendrites emanating from the cell body (center) and number of dendritic branch points (right). e) Quantification of total axonal length for S2p and M1p neurons. f) Thresholded analysis of cell-by-cell axon length in specific targets. Each column represents the axon length of one neuron. Some S2p neurons (red) strongly projected to wS2 and striatum. Some M1p neurons strongly projected to wM1, striatum and CM. Dark colors indicate > 10 mm of branching axon in the target region. Light shading indicates regions with < 10 mm and > 1 mm of axon. g) Quantification of branching axon length in wS1, wS2, wM1/2, PL1/2, AM, CM, PM, PP, TeA, and striatum.

somatotopic map of axonal projections in the various target regions, as was carried out for mouse V1 (Wang and Burkhalter, 2007).

We only found relatively sparse axon in contralateral somatosensory cortex, although the corpus callosum was strongly labeled. It is possible that the callosum presents a diffusional barrier, hindering complete labeling of contralateral axon. Similarly, it is also possible that our labeling of axons in other brain regions is incomplete. In the future, it will therefore be important to compare the completeness of different labeling methods.

2.4.2 Axonal projections of individual S2p and M1p neurons

At the single cell level, little is known about the brain-wide anatomical structure of long-range projection neurons of mouse wS1, especially that of L2/3 projection neurons (Yamashita et al., 2013; Guo et al., 2017). Here, we targeted our investigations to L2/3 pyramidal neurons retrogradely-labeled from wM1 and wS2 with cell-bodies located in the C2 barrel column of wS1 (Yamashita et al., 2013). All neurons sent axonal projections near to the injection site of the retrograde label. In addition, many neurons also sent long-range axonal projections to several other brain regions, including several sub-regions of the dysgranular zone, TeA and striatum.

Individual neurons appeared to select subsets of projection targets (Figure 7). For example, neurons in our data sample largely targeted their axons toward either wM1/2 or wS2. Neurons classified as S2p neurons appeared not to send their axon to wM1/2, whereas some M1p neurons had relatively weak projections to wS2. Some

S2p/M1p neurons projected strongly to striatum or TeA, but most S2p/M1p neurons did not send any axon to these regions. Our results thus indicate substantial anatomical diversity in the long-range projections of L2/3 neurons in wS1. It is possible that M1p neurons might have more diverse projection targets compared to S2p neurons (**Figure 2.7.f**), but our sample size is too small to characterize target preferences of these neurons to any degree of detail. New methods are therefore required to obtain much larger datasets. Imaging axonal and dendritic fluorescence from individual neurons across entire intact brains is now becoming possible (Economo et al., 2016; Gong et al., 2016; Guo et al., 2017). Methods for automated computer reconstruction of neuronal processes from 3D image stacks are also improving (Tomer et al., 2014; Kasthuri et al., 2015; Susaki et al., 2015; Renier et al., 2016; Seiriki et al., 2017). These technical developments provide hope that in the future it will be possible to gather datasets with much larger numbers of neurons, which appears to be required to investigate the diversity of neocortical projection neurons in wS1.

Current evidence suggests that S2p and M1p neurons might form largely non-overlapping classes of L2/3 projection neurons in wS1. Previous studies injecting retrograde labels in wM1 and wS2 found only few double-labeled neurons (Chen et al., 2013; Yamashita et al., 2013). Furthermore, gene-expression in retrogradely labeled M1p and S2p L2/3 neurons is also different (Sorensen et al., 2015). In general, it will be important to examine to what extent gene-expression correlates with long-range axonal projections, which may help classification of neuronal types. One approach would be to combine Patchseq technology (Cadwell et al., 2016; Fuzik et al., 2016) with brain-wide single-cell anatomy. Another interesting approach is to use DNA barcodes to sequence projections (Kebschull et al., 2016; Han et al., 2018). In general, there are likely to be many subtypes of excitatory neurons in the mammalian neocortex and classifying their structural diversity is of key importance (Harris and Mrsic-Flogel, 2013; Harris and Shepherd, 2015; Zeng and Sanes, 2017).

2.4.3 Limitations and future perspectives

An important limitation of the current study is that we were unable to align the somatotopic organization of the barrel map and cortical layers with the axonal projections. We therefore refrained from laminar analyses of axonal length, and there was ambiguity in differentiation of axon in regions surrounding wS1. Thus, an important advance to be made in future studies is to align the neuronal tracing to better-defined brain areas and

cortical layers. In this study we traced clearly-labeled axonal processes, and it is likely that this provides a lower bound estimate of the total axonal length due to incomplete labeling or tracing. Here, particular concern must be raised because we typically were not able to follow callosal axons until their presumed targets in the contralateral hemisphere, but rather in most cases we lost the axon within the callosal fiber tract.

Functional studies suggest that neurons projecting to distinct downstream areas of wS1 signal different aspects of sensory information (Sato and Svoboda, 2010; Chen et al., 2013; Yamashita et al., 2013; Kwon et al., 2016; Yamashita and Petersen, 2016). Electrophysiological recordings from S2p and M1p neurons labeled similarly to the current study in mice adapted to head restraint but not otherwise trained in a task, suggest that M1p neurons are less excitable than S2p neurons; that M1p neurons have larger slow membrane potential fluctuations during quiet wakefulness; that M1p neurons have larger fast membrane potential fluctuations phase-locked to the whisking cycle; that M1p neurons show faster and larger excitation to a brief whisker deflection; and that M1p neurons only transiently signal onset of active touch, whereas S2p neurons show persistent activity during prolonged active touch bouts (Yamashita et al., 2013). In mice trained to lick a water reward spout in response to whisker deflection, S2p neurons show increased depolarization and action potential firing compared to naïve mice, whereas M1p neurons show reduced signaling (Yamashita and Petersen, 2016). Calcium imaging experiments also show enhanced decision-related signaling in S2p neurons in a whisker detection task (Kwon et al., 2016), which might be supported through reciprocal excitation of S1 and S2 (Kwon et al., 2016; Yang et al., 2016). Interestingly, decision-related signaling between wS1 and wS2 was also highlighted in a whisker-dependent texture discrimination task (Chen et al., 2013, 2015). There is therefore growing evidence for differential signaling in M1p and S2p neurons. Nonetheless within each group there remains substantial functional diversity, some of which may be accounted for by the additional projections that these neurons may have, as shown in this study. Perhaps the most important next experimental step for single-cell labeling studies is thus to link the brain-wide morphological investigation of individual long-range axonal projections with physiological measurement of activity of the same neurons. Indeed, juxtacellular electrophysiological recordings have been used in previous studies to monitor the spiking activity of a neuron followed by labeling with biocytin (Pinault, 1996), which can result in labeling of long-range projections of the recorded neuron (Igarashi et al., 2012; Varga et al., 2012). There are thus many further studies that need to be under-

taken before we will understand the structural and functional diversity of L2/3 projection neurons in wS1.

Chapter 3

Two-photon calcium imaging of layer 2/3 projection neurons in whisker barrel cortex during learning of a whisker and auditory detection task

Abstract

The execution of a goal-directed behavior requires the brain to process incoming sensory information from the environment in a context-, learning- and motivation-dependent manner in order to perform specific motor actions. Cortico-cortical communication in the context of goal-directed sensorimotor transformation has begun to be studied, but little is known about how signaling between interconnected cortical areas is modified by sensorimotor learning, as well as in response to changes in reward contingencies. Hence, in the second part of my thesis, I studied cortico-cortical dynamics in primary whisker somatosensory barrel cortex (S1) of mice during a combined whisker and auditory task. First, mice were trained to lick a water reward spout in response to detected auditory stimuli. After several days of training in the auditory detection task, whisker stimuli were introduced in randomly interleaved trials. Licking in response to whisker stimuli were also rewarded, and mice rapidly learned to lick on both whisker and auditory trials. Subsequently, when mice were experts in the detection of both sensory modalities, they underwent 2 days of extinction learning on whisker trials, in which licking in response to whisker stimulation was not rewarded. Finally, reward was reinstated in whisker trials. Using transgenic

mice expressing GCaMP6f combined with two-photon microscopy and retrograde labeling techniques, I chronically monitored the activity of excitatory layer 2/3 neurons in S1 projecting to whisker motor cortex (M1p) or secondary somatosensory cortex (S2p), while mice learned the behavioral switch task. The results demonstrated that both S2p and M1p neurons responded after whisker and auditory stimulation. However, whisker stimulus evoked response was stronger and faster than the auditory stimulus evoked response. S2p neurons exhibited higher responses compared to M1p neurons that correlated with task performance, with the largest difference observed in the late and very late phase (231 - 1000 ms) after whisker deflection. Those responses remained relatively stable across training sessions and under different reward conditions. Furthermore, both S2p and M1p neurons responded during spontaneous licking, but the S2p neuronal response was larger than M1p across sessions.

1.5 Introduction

Neuronal activity in the whisker primary somatosensory cortex (S1) is known to process tactile information from facial whiskers, but also to participate in goal-directed behaviors involving whisker stimulus detection (Sachidhanandam et al., 2013), object localization (O'Connor et al., 2010) and texture discrimination (Chen et al., 2013). Such information processed in wS1 is transferred to other brain areas through excitatory long-range projection neurons. Excitatory neurons in L2/3 of S1 send major projections in whisker primary motor cortex (M1) and secondary somatosensory cortex (S2) (Aronoff et al., 2010; Yamashita et al., 2018). Corticocortical neurons in S1 that project to M1 or S2 are largely non-overlapping subpopulations (Sato & Svoboda, 2010; Chen et al., 2013; Yamashita et al., 2013). Previous studies on S2-projecting (S2p) and M1-projecting (M1p) neurons in layer 2/3 of S1 have shown that these two neuronal populations have different responses to whisker stimulation during both anesthetized and awake conditions (Sato & Svoboda, 2010; Yamashita et al., 2013). In trained mice performing a single whisker detection task (Sachidhanandam et al., 2013), passive whisker deflection induced a long-lasting biphasic depolarization correlated with task performance in S2p neurons, but not in M1p neurons (Yamashita & Petersen, 2016). In addition, in spontaneous unrewarded licking of expert mice, only S2p neurons were excited and not M1p neurons. In a texture discrimination task (Chen et al., 2013; Chen et al., 2015), in which mice display fine rhythmic

whisking during the sampling period, a higher fraction of S2p than M1p neurons showed touch related responses, as well as S2p neurons exhibiting increased responses during texture discrimination. In contrast, in object localisation task, in which mice make large whisker sweeps during sampling period, M1p neurons showed increased response and ability to discriminate pole position compared to S2p neurons. Therefore, neurons in S1 send different types of information to S2 and M1 during sensorimotor processing.

Only a few studies have investigated these two pathways and what they encode, as well as how they are shaped during learning of a sensorimotor task (Chen et al., 2013; Chen et al., 2015; Yang et al., 2016; Yamashita and Petersen, 2016; Kwon et al., 2016). Moreover, no study has examined how different reward conditions influence those two streams of information. Therefore, with these questions in mind, we chronically monitored the activity of excitatory S2p and M1p layer 2/3 neurons in S1 using two-photon calcium imaging, while mice learned a whisker and auditory detection task executed under different reward conditions. Our results demonstrated that both whisker and auditory stimulation evoked responses in both S2p and M1p neurons, with whisker stimuli inducing stronger and faster responses compared to auditory stimuli across all sessions and reward conditions. Both whisker and auditory stimulation evoked stronger responses in S2p neurons correlated with task performance, which remained relatively stable across most training sessions and under different reward conditions. The largest differences in activity during task performance between S2p and M1p neurons were found during late and very late phase. Similarly, enhanced excitation in S2p neurons was observed during spontaneous licking across sessions and reward conditions.

1.6 Materials and Methods

3.2.1 Design and assembly of a two-photon microscope setup

The design of the two-photon laser-scanning microscope is based on the Movable Objective Microscope (MOM) system (adapted from Sutter Instruments), which places the objective on a x-y-z micro-manipulator, allowing precise movement control while the specimen remains stationary (**Figure 3.1.b, c**). Additionally, the entire microscope can be rotated around the x-axis, enabling imaging of non-horizontal surfaces and volumes. The backbone of the design is a movable, raised optical breadboard, providing a large area for attaching optical elements associated with the microscope, as well as enough

space for additional experimental equipment. The microscope is coupled to an 8-kHz resonant scanner for fast line scanning in the x-direction and a galvanometric scanner for slower scanning in the y-direction (**Figure 3.1.a**). A resonant scanner provides high imaging speed by continuously oscillating at its resonant frequency. The optical signals

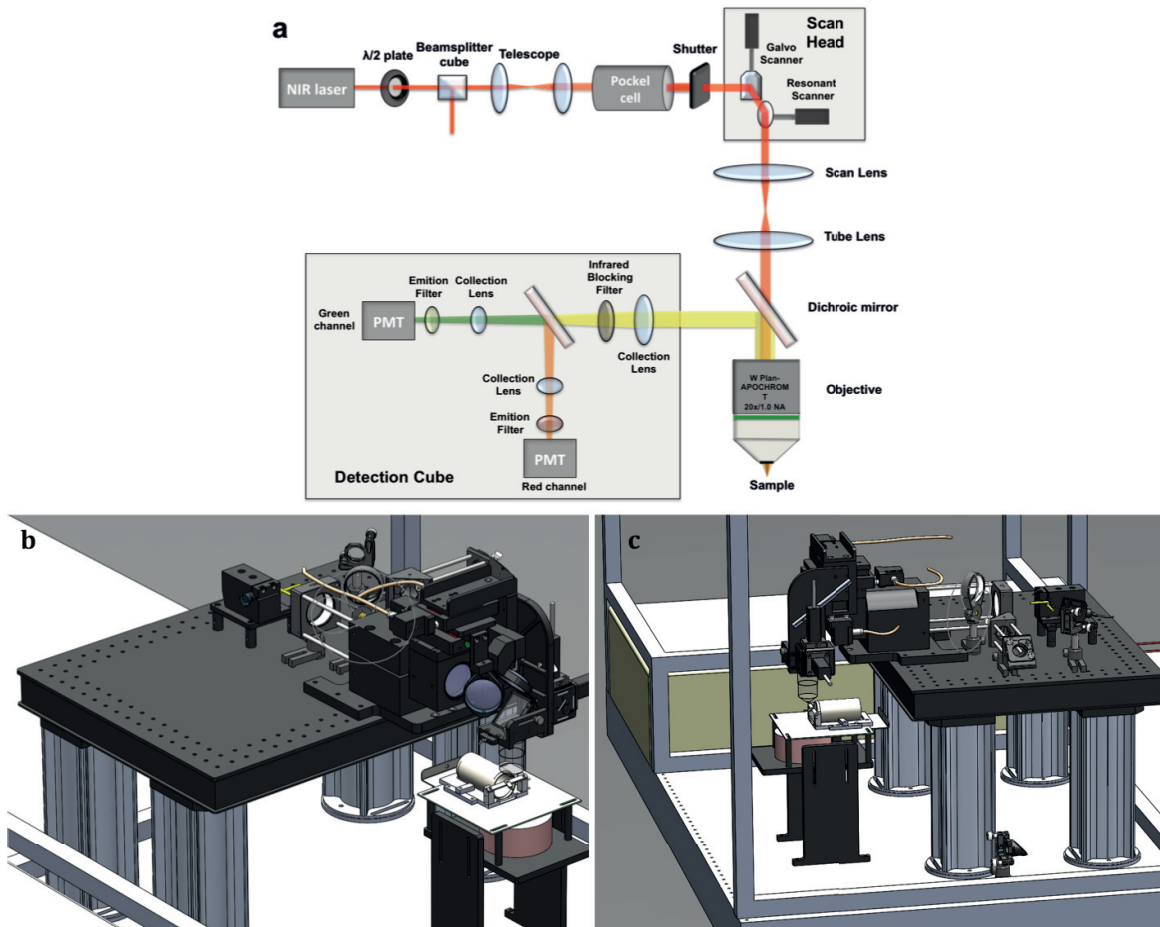


Figure 3.1: Two-photon microscope setup. a) Schematic diagram of the optical path of the two-photon microscope from the laser source to the scan head and the sample, and from the sample to the detection system. b), c) 3D-CAD design of the two-photon microscope setup including the mouse stage from two different views.

detected from the photomultiplier tubes (PMTs) are pre-amplified, then converted to digital signals, and finally fed into an FPGA module. At this point the PMT signals are integrated into a pixel array according to the oscillating motion of the resonant scanner (sig-

nal of the scanner's position corresponding to a pixel). The frame rate at which image sequences are acquired depends on the specified number of lines per frame. Thus, in my setup, a frame of 512 lines is acquired at ~30 Hz frame rate.

The near infrared light source of the two-photon microscope was provided by a Ti:Sapphire laser system that generates ultrashort pulses (<100 fs) delivered at a repetition rate of 80 MHz at a wavelength output tuned from 690 nm to 1040 nm (MaiTai DeepSee, Spectra-Physics). The intensity of the laser beam can be controlled by adjusting its polarization angle using a half-wave plate, followed by a polarizing beamsplitter cube that is used to separate the polarized light into a vertical and horizontal component (**Figure 3.1.a**). Subsequently, a Pockel's cell (model 302RM, Conoptics) is used to control the laser beam intensity, followed by a two-lens telescope that is used to expand beam size (3x beam expansion, lens 1: $f_1 = 100$ mm; lens 2: $f_2 = 300$ mm, Thorlabs). A mechanical shutter (SH05 beam shutter, SC10 shutter controller, Thorlabs) placed just before the beam enters the scan head is used to block the beam in the absence of imaging. The beam is then deflected by the scan mirrors, using an 8 kHz resonant scanner (aperture 6x4 mm, scanning angle 26 degrees, CRS Series, Cambridge Technology, GSI) for fast scanning in the x-axis coupled with a galvanometric mirror (aperture: 8x12mm, M-Series model 6210, Cambridge Technology, GSI) for line-by-line scanning in the y-axis. The laser then travels through the scan lens and tube lens in the optical path, consisting a second two-lens telescope that further expands the beam (2.6x beam expansion, lens 1: $f_{\text{scan}} = 75$ mm; lens 2: $f_{\text{tube}} = 200$ mm, Thorlabs) so as to fill the back aperture of the objective. After passing through a dichroic beamsplitter (F76-705, AHF Analysentechnik), the beam is focused by an objective of 20x magnification (Zeiss Objective W Plan-Apochromat 20x/1.0 DIC D=0.17) onto the specimen. The emitted fluorescence signals are then passing through an infrared blocker (ET750sp-2p (edge 750), Chroma) that transmits photons in the range of 393 - 749 nm, and blocks photons in the range of 770 - 1100 nm. The fluorescence signals are then detected with two PMTs (GaAsP photomultiplier tubes Hamamatsu Photonics). In order to achieve three-colour fluorescence detection (green, red, and far red), I used two different filter cubes: one which is coupled to emission filters for green and red wavelengths (F37-584 (green 510/84), F39-608 (red 607/70), F38-562 (beamsplitter, edge 562) AHF Analysentechnik), and one which is coupled to emission filters for red and far red wavelengths (F47-700 (far red 700/75), F39-610 (red 609/57), F38-649 (beamsplitter, edge 649) AHF

Analysentechnik). The PMT signals are subsequently pre-amplified using a variable gain high-speed current amplifier (DHPCA-100; Femto, Berlin, Germany), digitized using an analog-to-digital converter (NI-5732, National Instruments) and transmitted to an FPGA module (NI PXI-7813R, National instruments), which is integrated into a chassis (NI PXIe-1073, National instruments). Additionally, the FPGA module generates a step-wise signal to control the motion of y-scanner, after receiving a synchronisation signal (line-clock signal) from the resonant scanner 's control board (CRS 8K driver, model 6SC08KA012-02Y, Cambridge Technology). Regarding the zooming function, an analog output signal is generated that controls the oscillating amplitude of the resonant scanner using a data acquisition (DAQ) board (NI PXI-6341, National instruments). The same DAQ board generates the signal that controls the intensity of the laser beam through the Pockel's cell. The two-photon microscope is controlled through Matlab with ScanImage 5 software (Vidrio Technologies; Pologruto et al., 2003).

3.2.2 Mouse head-post implantation

All experiments were carried out with 6-10 week old female and male Rasgrf2-dCre mice (Harris et al., 2014; Madisen et al., 2015) crossed with TIGRE2.0 Cre-dependent GCaMP6f reporter mice (Ai148) (Daigle et al., 2018) in accordance with protocols approved by the Swiss Federal Veterinary Office.

In order to achieve chronic and stable recordings, mice were implanted with a small light-weight metal head-post on their skull. Mice were deeply anesthetized with isoflurane gas anesthesia (3-4% for induction) and then placed on the stereotaxic apparatus using a nose-clamp. During surgery, the level of isoflurane concentration was maintained at 1.5%, temperature was controlled and held at 37°C with a heating pad (FHC), and eyes were protected with an eye gel (Viscotears, Alcon). To prevent pain or inflammation after the surgery, mice were injected with Carprofen (0.3 ml at 0.5 mg/ml, i.p.) (Rimadyl, Pfizer) and a mix of lidocaine (2% diluted 1:10) and bupivacaine (0.5% diluted 1:2) subcutaneously on the incision site at the beginning of the surgery. The skin was cut and the skull was exposed. The membrane of periosteum covering the skull, was gently removed using a scalpel, and then skull was cleansed with Betadine. Immediately after the bone was dried, it was covered with cyanoacrylate glue (Loctite, Henkel) and a small metal post was fixed onto the right hemisphere of the skull. Finally, dental cement (Paladur) was added to reinforce the attachment of the head-post and create a chamber around the region of interest. A silicone elastomer (Kwik-Cast, WPI) was ap-

plied in the chamber to protect the exposed skull. At the end of the surgery, in order to avoid post-operative pain, Algifor (2.5 ml in 250 ml of water) was added into the water bottle for 3 days.

3.2.3 Intrinsic signal optical imaging

In order to target the experiments to the region of interest, the C2 barrel column in primary whisker somatosensory cortex (wS1), I used intrinsic signal optical imaging (Grinvald et al., 1986). It is a minimally invasive technique, which is based on recordings of intrinsic optical signals (IOS) from the surface of the cortex that are induced by sensory stimulation under light anesthesia. The IOS imaging was performed immediately after implantation, while maintaining the level of anesthesia at 1% and temperature at 37°C. All whiskers but C2 were trimmed, and the mouse was transferred on a holder to fix the head using the implanted metal head-post. The mouse head was placed under a CMOS camera coupled to a stereomicroscope (Leica MZ9.5) with a magnification of 3.2x. A reference image of the surface vasculature was first acquired under green illumination (525 nm, Thorlabs LED) (**Figure 3.2.a**). The C2 whisker was then inserted in a glass capillary attached to a piezo actuator (PICMA, PI Ceramic) and deflected for 4 seconds in the antero-posterior direction at a repetition frequency of 10 Hz, while brain surface was under

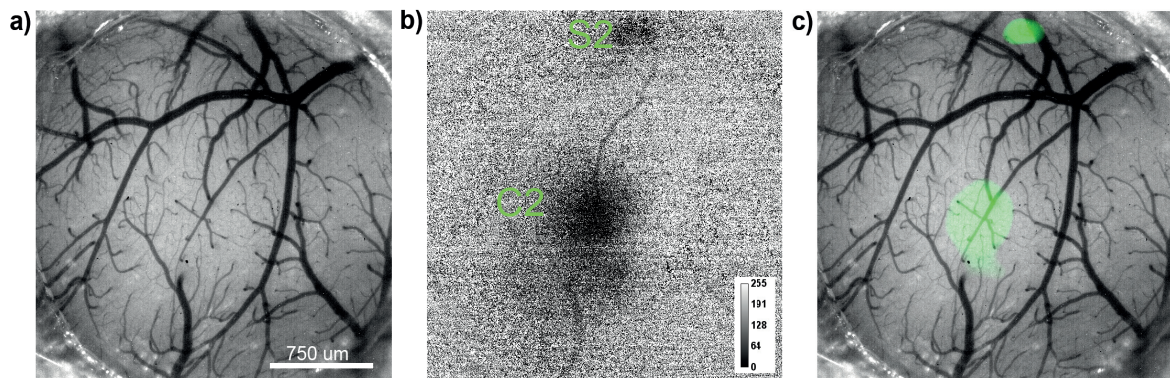


Figure 3.2: Intrinsic signal optical imaging. a) Anatomy image of the surface vasculature. b) Functional image of the intrinsic signal of the C2 barrel in wS1 as well as S2 area after C2 whisker stimulation. c) Overlay of functional image on the anatomy image to map C2 barrel

constant red illumination (630 nm, Thorlabs LED). Reflected light was collected through the stereomicroscope and recorded by the CMOS camera (**Figure 3.2.b**). This process

was repeated several times, while trials without whisker stimulation were interleaved. The relative change in light reflectance was calculated by subtracting the mean baseline reflectance (R_b) from the mean reflectance measured during whisker stimulation (R_s) and dividing this value by the mean baseline reflectance: $(R_s - R_b) / R_b$. Image acquisition and processing was done with custom routines written in Matlab. Finally, the functional image of the intrinsic signal was overlaid on the anatomical image of the surface vasculature to map the C2 barrel column and wS2 areas (**Figure 3.2.c**).

3.2.4 Craniotomy and chronic cranial window implantation

Two-photon laser scanning microscopy in combination with genetically encoded calcium indicators (GECIs) provide a valuable tool for monitoring neuronal activity over long time. A chronic cranial window preparation over the region of interest in the mouse cortex is of key importance to obtain optical access for long-term imaging (Holtmaat et al., 2009; Holtmann et al., 2012). There have been proposed several protocols, to handle different needs, such as the removable cranial windows that have been used to reduce dura re-growth (Goldey et al., 2014), or the cranial window with access port that has a circular hole off-center into the coverglass (Roome and Kuhn, 2014), which enables cellular manipulation, drug application and electrophysiological recordings. Furthermore, there is the cranial window that has a microprism attached under the coverglass (Andermann et al., 2013), which enables deep-layer imaging in awake mice, or the cranial window that has a microfluidic pump (Takehara et al., 2014), which provides long-term monitoring of neurons and the delivery of chemicals or drugs directly into the brain. Finally, there is a new version of cranial window preparation made of a soft, flexible, transparent and penetrable silicon-based material, which allows not only long-term imaging but also the penetration of microelectrodes for electrophysiology and injections of viruses, drugs and/or other chemicals (Heo et al., 2016).

In chronic cranial window implantation (**Figure 3.3.a**), a small circular piece of bone of ~3.5 mm in diameter is removed (craniotomy), and then replaced by a triple round coverglass, while dura remains intact. The craniotomy is centered in C2 area and includes S2 that I have previously mapped with IOS. Before the surgical procedure, I prepare the triple cranial window consisting of a 5 mm coverslip cured to two 3 mm coverslips (Warner Instruments #1) using UV-curing adhesive (Thorlabs, NOA61), giving a total thickness of ~0.45 mm (**Figure 3.3.c**). The coverglass is placed in the craniotomy and then permanently sealed with UV-curing adhesive (Thorlabs, NOA68) and dental cement on top to provide

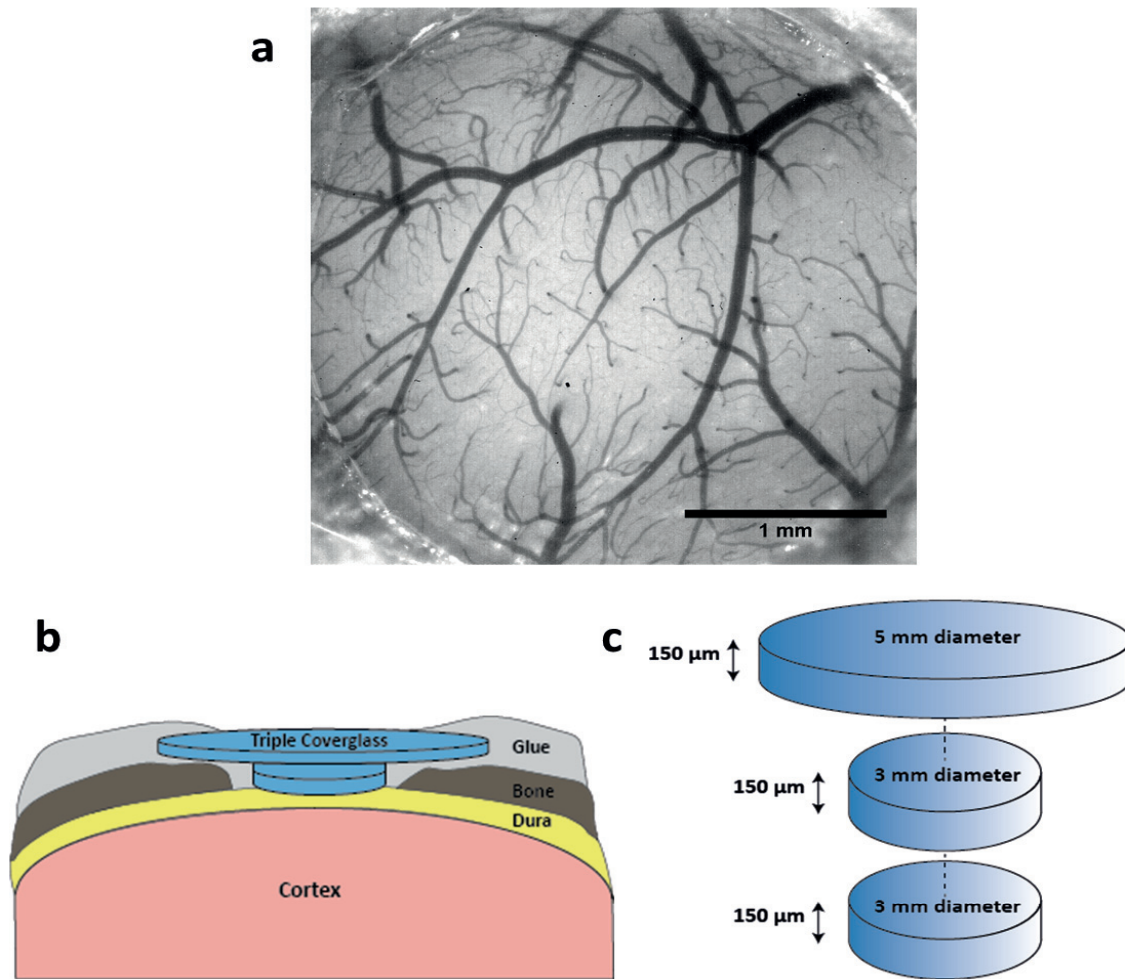


Figure 3.3: Chronic cranial window implantation for awake imaging in mice. a) Image of a typical chronic cranial window centered in wS1, one week after implantation. b) Schematic diagram of chronic cranial window preparation for in-vivo imaging. Approximately a ~3.5 mm circular craniotomy is performed and a triple round coverslip is secured in place using UV-curing adhesive (Thorlabs, NOA68) and dental cement on top, and then mice are allowed to recover for at least 7 days. c) Schematic geometry of the triple round coverslip. A 5 mm coverslip is cured to two 3 mm coverslips (Warner #1; total thickness: 0.45 mm) using UV-curing adhesive (Thorlabs, NOA61).

stability to the window over the long-term (**Figure 3.3.b**). Mice are allowed to recover for a week after the implantation. The window covers a diameter of about 3 mm, which, if it remains stable and clear for the first week, enables imaging of the same neuronal population over months (**Figure 3.3.a**). This method provides the means to chronically monitor with two-photon microscopy the same population of neurons in a mouse and visualize

changes in individual neurons allowing us to study cortical stability and plasticity (Helmchen and Denk, 2005; Svoboda and Yasuda, 2006; Huber et al., 2012; Margolis et al., 2012; Lütcke et al., 2013, Chen et al., 2015, Mayrhofer et al., 2015).

3.2.5 Expression of calcium indicator and retrograde labelling of L2/3 projection neurons in wS1

Cell-type-specific genetic tools coupled with the development of improved genetically encoded calcium indicators constitute a powerful tool for the study of brain function via selective expression of calcium probes in different cell types. In this study, I used a L2/3-specific Cre-driver mouse line (Rasgrf2-dCre) crossed with a TIGRE2.0 reporter mouse line expressing the GCaMP6f calcium indicator (Ai148-Rasgrf2Cre) (Daigle et al., 2018) (**Figure 3.4**). dCre recombinase activity was induced by intraperitoneal injection of trime-

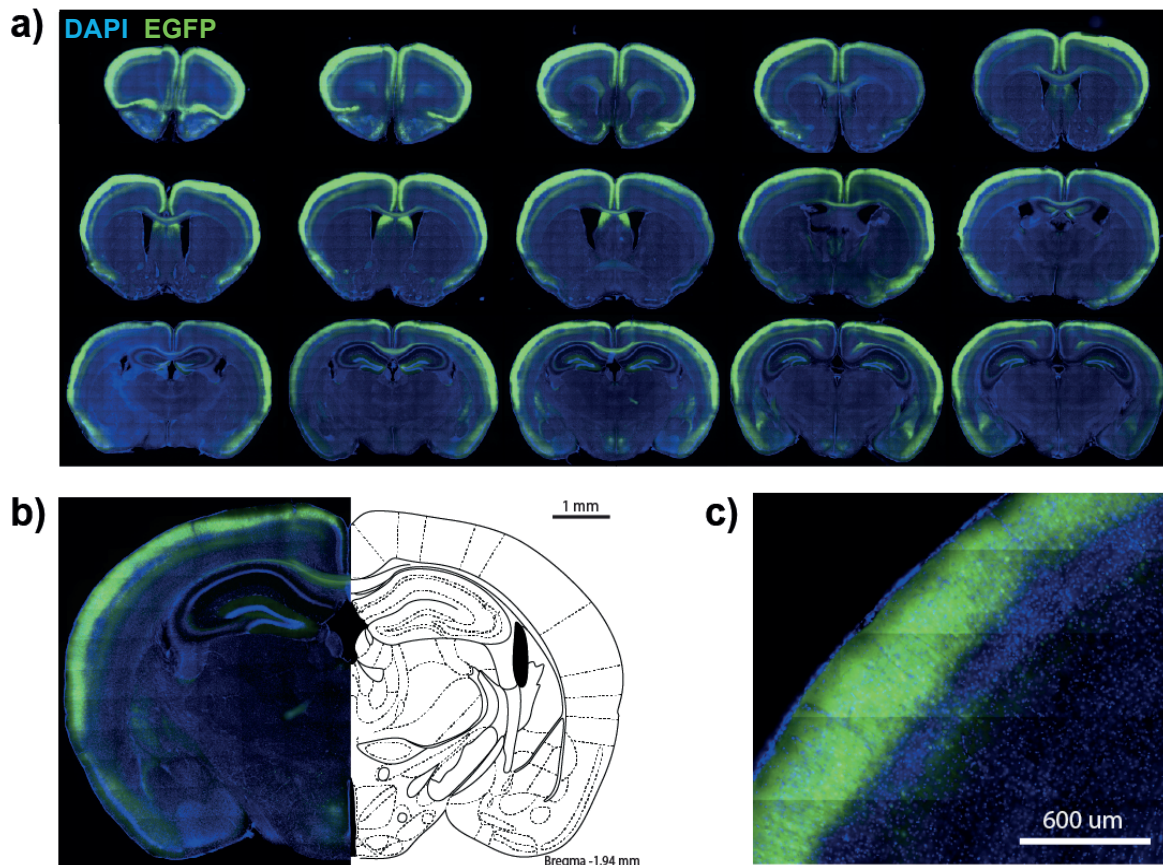


Figure 3.4: L2/3 neurons selectively expressed GaMP6f in Rasgrf2-dCre mice crossed with TIGRE2.0 Cre-dependent GCaMP6f reporter mice. a) Ai148-Rasgrf2 mice demonstrate layer specific expression of GCaMP6f across cortex. b) Example brain section around the centre of whisker primary somatosensory cortex. c) Zoom-in a cortical region.

thoprim (TMP) (0.25 mg/g body weight) for 3 consecutive days.

During cranial window preparation, after craniotomy was completed, stereotaxic CTB tracer injections were performed on Ai148 × Rasgrf2-dCre mice. CTB conjugated with Alexa-Fluor 594 (Molecular Probes, Invitrogen; 100 nl, 0.5 %, wt/vol) was injected into S2 using a glass pipette (tip diameter=27-30 mm) (**Figure 3.5.a**). Injection volume was 50 nl at ~300 µm and 50 nl at 500 µm below the pial surface, giving a total volume of 100 nl. S2 injection site was identified using intrinsic optical imaging as previously described. A glass coverslip was then used to seal the craniotomy. A second craniotomy of ~1 mm in diameter, was then opened over M1 (1 mm anterior, 1 mm lateral to Bregma) and CTB conjugated with Alexa-Fluor 647 (Molecular Probes, Invitrogen; 200

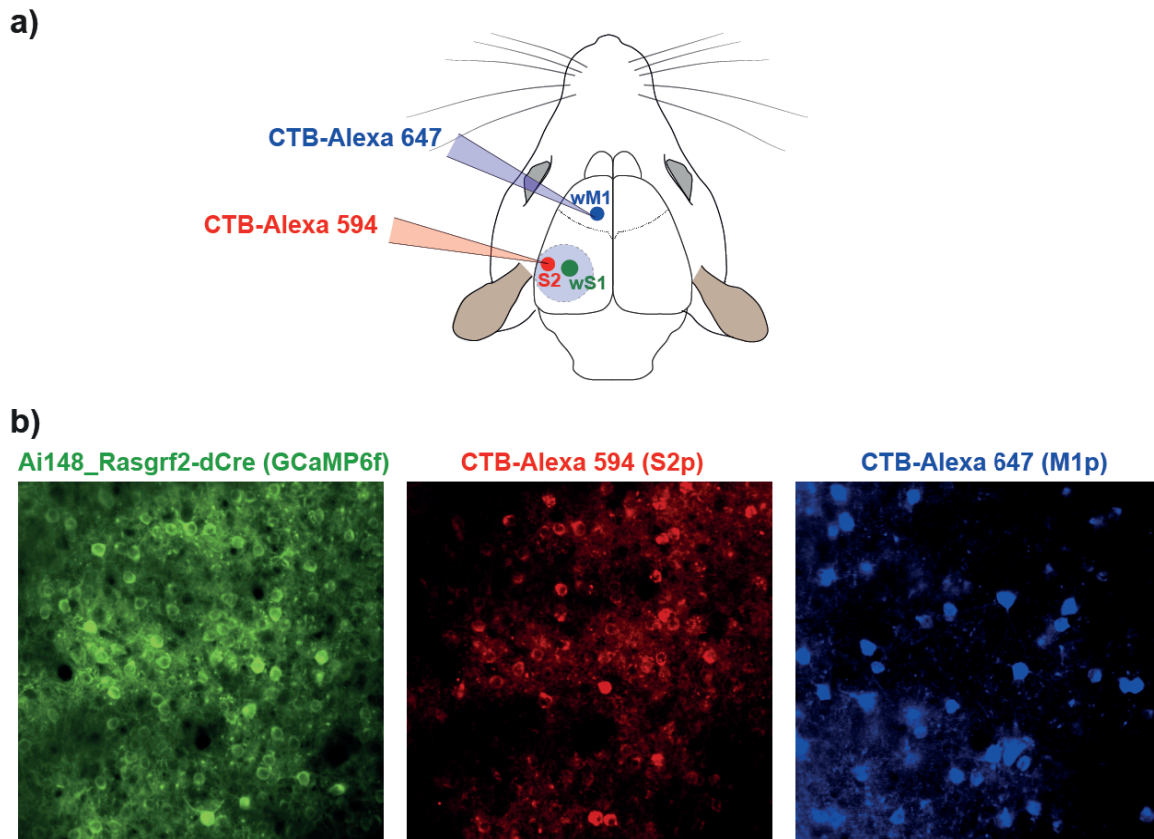


Figure 3.5: a) Retrograde labelling of S2p and M1p neurons in wS1. Schematic of mouse brain showing retrograde tracers and injection areas. CTB conjugated with Alexa-594 (red, 0.5%) and Alexa-647 (blue, 0.5%) was injected into S2 (100 nl) and M1 (200 nl) of the left hemisphere. b) CTB-labeled layer 2/3 neurons in S1 at the subpial depth of 200 µm imaged in-vivo with a two-photon microscope. Neurons expressing GCaMP6f in green, S2p neurons in red expressing CTB-Alexa 594 and M1p neurons in blue expressing CTB-Alexa 647.

nl, 0.25%, wt/vol) was injected (100 nl at ~300 μ m and 100 nl at 500 μ m below the pial surface, total volume of 200 nl) (**Figure 3.5.a**). In some mice, CTB injections were inverted, in particular, CTB Alexa-Fluor 647 was injected in S2 and CTB Alexa-Fluor 594 was injected in M1. Imaging of CTB labeled neurons expressing GCaMP6f was performed at earliest eight days after injections and cranial window implantation using a two-photon microscope (**Figure 3.5.b**).

3.2.6 Whisker and auditory detection task

I trained 19 mice to perform a head-fixed go/no-go whisker and auditory detection task. Approximately one week after cranial window implantation and CTB injections, mice underwent water-deprivation. Behavior was reported by licking of a water spout attached to a piezo sensor that activates the delivery of a water drop (4-5 μ l) through a pneumatic valve (**Figure 3.6.a**). Mice were initially habituated to head-restraint on the recording set-up and exposed to 'free-licking' for 1-2 sessions (pre-training) (**Figure 3.6.b**). In 'free-licking' sessions, mice receive water drops at random time points, while imaging L2/3 neurons in wS1 to identify the center of C2 barrel and define the imaging field of view using a two-photon microscope (**Figure 3.6.a**). At the beginning of training, mice were taught to lick the water spout for reward in response to detected auditory stimuli (**Figure 3.6.b**). After several days of training in the auditory detection task, and when mice had reached good performance, whisker stimuli were introduced in randomly interleaved trials. Licking in response to whisker stimuli were also rewarded, and mice rapidly learned to lick on both whisker and auditory trials. Subsequently, when mice had reached high and stable performance in the detection of both sensory modalities, they were exposed to extinction learning on whisker trials for two days, in which licking after whisker stimulation was not rewarded, thus mice had to learn to withhold licking activity. After the extinction phase on whisker trials, water reward was reinstated for a number of sessions, until mice reached again high and stable performance for both whisker and auditory trials. Finally, mice were subjected to a whisker particle control experiment and psychophysical measurements of whisker stimulus intensity during execution of the task (post-training) (**Figure 3.6.b**). In the whisker particle control session, after ~100 trials from the beginning of training, the metal particle attached to the whisker was removed, therefore, there was no whisker sensory input to the mouse. The mouse performed under this condition for ~100 trials, and then the metal particle was again attached to the whisker, and the mouse continued the training until it stopped licking for a reward. Regarding the psychophysical

measurements of whisker stimulus intensity, mice were trained for 2 to 3 sessions in three different whisker stimulus intensities: 1 ms (28 mT), 0.08 ms (14 mT), and 0.04 ms (8 mT).

For auditory stimulation, I used a 10 kHz sound of 10 ms duration. For whisker stimulation, a small metal particle was attached to the whisker, and a magnetic coil was placed under the mouse centered at the site of the right C2 whisker (**Figure 3.6.a**). The coil was producing magnetic pulses of 1 ms that were vertically deflecting the whisker. Trials with either whisker or auditory stimulation, as well as trials without stimulation (catch trials or no-stim trials) were interleaved throughout training and presented at random inter-trial intervals ranging from 11-14 s. Catch trials were presented with 30-40% probability of all trials. A trial consisted of a 3 s pre-stimulus period (quiet time) followed by stimulus presentation (**Figure 3.7**). If mice licked within the 3 s quiet window, the trial was aborted and a 5-8 s time out period was imposed to the mouse. The reward time window was 1 s after stimulation. A white noise sound was used throughout training to mask any possible sounds that are not associated to the task. Control and data acquisition of behavior experiments were performed using a custom-written LabVIEW software (National Instruments).

There are eight trial types across all different training phases (**Figure 3.7**, **Figure 3.8**). When licking occurred immediately after auditory stimulation (within 1 s reward window), water was delivered to the mouse and the trial characterized as 'auditory hit' (AHit). When mice did not lick after auditory stimulation the trial scored as 'auditory miss' (AMiss). In sessions where whisker stimulation was rewarded (whisker detection), licking after whisker deflection was defined as 'whisker hit' (WHit) and no licking as 'whisker miss' (WMiss). In sessions where whisker stimulation was not rewarded (whisker extinction), licking after whisker deflection was defined as 'whisker false alarm' (WFL), and when mice withheld licking the trial was described as 'whisker correct rejection' (WCR). During catch trials, if there was no licking, the trial was characterized as 'correct rejection' (CR), and if there was licking, the trial was scored as 'false alarm' (FA).

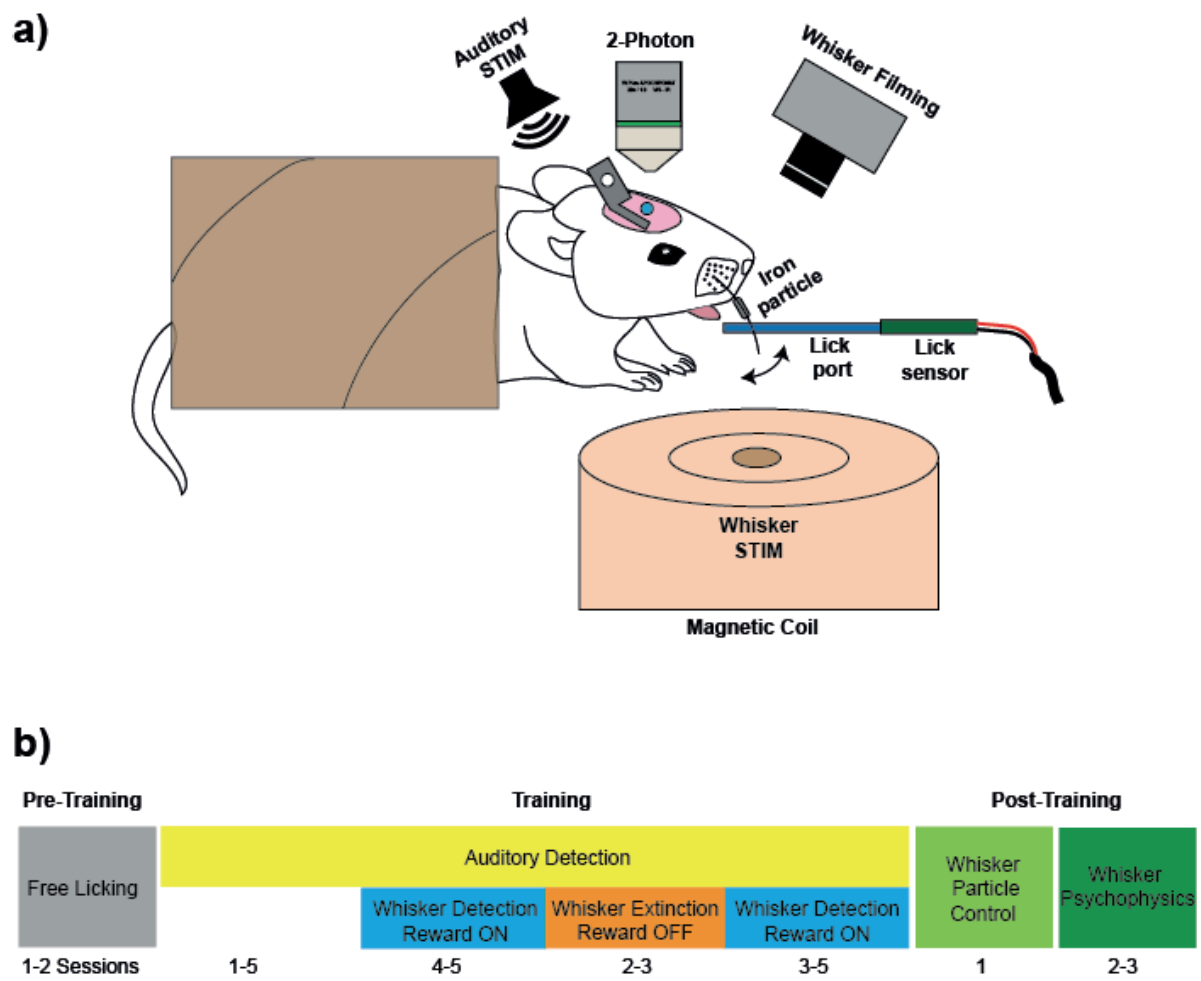


Figure 3.6: a) Schematic of experimental setup. b) Timeline of experiment's training sessions

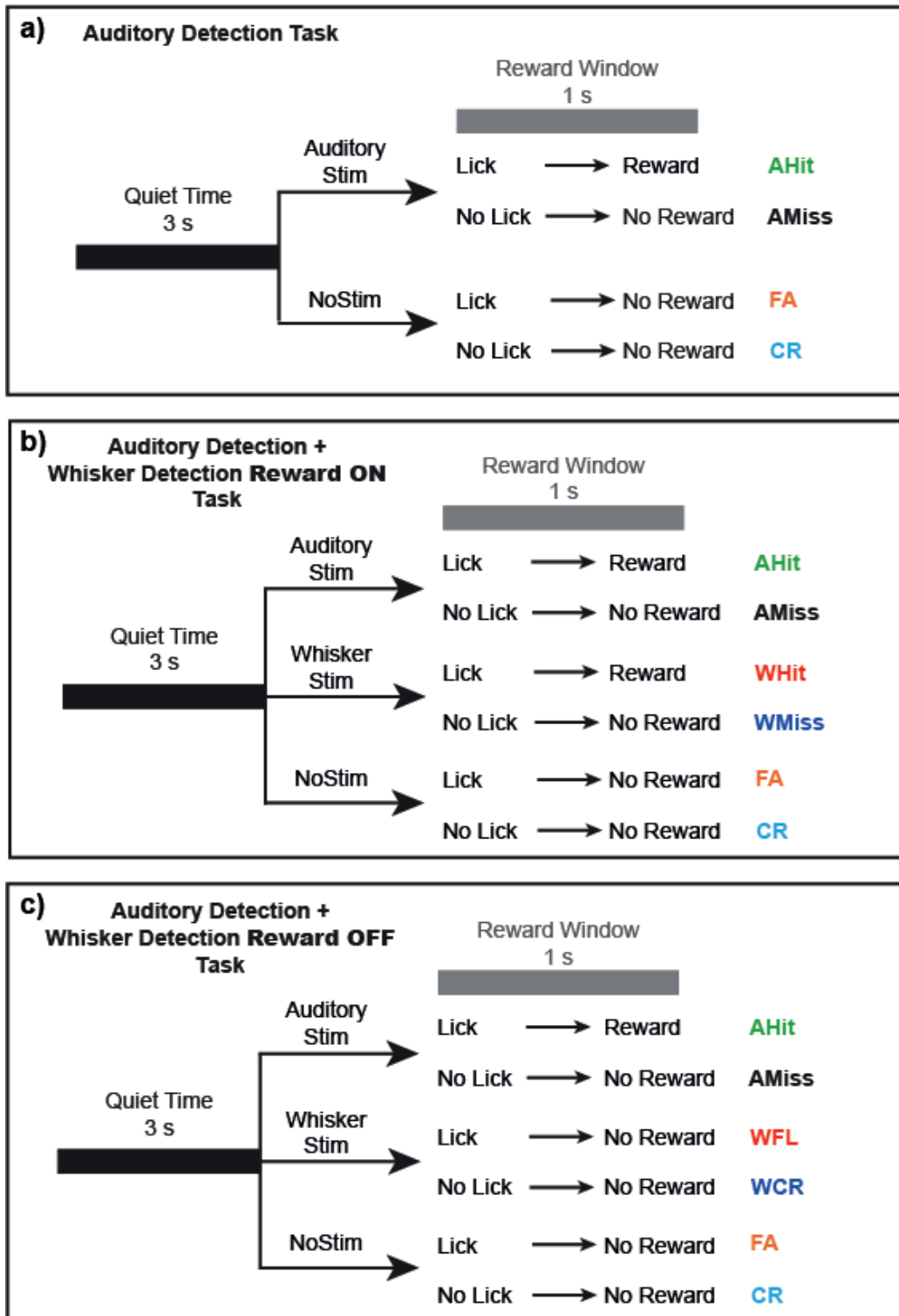


Figure 3.7: Whisker and auditory detection task. Schematic of trial structure for the 3 different conditions of the training (AHit: auditory hit, AMiss: auditory miss, WHit: whisker hit, WMiss: whisker miss, WFL: whisker false lick, WCR: whisker correct rejection, FA: false alarm, CR: correct rejection)

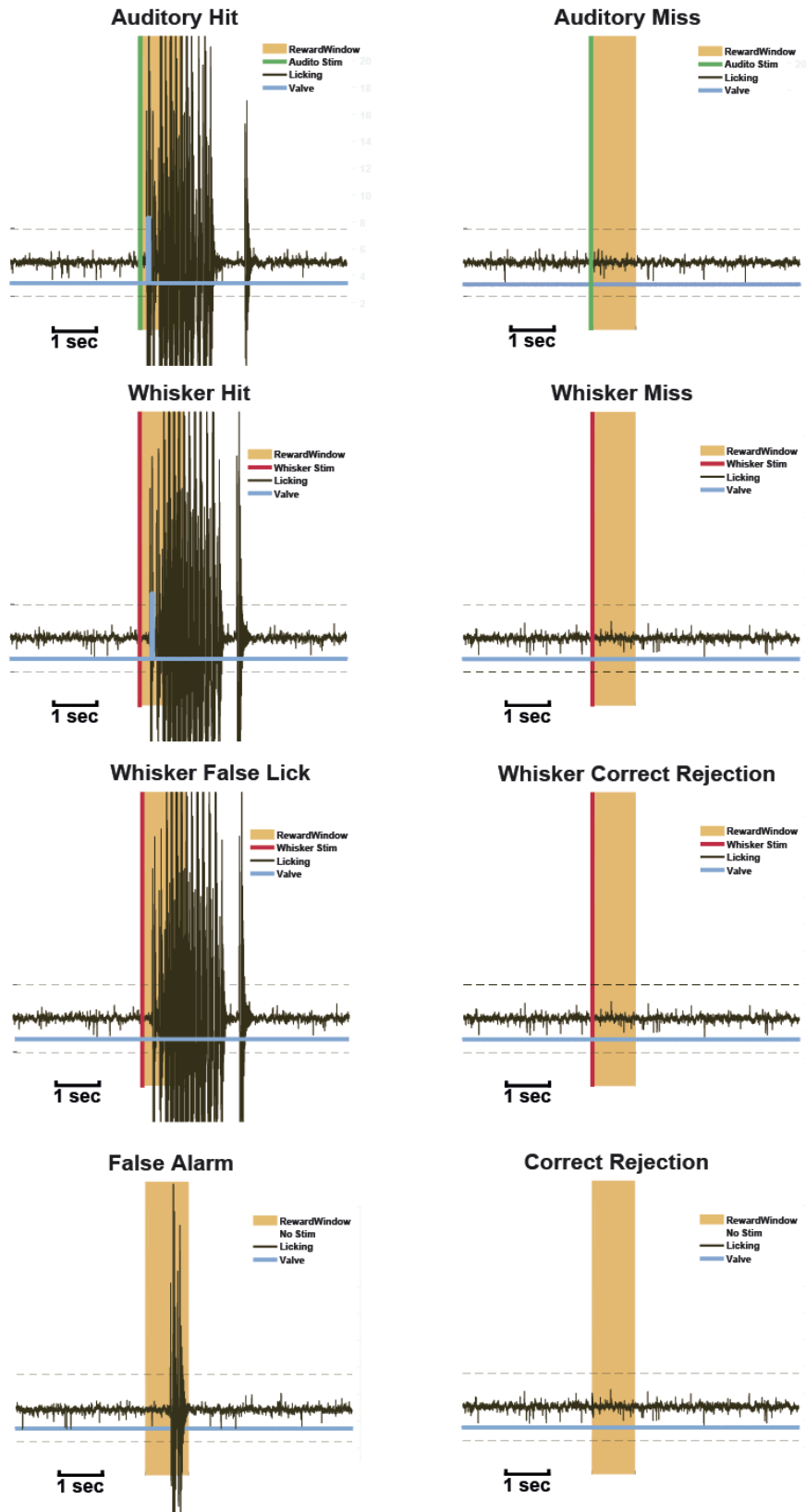


Figure 3.8: Whisker and auditory detection task. Examples of the different trial types

3.2.7 Two-photon calcium imaging

Chronic imaging started at earliest eight days after CTB injections and cranial window implantation using a custom-built two-photon laser-scanning microscope (see materials and methods 3.2.1). Images were acquired at a frequency of 30 Hz with 512x512 pixel resolution. Anatomical imaging was performed during the 'free-licking' sessions to identify the center of C2 barrel column according to the functional (IOS) and anatomical (blood vessel pattern) superimposed image, which was acquired with the intrinsic imaging method. A z-stack of about 250 μm from the surface with 5-10 μm step was acquired. The imaging field-of-view (FOV) was chosen on the basis of the location of S2p and M1p neurons at the center of C2 barrel column and was the same across all training sessions. An average image of the selected FOV was created before the start of the first training session, which was used as the master reference image to find the same imaging location at every session. During an imaging session data was acquired continuously (gap-free). The behavior control program provided three analog input signals 0-5 V (Start, Stop, Next) to ScanImage in order to trigger the start of image acquisition, the next file opening to save trial data and the end of acquisition.

3.2.8 Calcium imaging analysis

Calcium imaging data analysis was performed using Matlab (MathWorks). Anatomical fluorescence data acquired from all channels (EGFP, Alexa-594, Alexa-647), before the start of the first training session, was imported into Matlab for processing. Movies were corrected for movement artifacts (2-D rigid translation) (Guizar-Sicairos et al., 2008), and average images for each channel were created. A 3-channel stack image containing red fluorescent Alexa-594 (S2p neurons in red channel), far red Alexa-647 (M1p neurons in blue channel) and EGFP (all neurons expressing GCaMP6f in green channel) (**Figure 3.5.b**) was formed, which was used as a master reference image.

Functional imaging data acquired from the green channel (GCaMP6f) was imported into MATLAB for processing. The first step of processing was the subtraction of background, which is the minimum fluorescence value across the entire video for each trial. Motion correction was performed using a Matlab routine, which performs subpixel image registration by cross-correlation (2-D rigid translation) (Guizar-Sicairos et al., 2008). Regions of interest (ROIs) corresponding to individual neurons were manually selected from

the master reference image of the first imaging session using ImageJ (ImageJ, National Institutes of Health, USA). For each session, a reference mean image over a number of frames (~2000-3000 frames) was created. Reference images of each session were then registered (affine transformation consisting of translation, rotation, scale, and shear) to the master reference image of the first session, and the calculated transformations were stored. The selected ROIs were then registered on the reference image of each session by applying the calculated transformations. Finally, pixel values within each ROI were averaged and extracted for each frame across all imaging sessions. Calcium signals were expressed as relative change in fluorescence $\Delta F/F = (F - F_0)/F_0$. F_0 was calculated as the mean value of 60 frames before the trial start (the stimulus or no-stimulus event).

1.7 Results

3.3.1 Whisker and auditory detection task

I trained 19 mice to perform a head-fixed go/no-go whisker and auditory detection task, in which mice underwent different reward conditions and stimulus presentations. In this task, at first mice were trained only in auditory stimulus detection (**Figure 3.6.b, Figure 3.7.a, and Figure 3.9, Figure 3.10.a**). Water-restricted mice learned to detect auditory stimuli by reporting sensory perception through licking a reward spout to obtain water. Catch trials, in which no stimulus was applied, were randomly interleaved throughout training. Trials occurred at random inter-trial intervals ranging from 11-14 s. Mice needed from 1 to 5 sessions (**Figure 3.6.b, Figure 3.10.a**) to reach good performance (AHit rate = 0.66, FA rate=0.21, day 1, learning curve of mouse AV208) (**Figure 3.9**), (AHit rate = 0.76 ± 0.10 , FA rate = 0.19 ± 0.06 , $n=19$, mean \pm SD, day before whisker detection starts, average learning curve for whisker day 1 alignment) (**Figure 3.10.b**). Auditory detection performance remained high and stable throughout training for all mice (**Figure 3.10.a**). After mice reached good performance on the auditory detection, whisker stimuli were introduced in randomly interleaved trials (**Figure 3.7.b, Figure 3.9, Figure 3.10.b**). Mice rapidly learned the whisker detection task, in particular, 16 out of 19 mice developed good whisker performance within the first session, two mice within the second session, one mouse within the third session (WHit rate = 0.69, AHit = 0.89, FA rate = 0.21, day 2, learning curve of mouse AV208) (**Figure 3.9**), (WHit rate = 0.70 ± 0.20 , AHit rate = 0.81 ± 0.04 , FA rate = 0.15 ± 0.07 , $n=19$, first day of whisker detection, average learning

curve for whisker day 1 alignment) (**Figure 3.10.b**). Most mice ($n=17$) were trained under these conditions for 4 to 5 training sessions (**Figure 3.6.b**). Only two mice had unstable performance during this phase and needed more training time (9 sessions). As soon as mice showed high performance for a minimum of 4 sessions on both whisker and auditory trials (WHit rate = 0.81, AHit = 0.82, FA rate = 0.15, day 6, learning curve of mouse AV208) (**Figure 3.9**), (WHit rate = 0.80 ± 0.01 , AHit rate = 0.81 ± 0.01 , FA rate = 0.11 ± 0.05 , $n=19$, day before whisker extinction, average learning curve for extinction day 1 alignment) (**Figure 3.10.c**), they were exposed to extinction learning on whisker trials for two days (**Figure 3.7.c, Figure 3.9, Figure 3.10.c**). In this phase of training, if mice licked after whisker stimulation they did not receive a water reward. Consequently, after a number of trials (variable across mice) in which mice were not rewarded upon whisker stimulation, gradually they learned to withhold licking in response to whisker stimulation. At the first extinction session, licking performance on whisker trials dropped by half (WFL rate = 0.45, AHit = 0.80, FA rate = 0.04, day 7, learning curve of mouse AV208) (**Figure 3.9**), (WFL rate = 0.46 ± 0.06 , AHit rate = 0.81 ± 0.02 , FA rate = 0.06 ± 0.03 , $n=19$, first day of whisker extinction, average learning curve for extinction day 1 alignment) (**Figure 3.10.c**), and the second day had fallen to ~25 % (WFL rate = 0.21, AHit = 0.80, FA rate = 0.04, day 8, learning curve of mouse AV208) (**Figure 3.9**), (WFL rate = 0.22 ± 0.07 , AHit rate = 0.81 ± 0.01 , FA rate = 0.05 ± 0.04 , $n=19$, last day of whisker extinction, average learning curve for extinction day 1 alignment) (**Figure 3.10.c**). Almost all mice needed two sessions to learn to withhold licking in response to whisker stimulation until they displayed low performance on whisker extinction, except one mouse that needed three sessions. After whisker extinction phase, water reward was reinstated for 3 to 6 sessions (**Figure 3.6.b, Figure 3.7.b, Figure 3.9, Figure 3.10.c**), until mice reached again high and stable performance for both whisker and auditory detection (WHit rate = 0.85, AHit = 0.87, FA rate = 0.15, day 13, learning curve of mouse AV208) (**Figure 3.9**), (WHit rate = 0.81 ± 0.03 , AHit rate = 0.82 ± 0.05 , FA rate = 0.09 ± 0.06 , $n=19$, day 7 after whisker extinction, average learning curve for extinction day 1 alignment) (**Figure 3.10.c**). Some mice restored high performance very quickly, even within the first session after extinction, however, there were some that needed more training sessions.

At the last phase (post-training), some mice were subjected to a whisker particle control experiment and psychophysical measurements of whisker stimulus intensity during execution of the task (**Figure 3.6.b, Figure 3.11**). In whisker particle control session (**Figure 3.11.a**), when the metal particle was removed from the whisker, the mice almost

stopped performing on whisker stimulus trials (WHit rate = 0.04 ± 0.05 , AHit rate = 0.98 ± 0.04 , FA rate = 0.06 ± 0.05 , $n=11$, particle OFF) (**Figure 3.11.a**), which means that there was no sensory input or other cue triggering licking for reward. When the metal particle was reattached on the whisker, high performance was reinstated (WHit rate = 0.81 ± 0.01 , AHit rate = 0.75 ± 0.02 , FA rate = 0.04 ± 0.02 , $n=11$, particle ON) (**Figure 3.11.a**). Performance on auditory trials was high and stable throughout session. Regarding the psychophysical measurements of whisker stimulus intensity, mice were trained for 2 to 3 sessions in three different whisker stimulus intensities, 1 ms (28 mT), 0.08 ms (14 mT), and 0.04 ms (8 mT). Measurements from all 2-3 sessions were grouped together, and psychometric curves were computed for each of the 11 mice. On average, mice displayed the highest performance on the strongest stimulus intensity, which was the 1 ms pulse duration (WHit rate = 0.79 ± 0.11 , AHit rate = 0.79 ± 0.03 , FA rate = 0.07 ± 0.02 , $n=11$, psychophysics) (**Figure 3.11.b**). Performance dropped considerably on the medium stimulus intensity, which was the 0.08 ms pulse duration (WHit rate = 0.49 ± 0.07 , AHit rate = 0.79 ± 0.03 , FA rate = 0.07 ± 0.02 , $n=11$, psychophysics) (**Figure 3.11.b**), and on the smaller stimulus intensity which was the 0.04 ms, performance was little above chance level (Whit rate = 0.12 ± 0.05 , AHit rate = 0.79 ± 0.03 , FA rate = 0.07 ± 0.02 , $n=11$, psychophysics) (**Figure 3.11.b**).

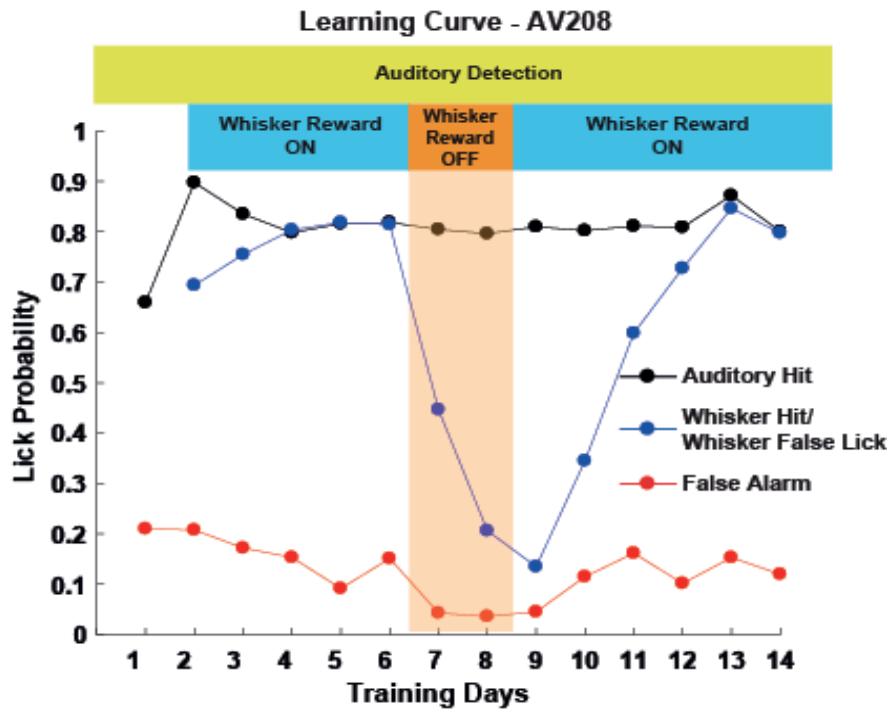
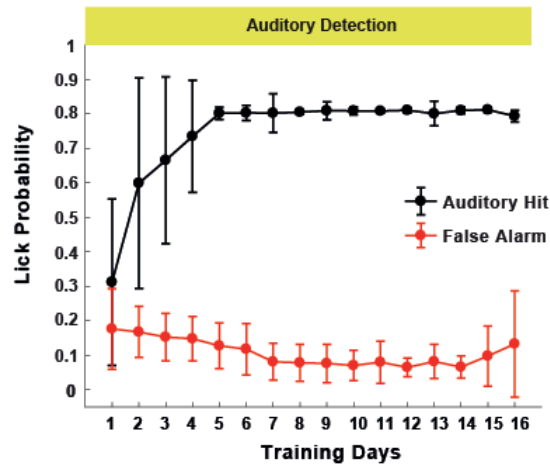
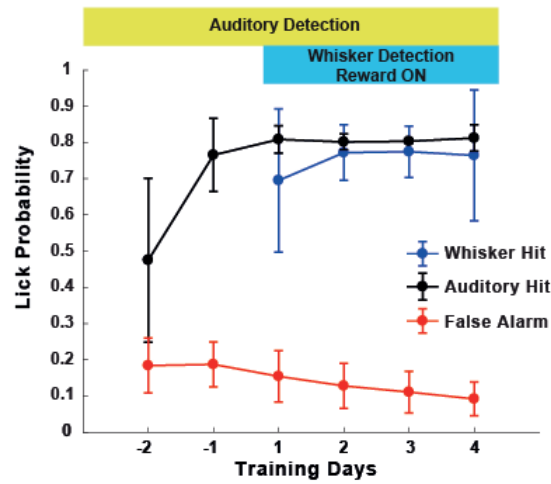


Figure 3.9: Example learning curve over days of mouse AV208.

a) Average Learning Curve (n=19) - Auditory Day 1 Align



b) Average Learning Curve (n=19) - Whisker Day1 Align



c) Average Learning Curve (n=19) - Extinction Day 1 Align

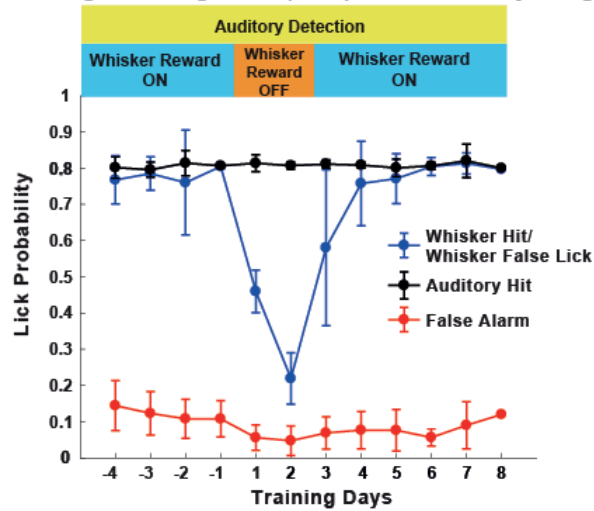


Figure 3.10: Average learning curves across all mice. a) Behavior data aligned on the 1st day of auditory detection. b) Behavior data aligned on the 1st day of whisker detection. c) Behavior data aligned on the 1st day of whisker extinction

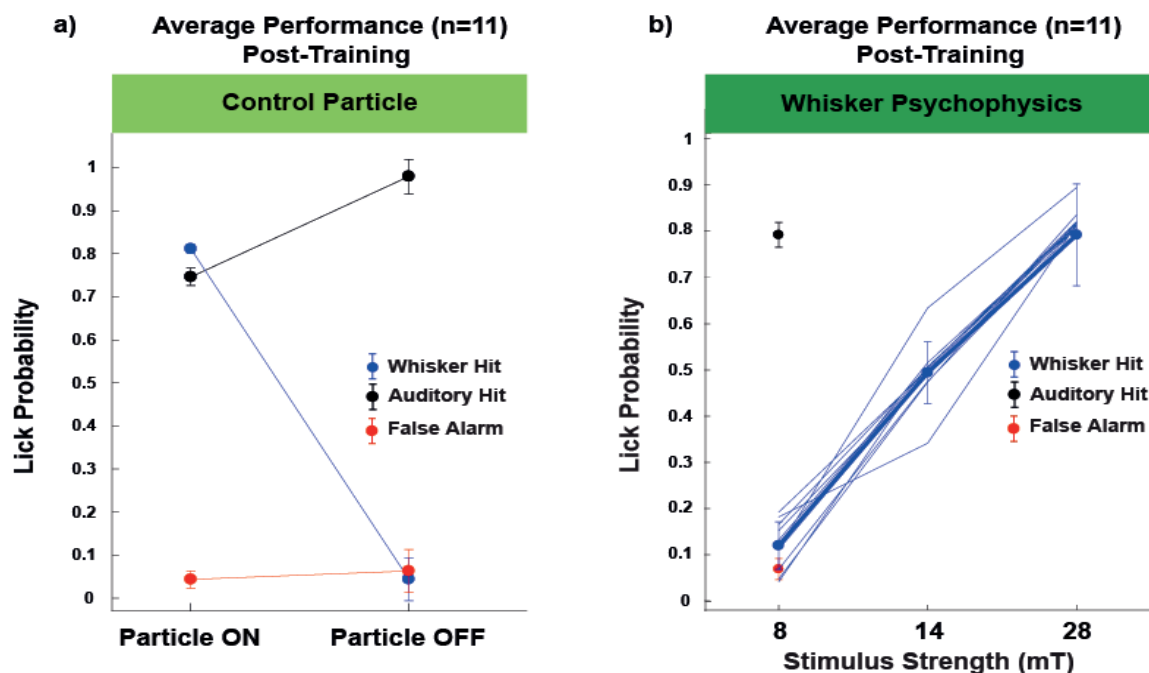
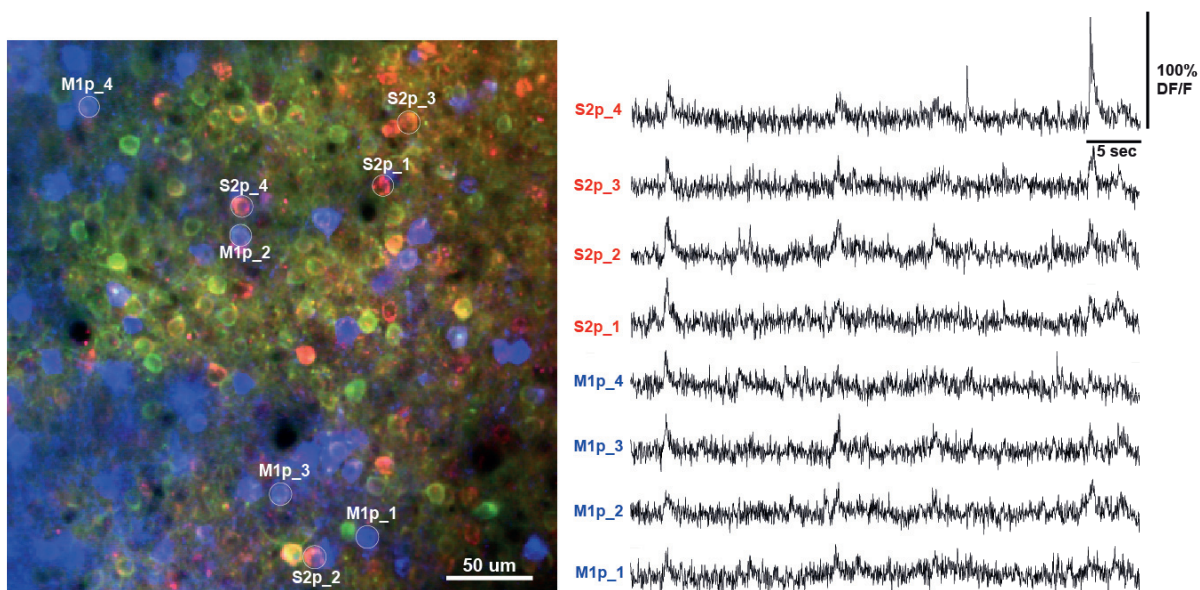


Figure 3.11: a) Control experiment when iron particle was on the whisker (Particle ON) and when iron particle was removed from the whisker (Particle OFF). b) Psychophysical experiment of whisker stimulus strength for three different stimulus intensities.

3.3.2 Two-photon calcium imaging during task learning

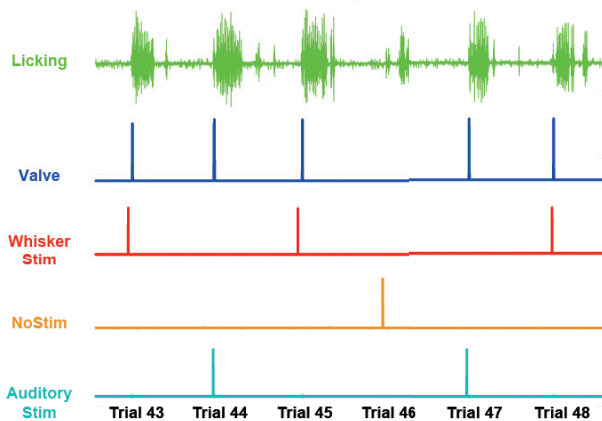
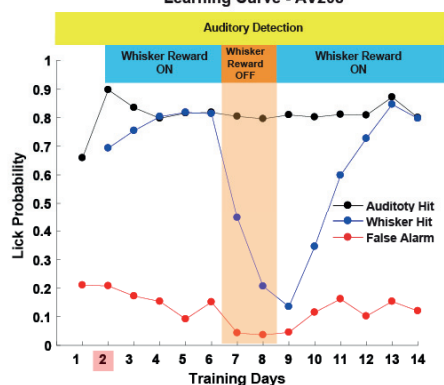
I performed in vivo calcium imaging of layer 2/3 neurons (at ~200 μm depth) through a cranial window using GCamp6f, a genetically encoded calcium (Figure 3.12.a). I acquired imaging data from 19 mice, but for the current analysis, I have used data from only 6 mice. These mice were selected based on their high fluorescence levels of both retrograde tracers in S2p and M1p neurons. In addition, most of the selected mice (5 out of 6) had undergone all training phases including the control particle and psychophysics. Neurons were chronically followed throughout all training sessions. I analysed calcium signals in a total of 1704 neurons (whole population including S2p and M1p neurons), 311 S2p neurons, and 234 M1p neurons. Neurons displayed heterogeneous calcium signals, with varying amplitudes and differences in trial-by-trial variability, but with subsets clearly responding to auditory stimuli, to whisker stimuli, or both, while others responded to unrewarded licking (Figure 3.12.a). Figure 3.12, describes the results from an example mouse (AV208), in which I observe overlaid single trial responses on

a)

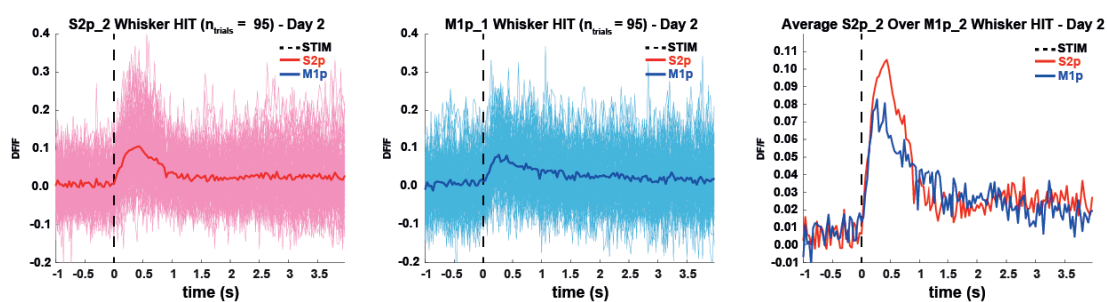


GCaMP6f CTB-Alexa 594 CTB-Alexa 647

Learning Curve - AV208



b)



c)

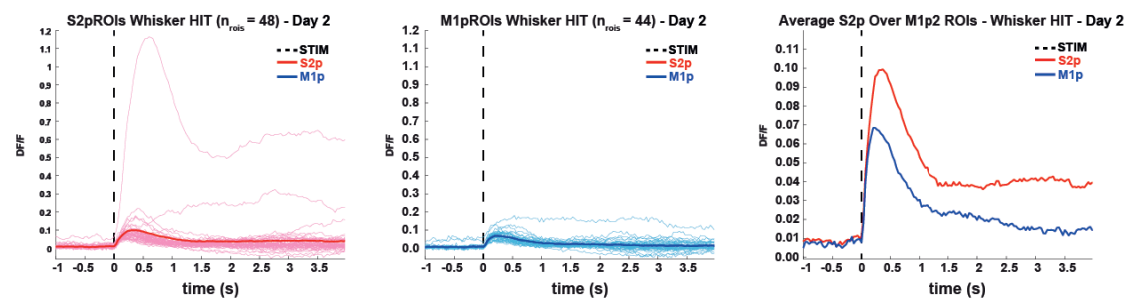


Figure 3.12 Two-photon calcium imaging in layer 2/3 of the C2 barrel column during the detection task in an example mouse. a) (on the left) Two-photon image of S2p and M1p neurons in the C2 barrel column at ~200 μ m depth. Superimposed image of 3-channels (see Figure 3.5): S2p neurons labelled with CTB Alexa-594 in red; M1p neurons labelled with CTB Alexa-647 in blue; GCaMP6f expressing neurons in green. (on the right) Single-trial example calcium traces of selected S2p (red) and M1p (blue) neurons at 6 consecutive trials. (below calcium image) Learning curve of the example mouse. b) Overlaid single-trial calcium traces of whisker hit trials for a selected S2p neuron (S2p_2) and a selected M1p neuron (M1p_1) during training session 2, which is the day that the whisker stimulation starts. Thin line indicates individual trial traces, and thick line indicates the average calcium trace in this session. (on the right). Overlaid average calcium traces of the selected S2p and M1p neuron. c) Overlaid average calcium traces of whisker hit trials for individual S2p and M1p neurons during training session 2, which is the day that the whisker stimulation starts. Thin line indicates average traces individual neurons, and thick line indicates grand average calcium trace of S2p and M1p, respectively (on the right). Overlaid grand average calcium traces of S2p and M1p neurons.

whisker hit trials of one example S2p neuron (in red) and one M1p neuron (in blue) in a single session (day 2 of whisker stimulus detection) aligned to whisker stimulus event (**Figure 3.12.b**). Their average traces showed that both neurons responded in whisker hit trials, with the S2p neuron exhibiting a stronger response than the M1p neuron during reward window (1 sec after stimulation). The average calcium transients of all S2p and M1p neurons in this mouse demonstrated that S2p responses were larger than M1p not only during the reward window but also across a prolonged post-stimulus period (**Figure 3.12.c**).

I then investigated calcium responses of the whole population of L2/3 neurons (n=268) in S1 of the same mouse during the execution of the task across learning sessions and the different reward and stimulus conditions. I averaged the sensory-evoked responses for each trial type (Whit, WMiss, AHit, and AMiss) (**Figure 3.13**). At the first day of training, in which mice were trained to auditory detection, neurons were responsive only to auditory hit and not auditory miss trials. At the first day of whisker stimulus presentation (second panel), in which mice were trained to whisker and auditory detection, I observed that the neuronal population responded to whisker hit, whisker miss and auditory hit trials, but calcium signals in whisker hit trials were stronger than the other two trial types. In both whisker hit and whisker miss trials, I noticed similar early sensory responses, but a much larger late phase response and a sustained activity after reward window (>1 sec) in whisker hit trials, compared to whisker miss trials in which early re-

sponse returned to baseline shortly after whisker stimulation. Auditory hit response was smaller and delayed compared to both whisker hit and miss trials, but lasted throughout the trial duration and displayed an increase after the reward window that reached the same level as the sustained response after reward window in whisker hit trials. Longitudinal observation across training phases showed a gradual reduction of calcium responses on whisker hit, compared to whisker miss trials in which activity remained relatively stable. Given that mice learned to withhold their licking to whisker stimulation, in the two extinction sessions I notice that the sustained response after reward window was completely suppressed in whisker false lick trials. Only after reward was reinstated, sustained response after reward window gradually increased (day 4 after extinction), but was less prominent than in early training sessions. Auditory hit trial responses also displayed a progressive reduction across sessions.

Similar results were observed in the grand average responses across mice ($n=6$) (**Figure 3.14**). The grand average fluorescence time courses indicate that neurons in L2/3 ($n=1704$) responded to whisker hit/false lick, whisker miss/correct rejection, auditory hit, auditory miss and false alarm trials. The strongest neural response was observed in whisker hit trials and displayed a sustained activity after reward window only in early training sessions. Whisker hit transients exhibited a reduction over sessions. Grand average calcium response in whisker miss trials was smaller than whisker hit, and similarly to the example mouse data, returned back to baseline shortly after stimulation. Whisker miss transients remained stable over sessions. As expected, grand average auditory hit response was smaller and delayed compared to whisker hit and miss trials, and remained stable over sessions. I found that some L2/3 neurons were also activated in auditory miss trials, with a similar delay to auditory hit trials, but much smaller amplitude and duration. Grand average auditory miss responses remained relatively stable across sessions. Furthermore, I also found L2/3 neurons in C2 barrel responding to spontaneous unrewarded licking (false alarm trials). These findings demonstrate that L2/3 neuronal population responded to both whisker and auditory stimulation, with whisker stimulus evoked responses been stronger and faster than in auditory stimulation across all sessions and reward conditions. Responses in S1 correlated with task performance, and those responses remained relatively stable across most training sessions and under different reward conditions.

A similar pattern of results was obtained in S2p neurons ($n=48$) for both the example mouse and grand average responses across mice (**Figure 3.15**, **Figure 3.16**). In the

example mouse data, the response of S2p neurons was overall smaller than the whole population of neurons in whisker hit, whisker miss and auditory hit responses in most training sessions. In grand average responses, there was a small reduction comparing S2p neurons and the whole population observed in whisker miss and auditory hit trials, while those responses remained stable over sessions. However, a larger overall reduction comparing S2p neurons and the whole population was observed in whisker hit trials. In addition, a noticeable decrease was observed when comparing whisker hit calcium transients of the first session (whisker detection day 1) to all other training sessions. In both the example mouse and grand average data, the response pattern in M1p neurons (n=44) was analogous to S2p neurons, but considerably reduced especially for whisker hit and auditory hit trials (**Figure 3.17, Figure 3.18**). These results suggest that both S2p and M1p neurons responded to both whisker and auditory stimulation, with whisker stimulus evoked responses been stronger and faster than in auditory stimulation across all sessions and reward conditions. Overall, both S2p and M1p neurons exhibited similar but smaller amplitude responses compared to the whole L2/3 population of neurons in S1.

Next, I compared average responses between S2p and M1p neurons in whisker hit, whisker miss, auditory hit and auditory miss trials for both the example mouse and across all mice over sessions. In whisker hit trials of the example mouse data (**Figure 3.19**), responses of S2p neurons were clearly stronger than M1p neurons, especially in early training sessions and late sessions after extinction, in which the mouse reinstated high performance. This difference was very small in the second day of extinction and the two following days, in which the mouse was clearly ignoring whisker stimulation. In grand average responses across mice, S2p neural responses were stronger than M1p, their difference remained relatively stable across all sessions (**Figure 3.20**). Calcium signals in whisker miss trials, for both the example mouse and grand average data (**Figure 3.21, Figure 3.22**), were slightly larger in S2p than M1p neurons. This small difference remained stable across sessions and reward conditions. In auditory hit trials, responses were larger for S2p neurons than M1p in the example mouse average data, but only in early training sessions and late sessions after extinction, in which the mouse reinstated high performance (**Figure 3.23**). However, in auditory hit grand average data (**Figure 3.24**), S2p responses were larger than M1p, and this difference remained stable across all training sessions. Finally, when comparing results of S2p and M1p neurons in auditory miss trials, there was no difference in their responses across all sessions in both the example mouse and grand average data (**Figure 3.25, Figure 3.26**). Taken together these

data demonstrated a stronger response in S2p neurons compared to M1p that correlated with task performance, and remained relatively stable across most training sessions and under different reward conditions.

These findings are in agreement for all six mice used in the current analysis. **Figure 3.27**, displays data of individual mice in a single training session (whisker detection day 2) for whisker hit trials, in which again I observed that S2p responses were stronger than M1p in all six mice. I then quantified the mean peak response within 1 sec reward window, as well as the mean response for five different phases after stimulus presentation: very early (33-132 ms), early (132-231 ms), late (231-429 ms), very late (429-1000 ms), and hyper late (1000-3600 ms). I found that the mean peak response in the reward window for whisker hit trials was significantly higher in S2p neurons compared to M1p (peak DF/F S2p: 0.086 ± 0.016 , M1p: 0.059 ± 0.014 , $p = 0.03125$, $n = 6$ mice, Wilcoxon signed-rank paired test). Similarly, S2p mean responses were significantly higher than M1p for all the different phases (very early DF/F S2p: 0.019 ± 0.005 , M1p: 0.015 ± 0.005 , $p = 0.03125$; early DF/F S2p: 0.052 ± 0.013 , M1p: 0.036 ± 0.010 , $p = 0.03125$; late DF/F S2p: 0.069 ± 0.018 , M1p: 0.042 ± 0.014 , $p = 0.03125$; very late DF/F S2p: 0.042 ± 0.015 , M1p: 0.023 ± 0.009 , $p = 0.03125$; hyper late DF/F S2p: 0.016 ± 0.011 , M1p: 0.002 ± 0.006 , $p = 0.03125$; $n = 6$ mice, Wilcoxon signed-rank paired test). The smallest difference in activity during task performance between S2p and M1p neurons was observed during the very early (33 - 132 ms) period upon whisker stimulation. The largest difference in activity during task performance between S2p and M1p neurons was observed during the late (231-429 ms) and very late (429-1000 ms) period upon whisker stimulation. These results suggest that across mice, S2p neurons compared to M1p, not only exhibited a higher mean peak response correlated with task performance, but also a higher response in all the post-whisker-stimulus time windows during the trial, with the largest difference observed in the late and very late phase after whisker deflection.

I next analysed average responses of individual S2p ($n = 311$) and M1p ($n = 234$) neurons across all six mice (**Figure 3.28.a**). In a single training session (whisker detection day 2) for whisker hit trials, both cell types displayed diverse responses. However, on average S2p neuronal responses were larger than M1p (**Figure 3.28.b**). When comparing mean peak response in the reward window for single S2p and M1p neurons (**Figure 3.28.c**), I observed that S2p responses were significantly higher than M1p (peak DF/F S2p: 0.086 ± 0.077 , M1p: 0.059 ± 0.042 , $p = 0.042 \times 10^{-9}$, Wilcoxon rank sum unpaired test). I found similar results for all the different phases, demonstrating significantly higher

responses in S2p than M1p neurons (very early DF/F S2p: 0.019 ± 0.014 , M1p: 0.015 ± 0.011 , $p = 0.021$; early DF/F S2p: 0.052 ± 0.049 , M1p: 0.036 ± 0.028 , $p = 0.013 \times 10^{-4}$; late DF/F S2p: 0.069 ± 0.074 , M1p: 0.042 ± 0.044 , $p = 0.011 \times 10^{-7}$; very late DF/F S2p: 0.042 ± 0.055 , M1p: 0.023 ± 0.035 , $p = 0.059 \times 10^{-7}$; hyper late DF/F S2p: 0.015 ± 0.041 , M1p: 0.001 ± 0.027 , $p = 0.055 \times 10^{-4}$; Wilcoxon rank sum unpaired test). Again, the smallest difference in activity during task performance between S2p and M1p neurons was observed during the very early (33 - 132 ms) period, and the largest difference was observed during the late (231-429 ms) and very late (429-1000 ms) periods. These findings suggest that although both S2p and M1p neurons displayed a diversity of sensory evoked responses, on average these responses were higher in S2p neurons than M1p for all the observed time windows during the trial, with the largest difference observed in the late and very late phase after whisker deflection.

Observations on whisker hit trials across training sessions showed that the mean peak response of S2p neurons remained higher than M1p neurons in all sessions (**Figure 3.29**). However, both S2p and M1p mean peak responses displayed an overall reduction over sessions. A similar response pattern was observed in the late (231-429 ms) and the very late (429-1000 ms) phases. In the early phase (132-231 ms), even though response was stably higher in S2p than M1p neurons over sessions, there was a less marked reduction observed in S2p neurons across days, whereas M1p neurons appeared to reduce their early phase response across training days. In the very early phase (33-132 ms), S2p stimulus evoked response was slightly higher than M1p, but both responses remained stable across sessions. Likewise, in the hyper late post-reward phase (1000-3600 ms), S2p response was a little higher than M1p. Together, these results demonstrate that S2p response remained higher than M1p across all training sessions, but both displayed a progressive reduction in their peak responses as well as in late and very late phases during the trial.

In the last part, I analysed responses during spontaneous unrewarded licking (lick triggered analysis on false alarm trials) (**Figure 3.30**). Both S2p and M1p neurons responded before and during the tongue contact with the water spout (1st lick). When comparing S2p and M1p average neuronal responses across mice, I observed that in the very first training session (auditory detection day 1) S2p response appeared to be only a little higher than the M1p. However, over the course of training this difference between S2p and M1p responses appeared to increase (in whisker detection day 1, day 2, and day before extinction). During the two extinction sessions, the difference between S2p and M1p

response seemed slightly reduced and resembled that of the very first training session (auditory detection day 1). When the reward on the whisker stimulation trials was reinstated, the difference between S2p and M1p response gradually appeared to display a small increase. These findings suggest that both S2p and M1p neurons responded during spontaneous licking, but S2p neuronal response was larger than M1p across sessions.

Next, I analysed average responses of individual S2p ($n = 311$) and M1p ($n = 234$) neurons during spontaneous unrewarded licking in a single training session (whisker detection day 2) and across mice (**Figure 3.31.a, b & c**). Most S2p and M1p neurons displayed a diversity of responses during spontaneous licking (**Figure 3.31.a**). Larger calcium responses were observed for S2p neurons compared to M1p neurons (**Figure 3.31.b**). I then quantified mean response before (100 - 33 ms) and after (33 - 165 ms) the mouse tongue first contacted the spout (1st lick) (**Figure 3.31.c**). Licking-related average calcium response before the 1st lick was significantly higher in S2p neurons (before 1st lick DF/F S2p: 0.023 ± 0.039 , M1p: 0.013 ± 0.022 , $p = 0.14 \times 10^{-3}$; Wilcoxon rank sum unpaired test). Similarly, the average calcium response after the 1st lick was also larger in S2p neurons compared to M1p (after 1st lick DF/F S2p: 0.037 ± 0.059 , M1p: 0.021 ± 0.031 , $p = 0.14 \times 10^{-3}$; Wilcoxon rank sum unpaired test). Finally, I followed mean responses before and after the 1st lick over sessions (**Figure 3.31.d**). S2p neuronal responses remained higher than M1p across all training sessions in both before and after the 1st lick period. These results show that although both S2p and M1p neurons displayed a diversity of responses during spontaneous licking, on average these responses were higher in S2p neurons than M1p and remained higher and relatively stable across sessions.

AV208 – All neurons

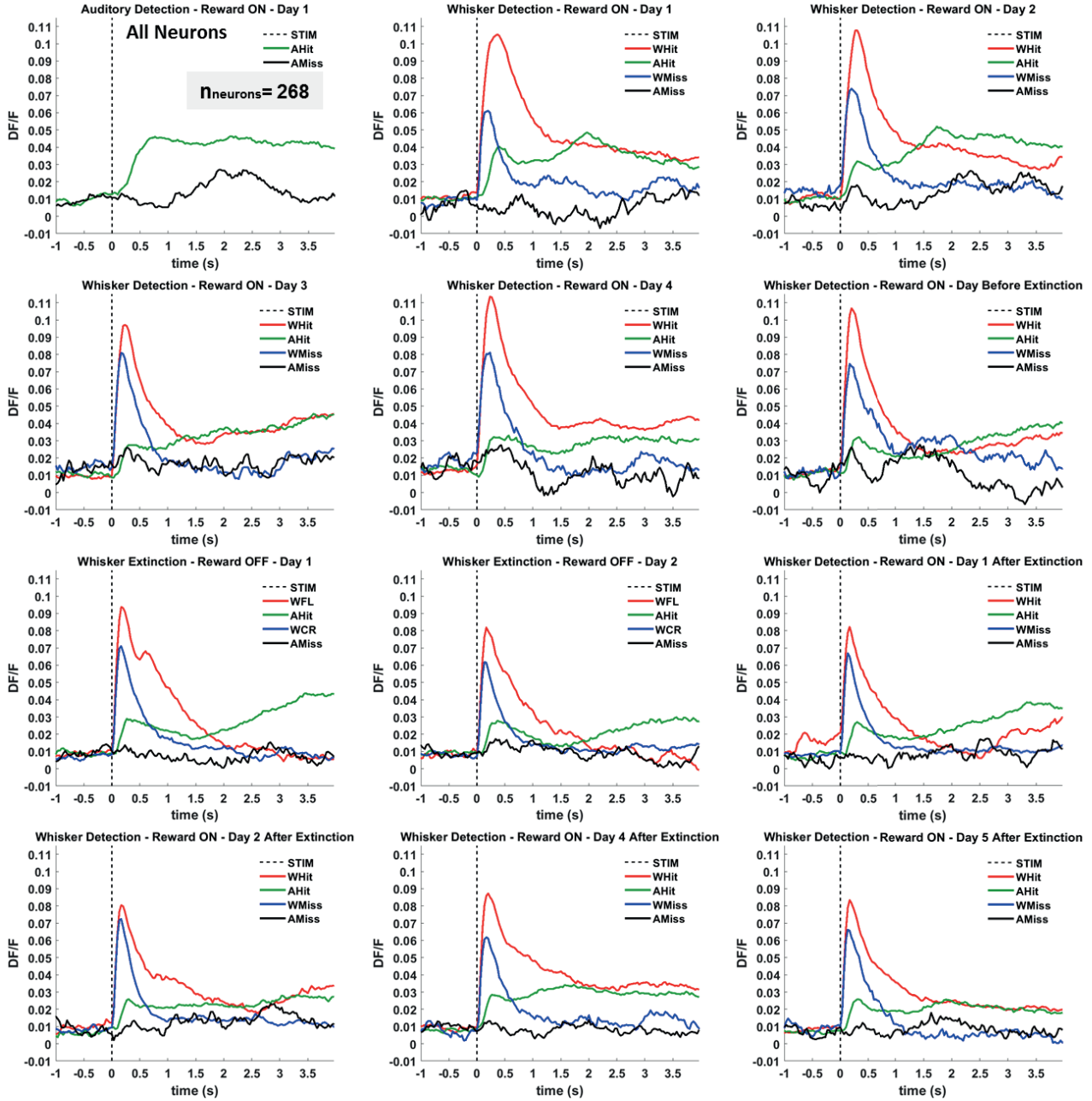


Figure 3.13: Average response of the whole population of L2/3 neurons in wS1 on different trial types (AHit: auditory hit, AMiss: auditory miss, WHit: whisker hit, WMiss: whisker miss, WFL: whisker false lick, WCR: whisker correct rejection) over training sessions for an example mouse (AV208). Dashed line indicates stimulation event.

Grand Average - All mice - All neurons

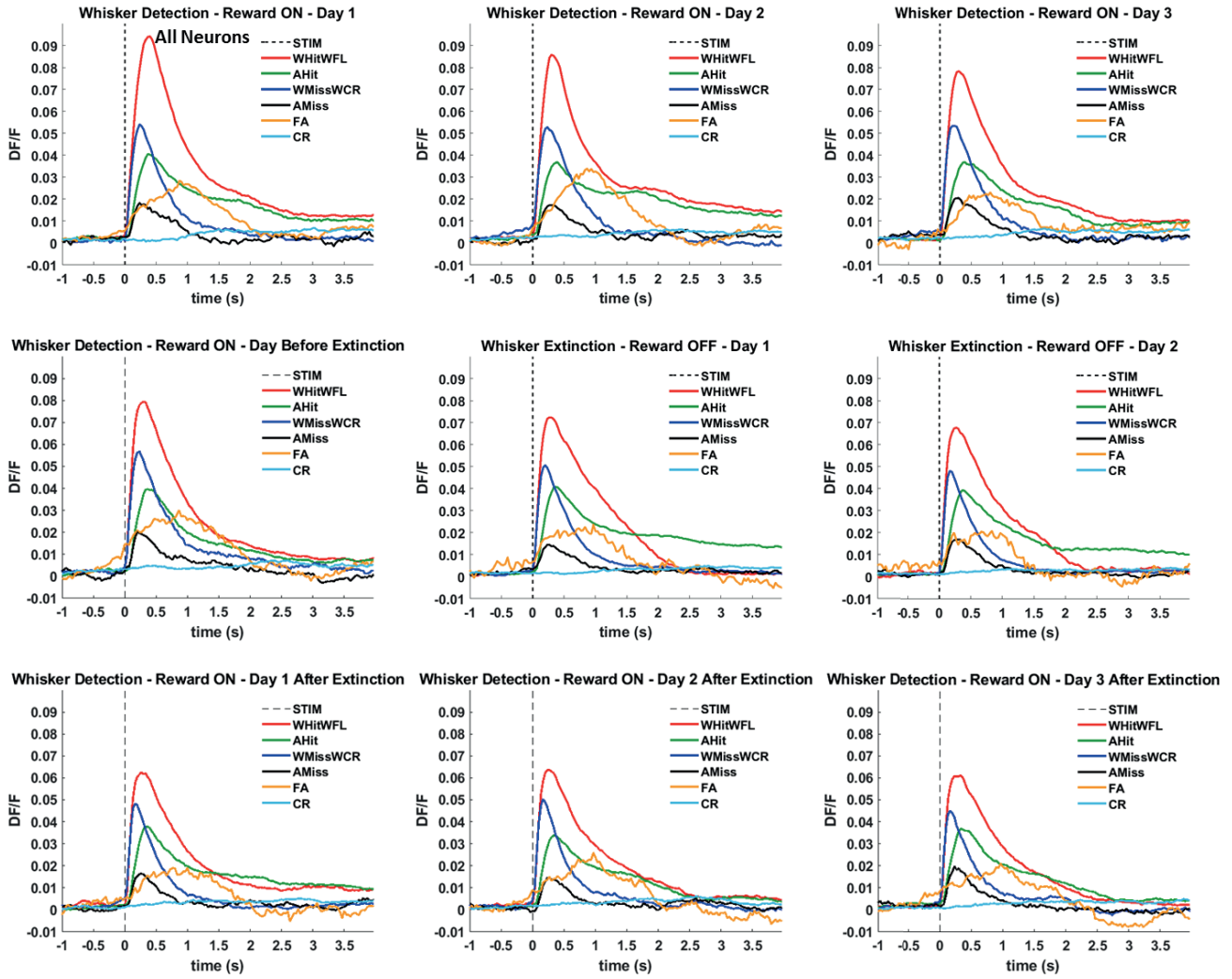


Figure 3.14: Grand average response of the whole population of L2/3 neurons in wS1 on different trial types (WHitWFL: whisker hit or whisker false lick, AHit: auditory hit, WMiss: whisker miss, AMiss: auditory miss, FA: false alarm, and CR: correct rejection) over training sessions across 6 mice. Dashed line indicates stimulation event.

AV208 – S2p neurons

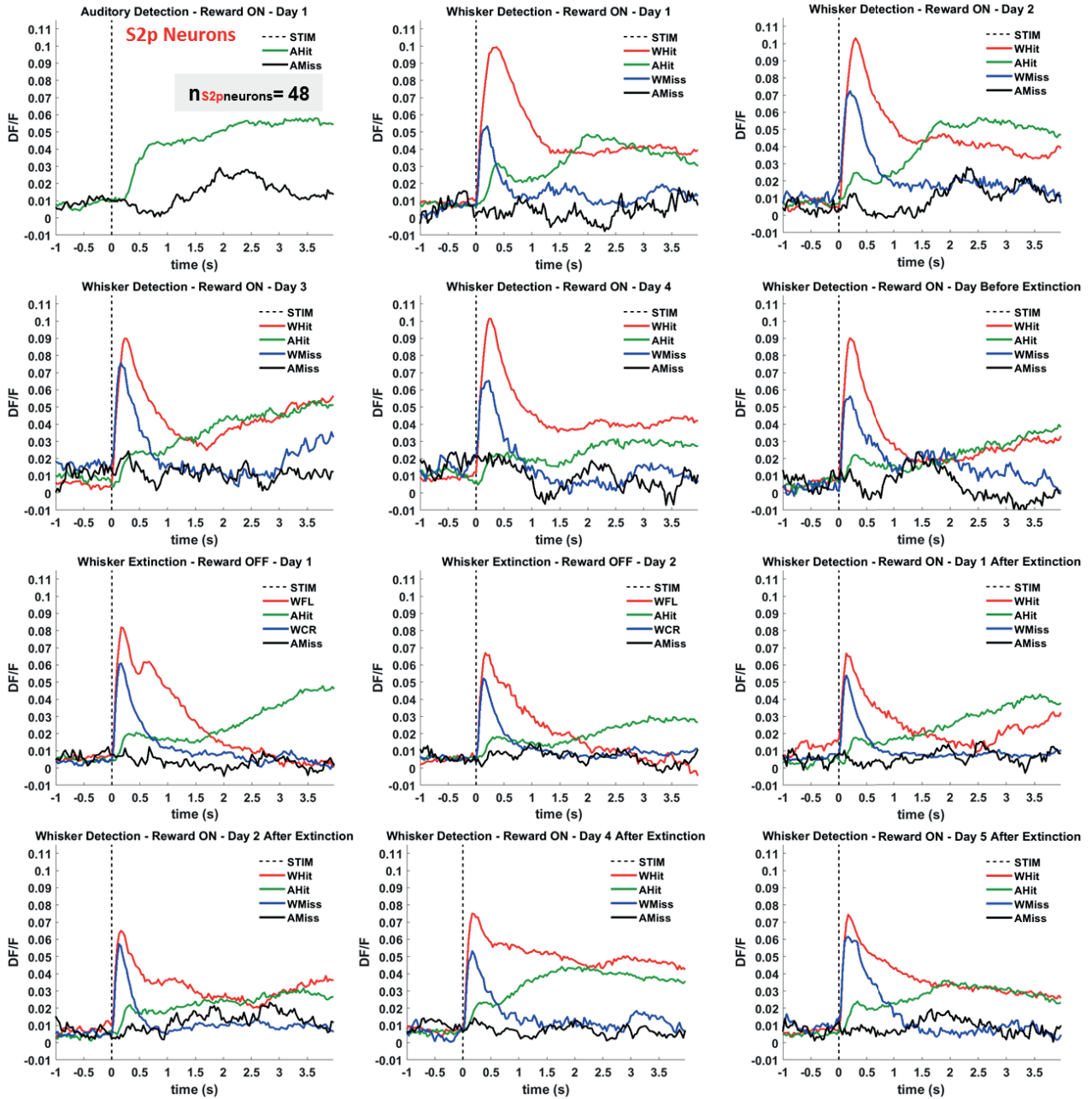


Figure 3.15: Average response of S2p neurons of L2/3 in wS1 on different trial types (AHit: auditory hit, AMiss: auditory miss, WHit: whisker hit, WMiss: whisker miss, WFL: whisker false lick, WCR: whisker correct rejection) over training sessions for an example mouse (AV208). Dashed line indicates stimulation event.

Grand Average - All mice - S2p neurons

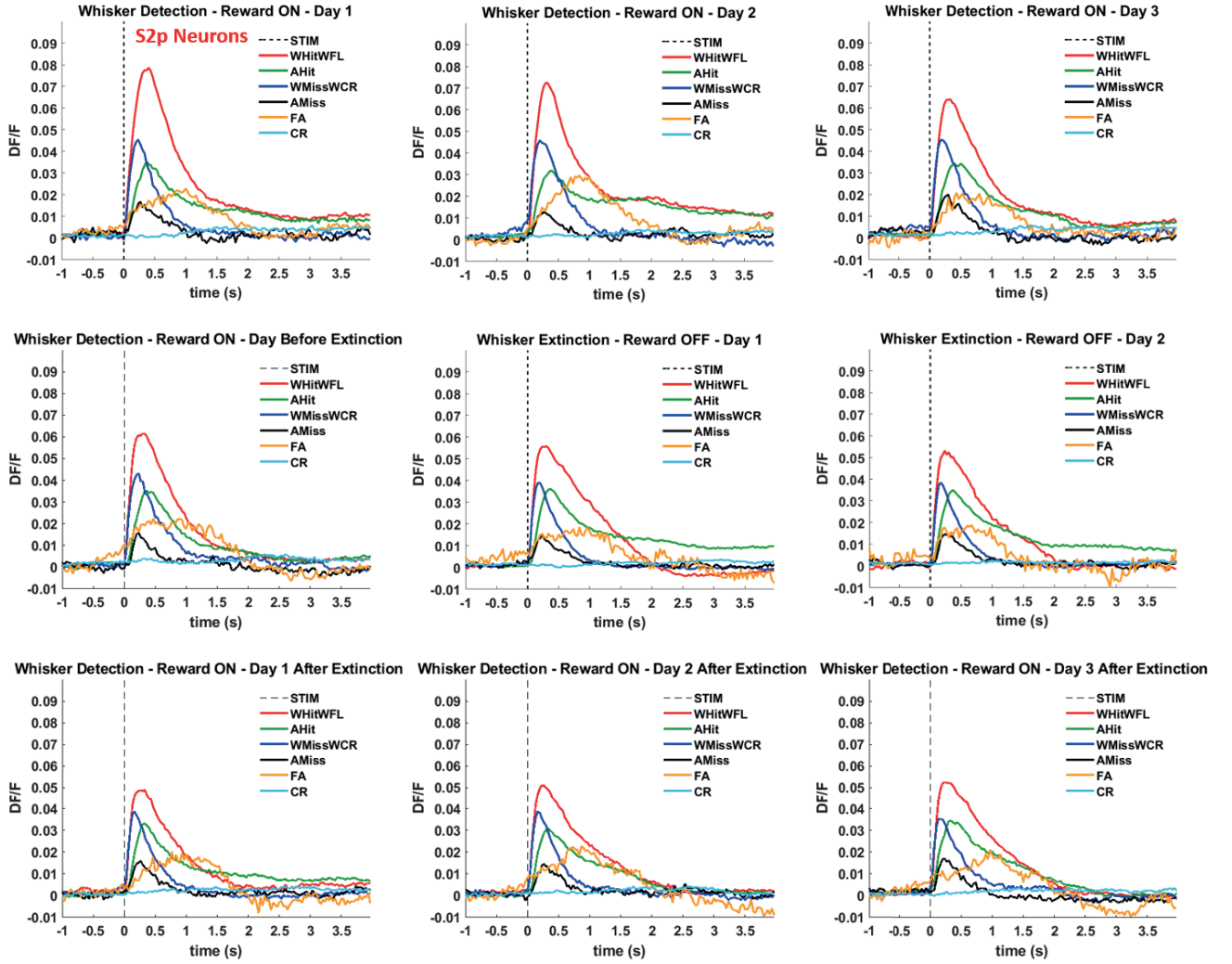


Figure 3.16: Grand average response of S2p neurons of L2/3 in wS1 on different trial types (WHitWFL: whisker hit or whisker false lick, AHit: auditory hit, WMiss: whisker miss, AMiss: auditory miss, FA: false alarm, and CR: correct rejection) over training sessions across 6 mice. Dashed line indicates stimulation event.

AV208 - M1p neurons

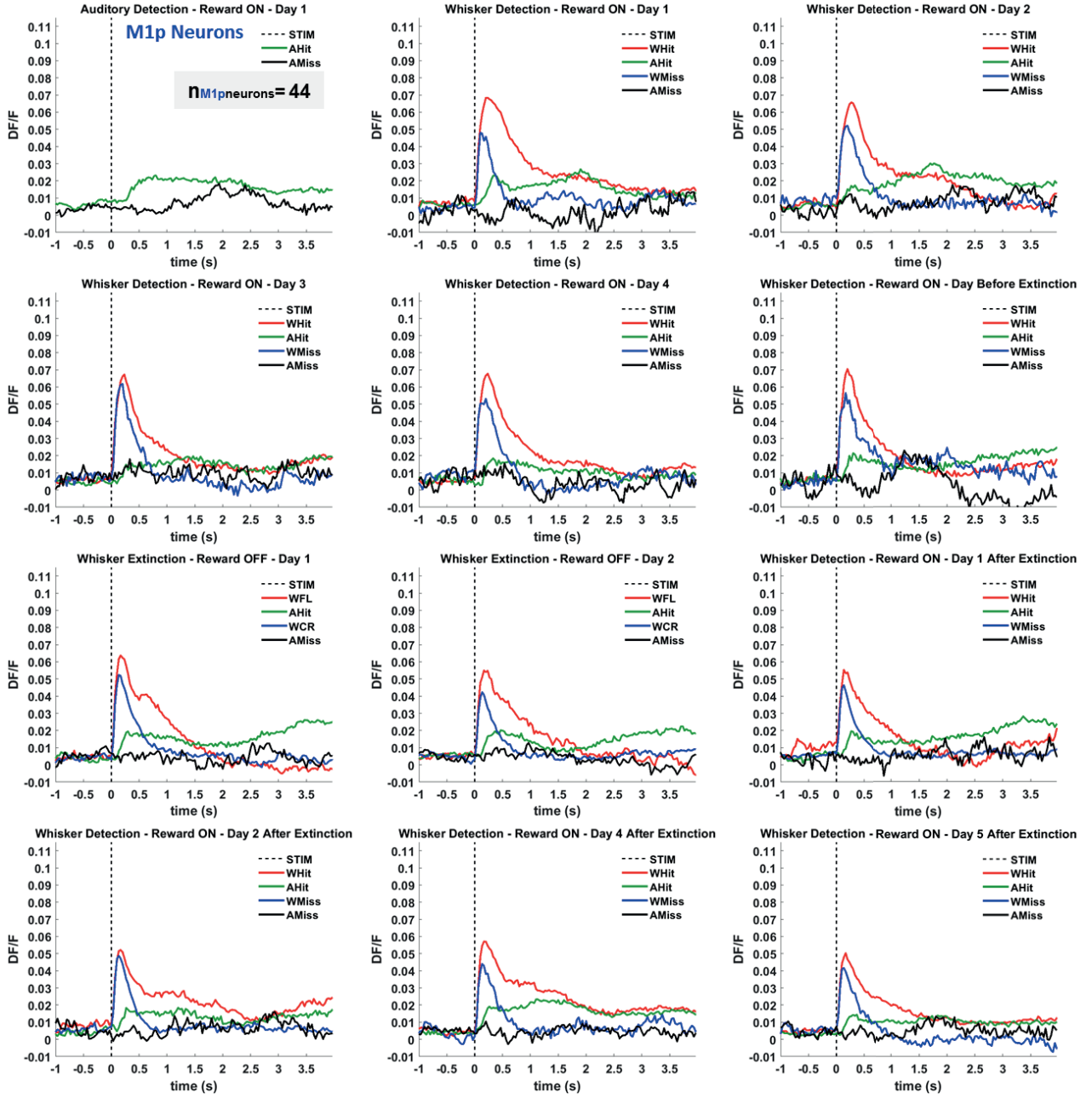


Figure 3.17: Average response of M1p neurons of L2/3 in wS1 on different trial types (AHit: auditory hit, AMiss: auditory miss, WHit: whisker hit, WMiss: whisker miss, WFL: whisker false lick, WCR: whisker correct rejection) over training sessions for an example mouse (AV208). Dashed line indicates stimulation event.

Grand Average - All mice - M1p neurons

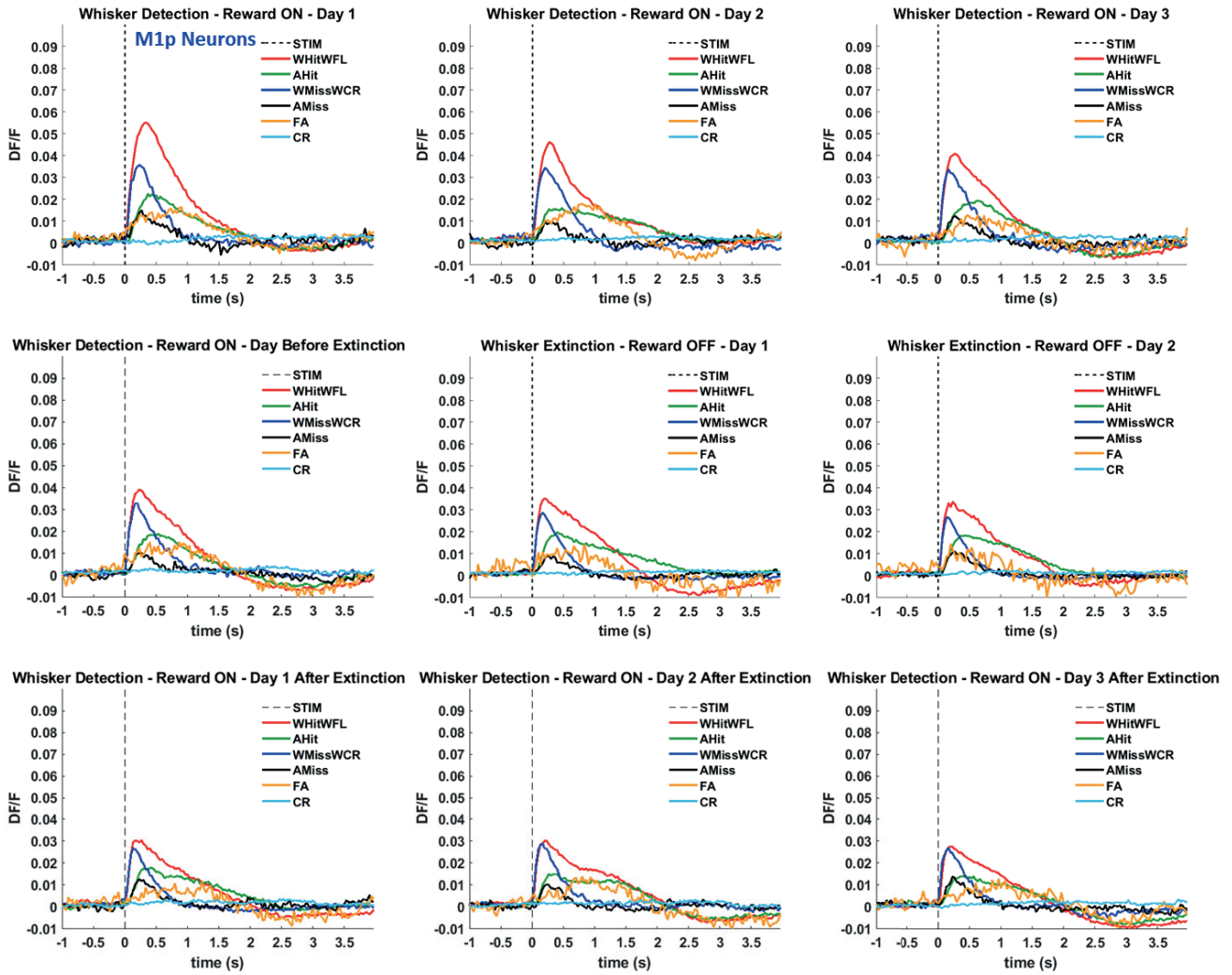


Figure 3.18: Grand average response of M1p neurons of L2/3 in wS1 on different trial types (WHitWFL: whisker hit or whisker false lick, AHit: auditory hit, WMiss: whisker miss, AMiss: auditory miss, FA: false alarm, and CR: correct rejection) over training sessions across 6 mice. Dashed line indicates stimulation event.

AV208 - Whisker hit trials S2p / M1p

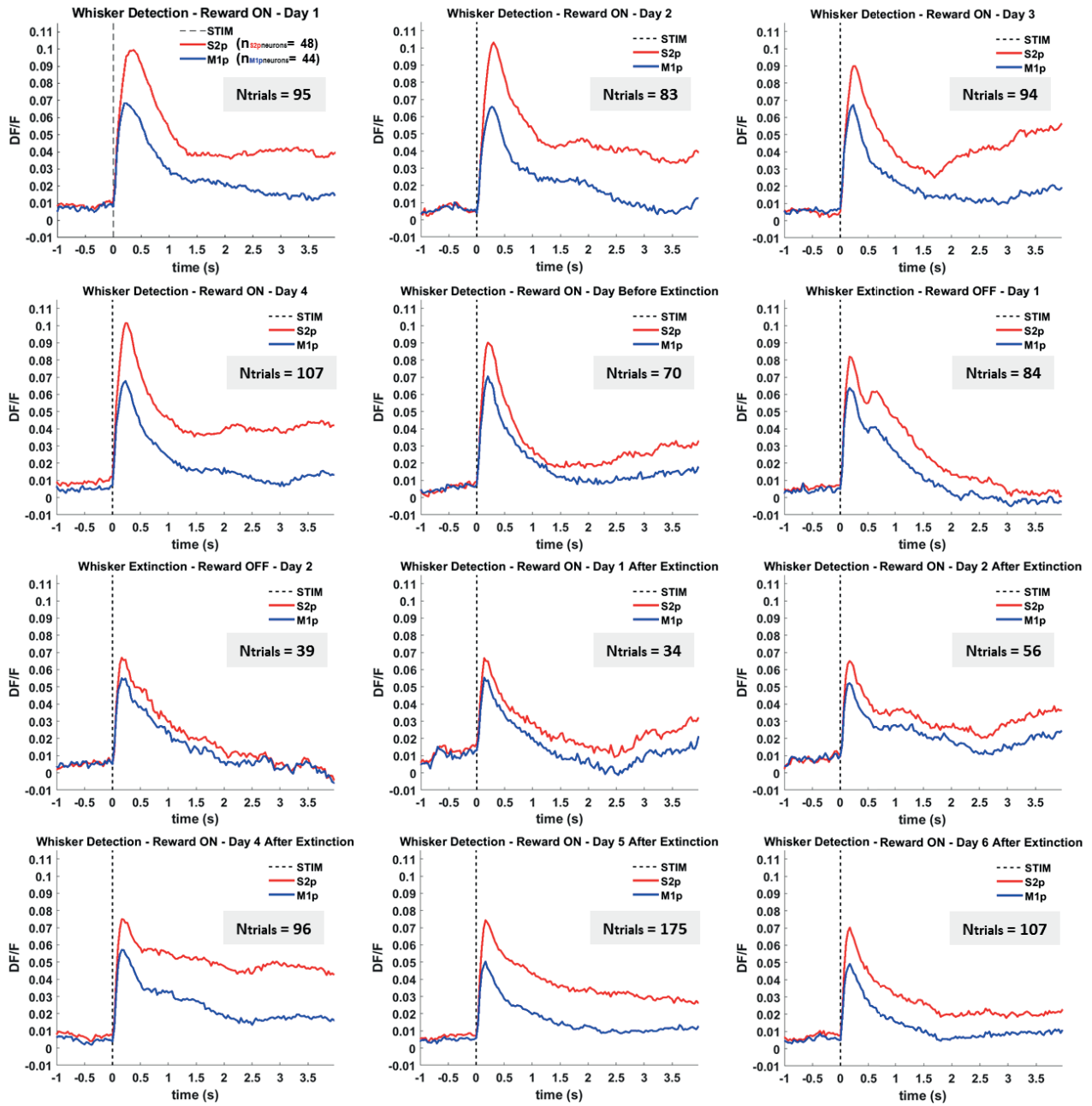


Figure 3.19: Average response of S2p and M1p neurons of L2/3 in wS1 on whisker hit trials over training sessions for an example mouse (AV208). Dashed line indicates stimulation event.

Grand Average - All mice - Whisker hit trials S2p / M1p

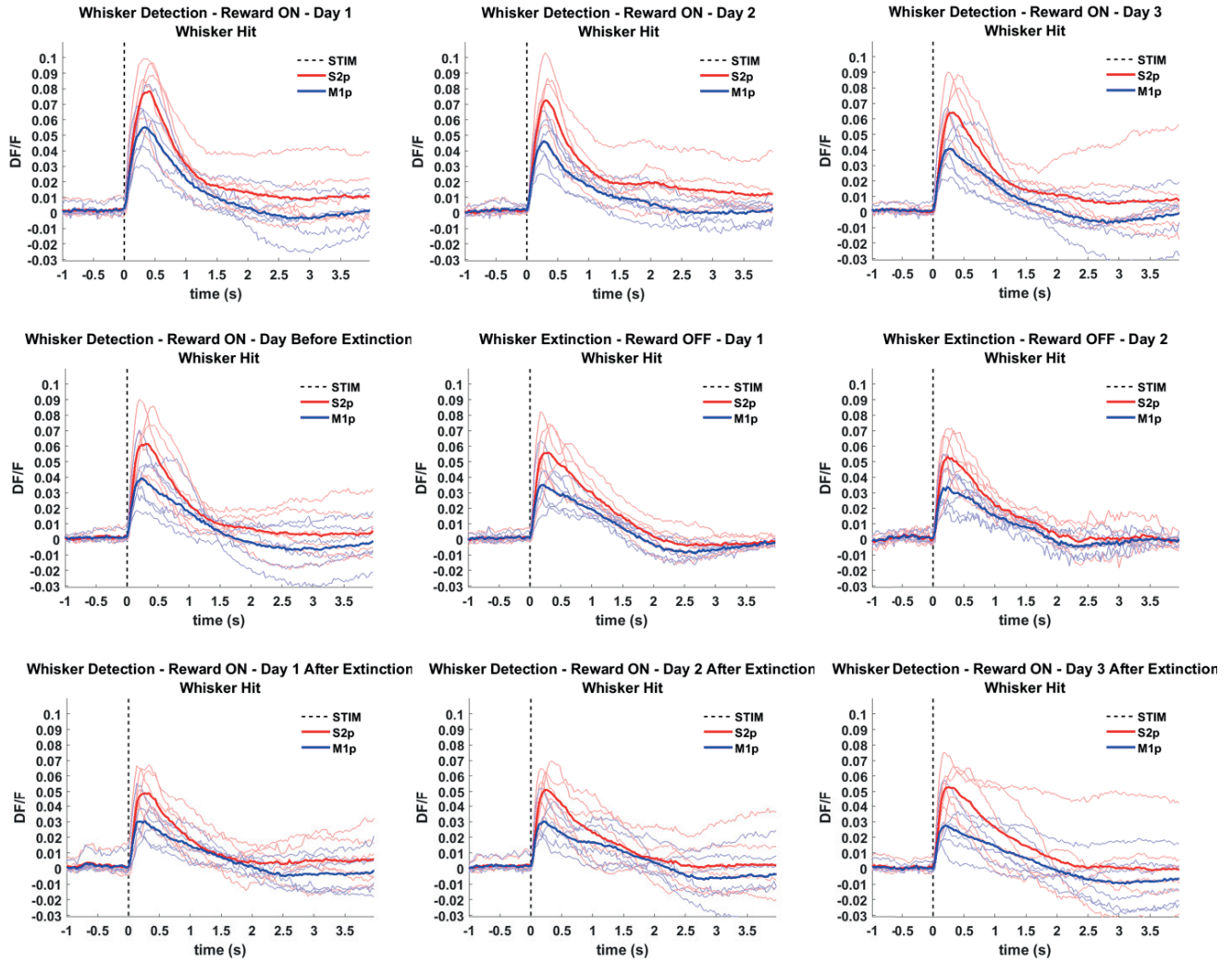


Figure 3.20: Grand average response of S2p and M1p neurons of L2/3 in wS1 on whisker hit trials over training sessions across 6 mice. Dashed line indicates stimulation event. Thick line corresponds to grand average calcium trace across mice, thin line corresponds to average calcium trace for a single mouse.

AV208 - Whisker miss trials S2p / M1p

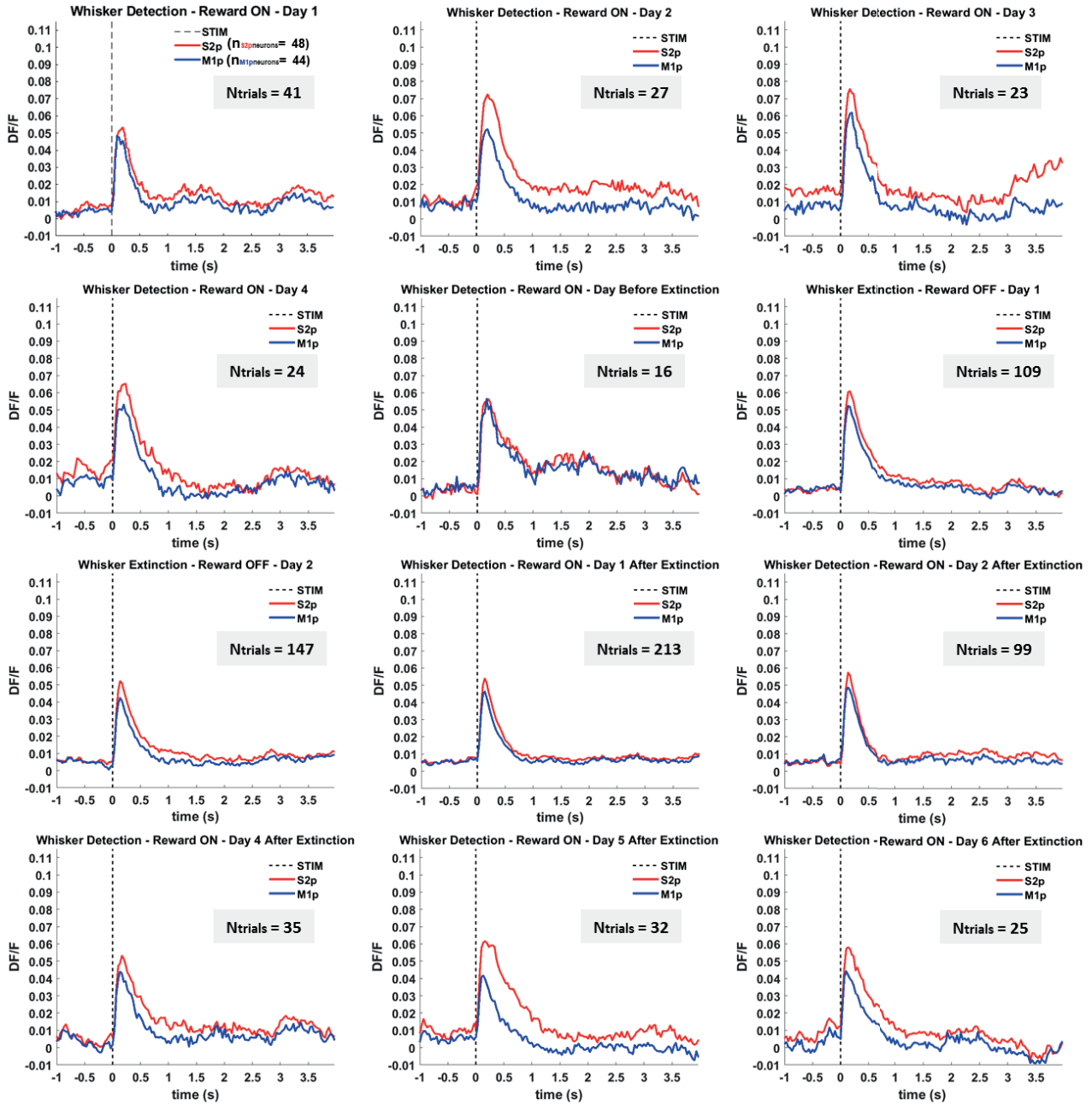


Figure 3.21: Average response of S2p and M1p neurons of L2/3 in wS1 on whisker miss trials over training sessions for an example mouse (AV208). Dashed line indicates stimulation event.

Grand Average - All mice - Whisker miss trials S2p / M1p

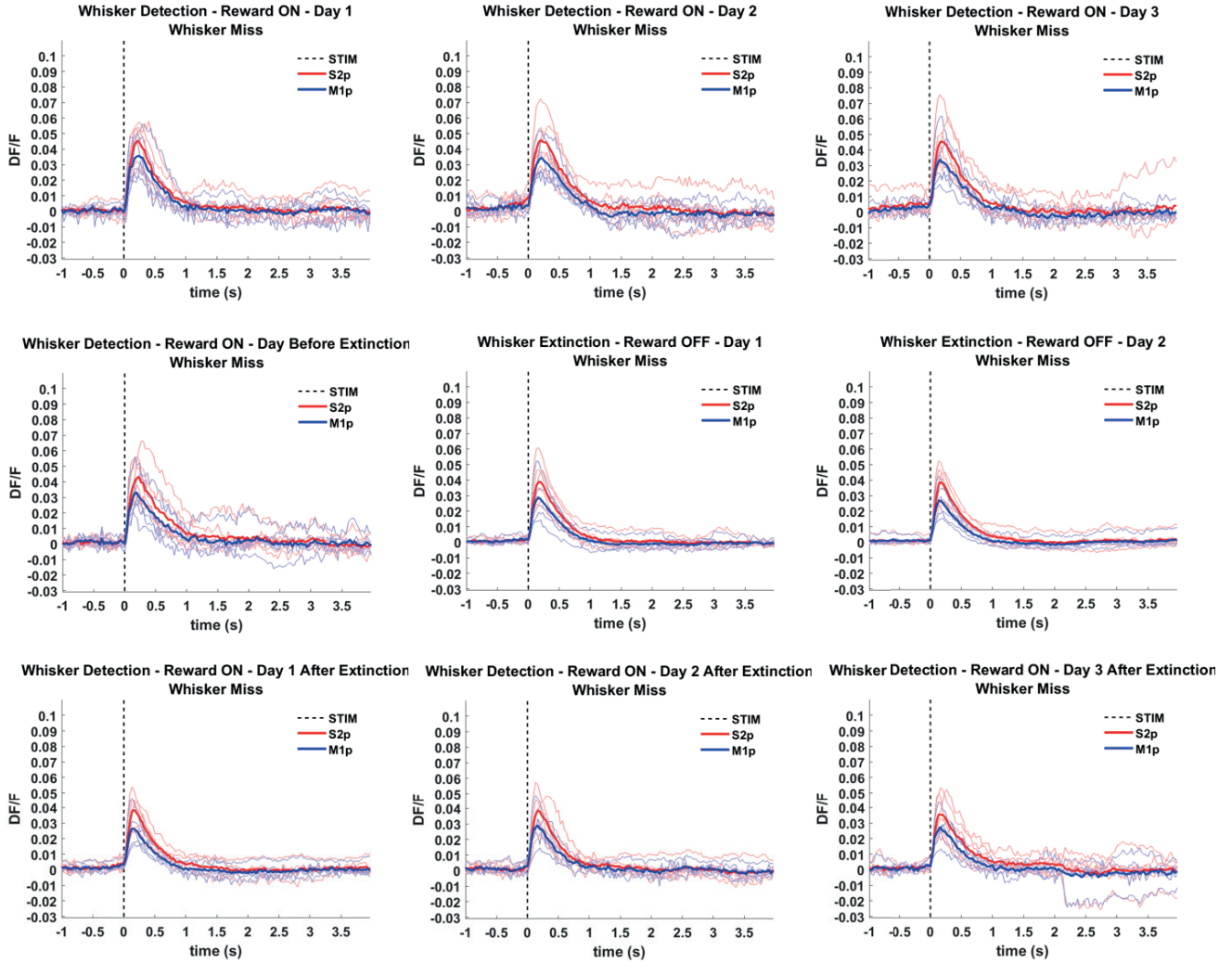


Figure 3.22: Grand average response of S2p and M1p neurons of L2/3 in wS1 on whisker miss trials over training sessions across 6 mice. Dashed line indicates stimulation event. Thick line corresponds to grand average calcium trace across mice, thin line corresponds to average calcium trace for a single mouse.

AV208 - Auditory hit trials S2p / M1p

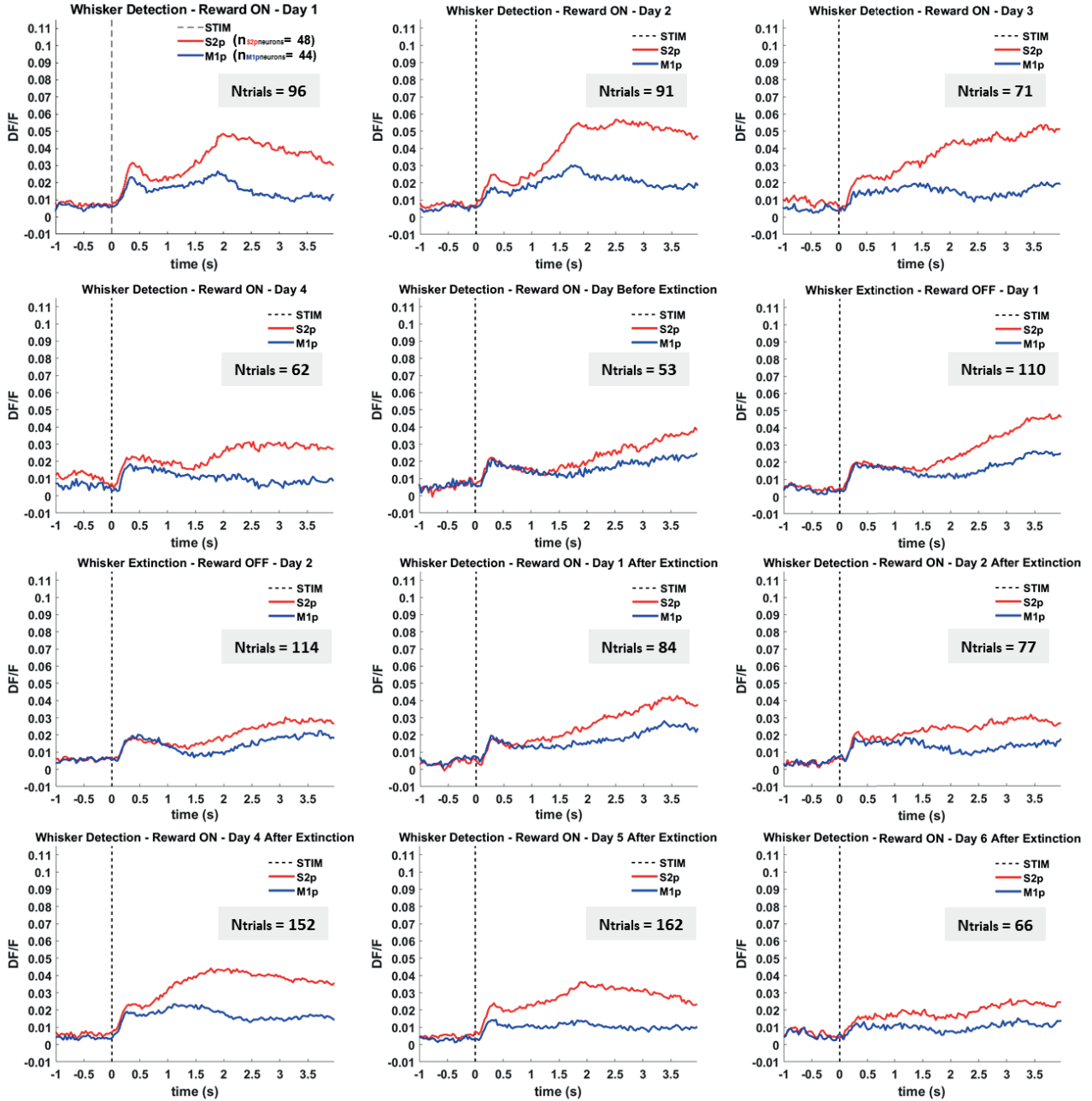


Figure 3.23: Average response of S2p and M1p neurons of L2/3 in wS1 on auditory hit trials over training sessions for an example mouse (AV208). Dashed line indicates stimulation event.

Grand Average - All mice - Auditory hit trials S2p / M1p

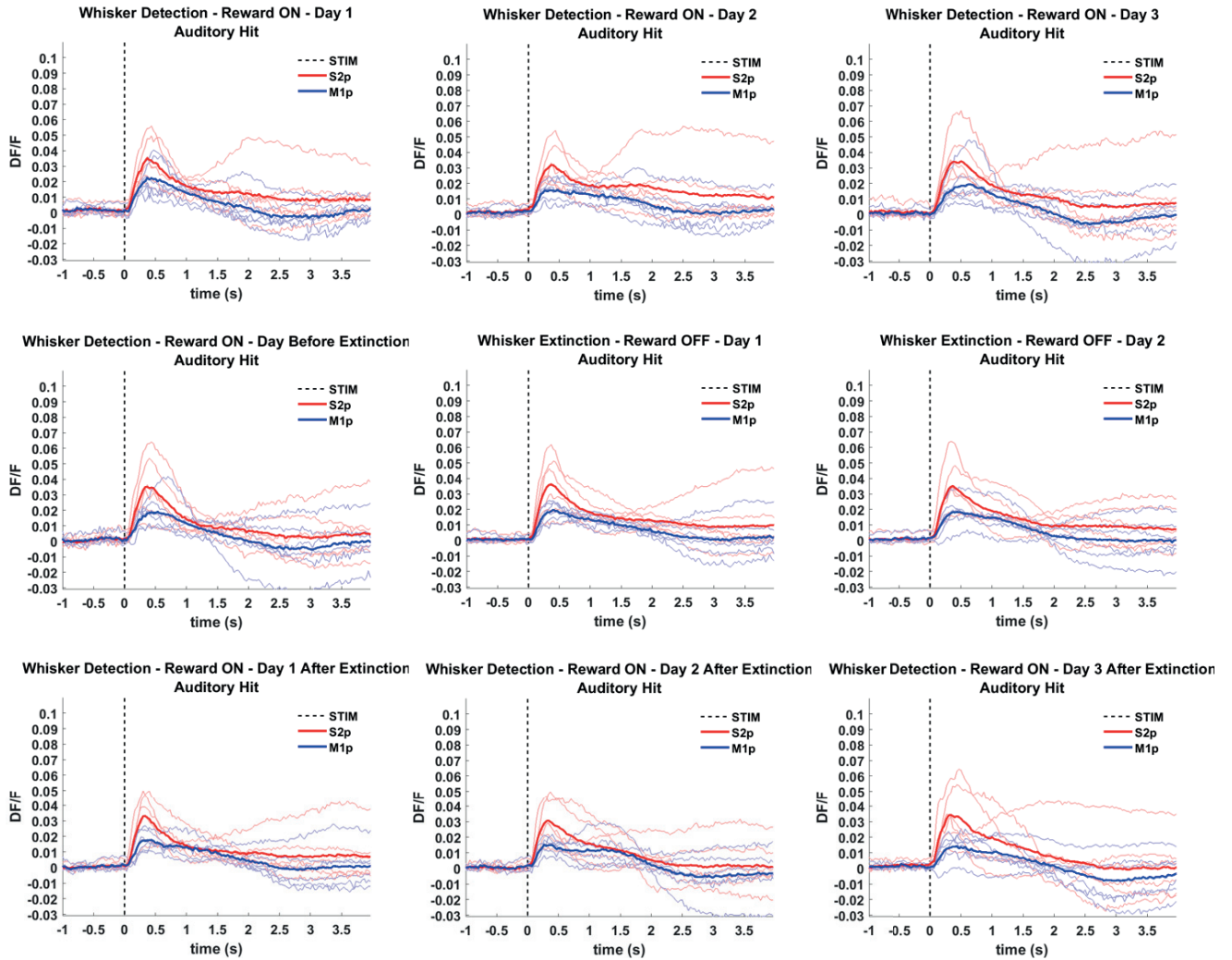


Figure 3.24: Grand average response of S2p and M1p neurons of L2/3 in wS1 on auditory hit trials over training sessions across 6 mice. Dashed line indicates stimulation event. Thick line corresponds to grand average calcium trace across mice, thin line corresponds to average calcium trace for a single mouse.

AV208 - Auditory miss trials S2p / M1p

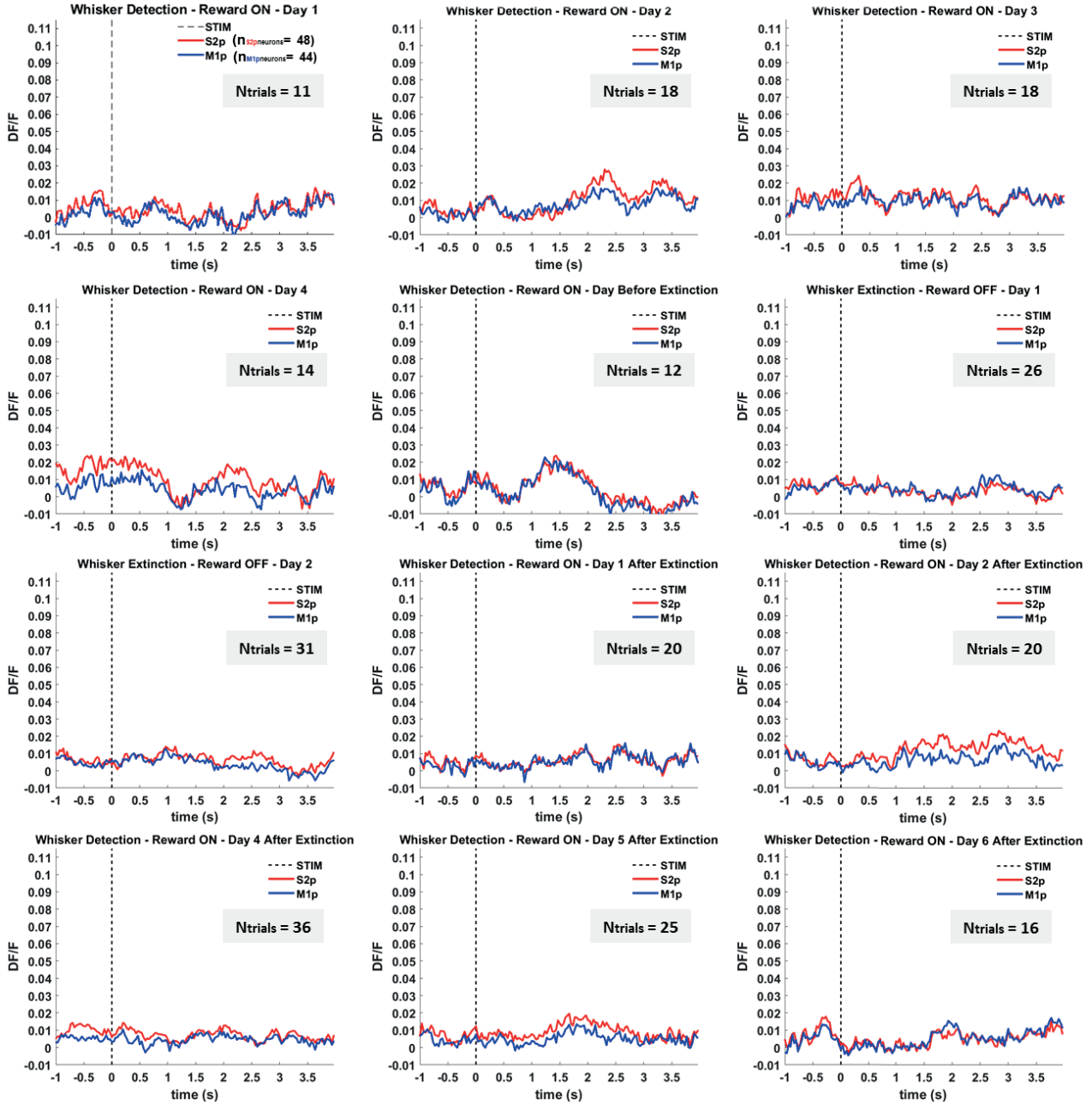


Figure 3.25: Average response of S2p and M1p neurons of L2/3 in wS1 on auditory miss trials over training sessions for an example mouse (AV208). Dashed line indicates stimulation event.

Grand Average - All mice - Auditory miss trials S2p / M1p

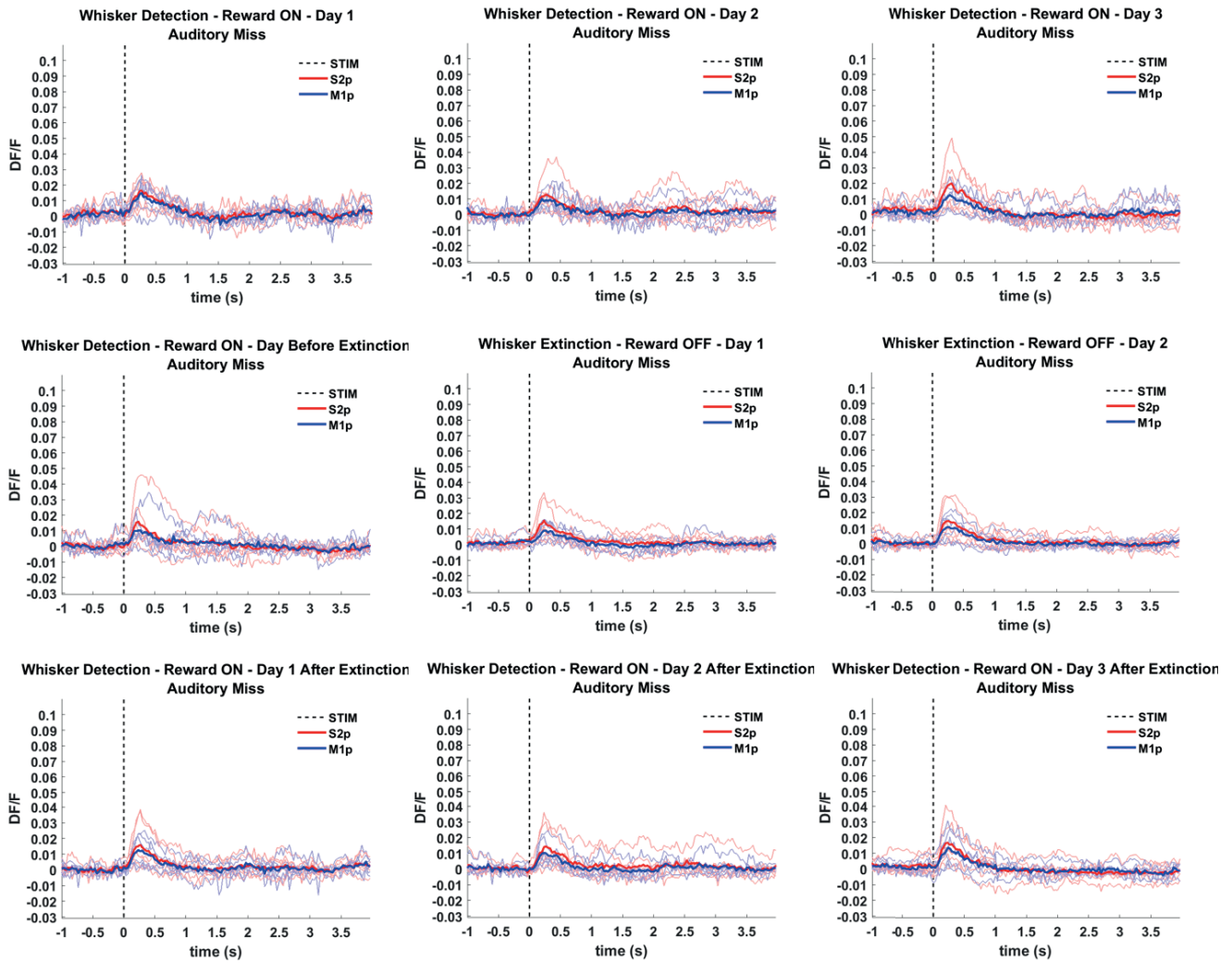


Figure 3.26: Grand average response of S2p and M1p neurons of L2/3 in wS1 on auditory miss trials over training sessions across 6 mice. Dashed line indicates stimulation event. Thick line corresponds to grand average calcium trace across mice, thin line corresponds to average calcium trace for a single mouse.

All mice – Whisker hit –Day 2 - S2p / M1p

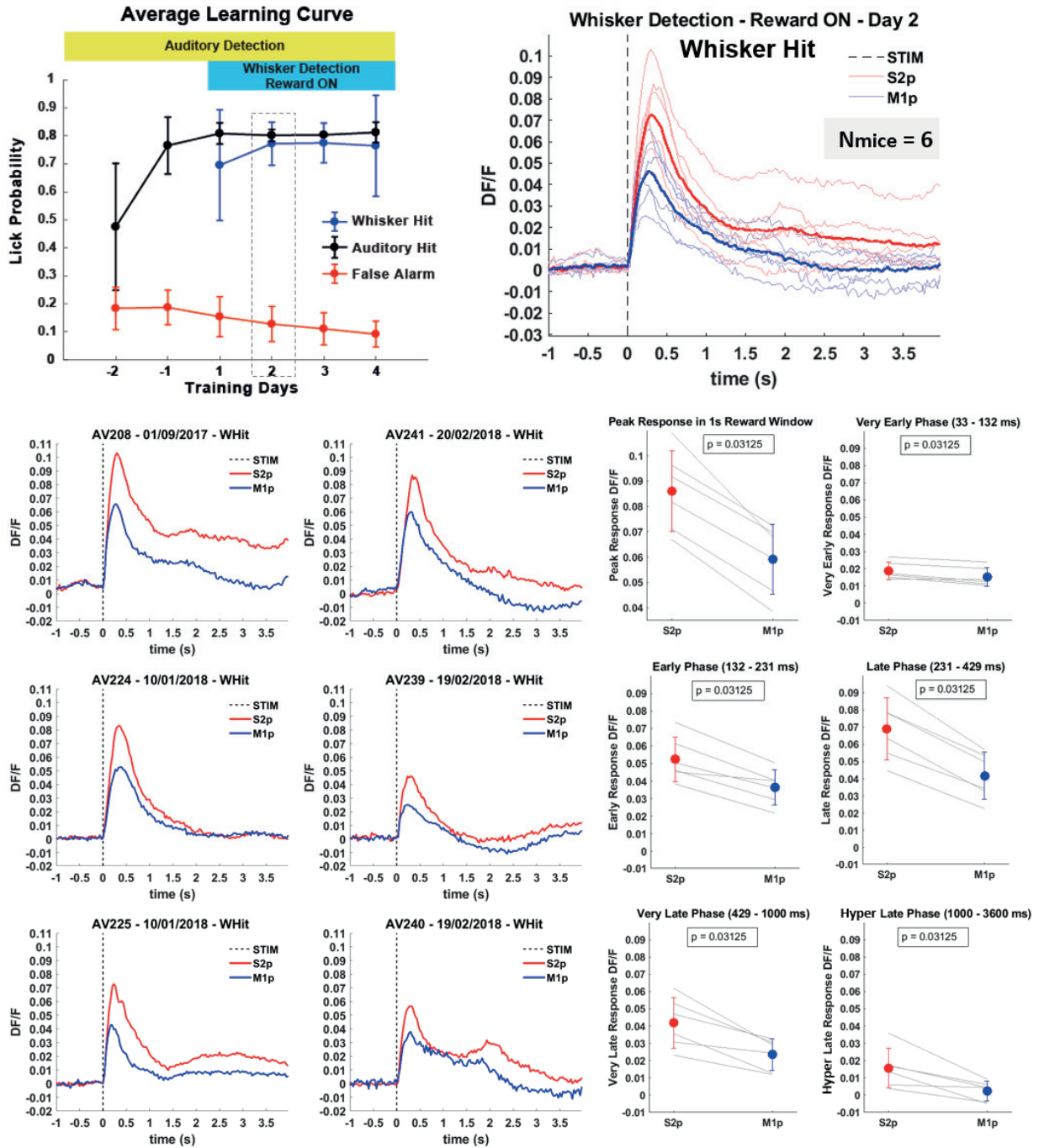


Figure 3.27: Average responses across 6 mice of S2p and M1p neurons of L2/3 in wS1 on a single training session (Day 2 of whisker detection) for whisker hit trials (WHit). Average learning curve indicates the selected training session. Overlaid single mice average traces (thin lines demonstrate individual mice average responses for S2p in re and M1p in blue, thick lines demonstrates the grand average response across mice, dashed line indicates stimulation event). Quantification of the different phases: very early (33-132 ms), early (132-231 ms), late (231-429 ms), very late (429-1000 ms), and hyper late (1000-3600 ms). Wilcoxon signed-rank paired test.

Whisker Detection - Reward ON - Day 2 - Whisker Hit - STIM Triggered Analysis

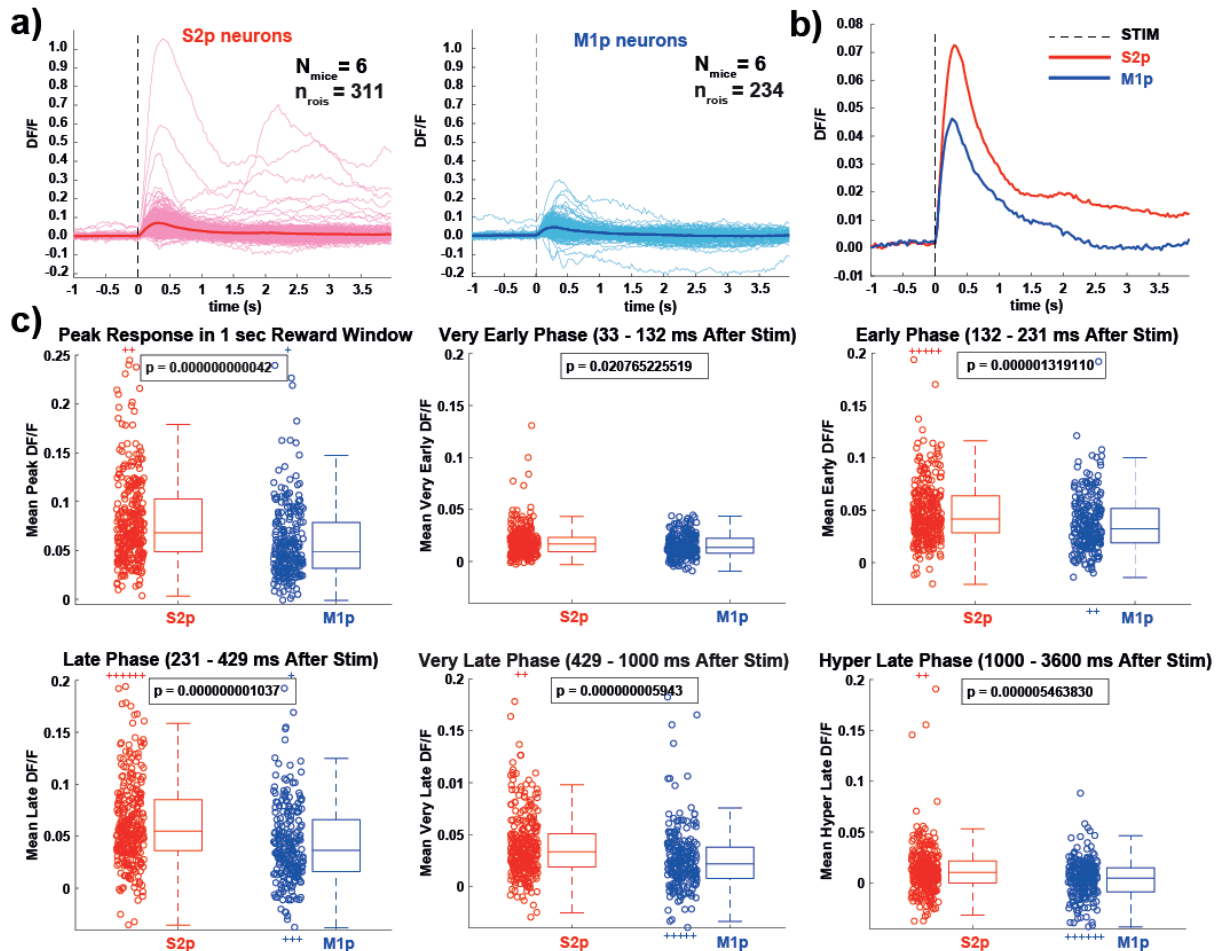


Figure 3.28: Single neurons analysis for S2p and M1p neurons of L2/3 in wS1 across 6 mice on a single training session (Day 2 of whisker detection) for whisker hit trials. a) Overlaid average response traces of single S2p and M1p neurons. Thick line corresponds to grand average across all neurons. b) Overlaid grand average response of S2p and M1p neurons. c) Quantification of mean peak response within 1 sec reward window, very early (33-132 ms), early (132-231 ms), late (231-429 ms), very late (429-1000 ms) and hyper late (1000-3600 ms) response after stimulus presentation of single neurons. Dashed line indicates stimulation event. In the box plots, the central line indicates the median, and the bottom and top edges of the box indicate the 25th and 75th percentiles, respectively. The whiskers show the most extreme data points not including outliers, and the outliers are indicated using the '+' symbol. Open circles represent individual neurons. Wilcoxon rank-sum unpaired test was used for statistical comparisons.

Whisker Hit - Over Sessions - S2p / M1p

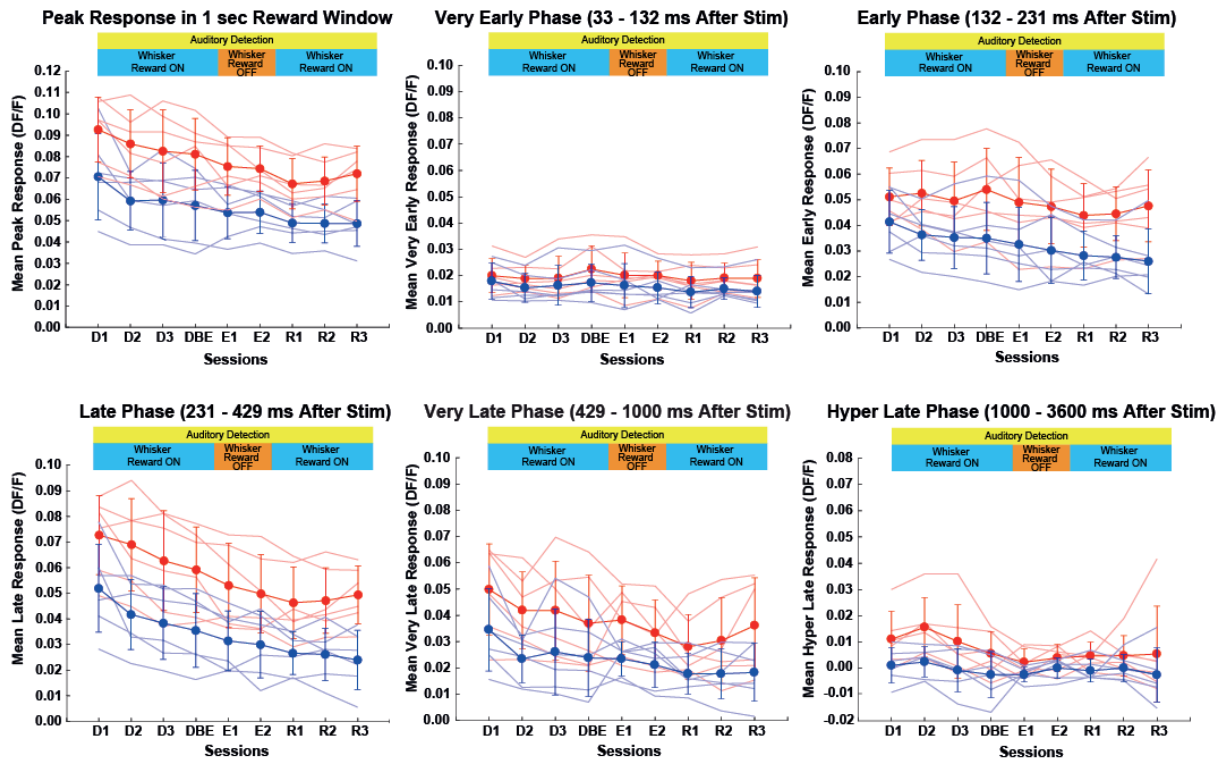


Figure 3.29: Longitudinal observation of mean peak (in 1 sec reward window), very early (33-132 ms), early (132-231 ms), late (231-429 ms), very late (429-1000 ms) and hyper late (1000-3600 ms) response after stimulus presentation across 6 mice for whisker hit/whisker false lick trials in S2p and M1p neurons.

Grand Average - All mice – False Alarm - Lick Triggered - S2p / M1p

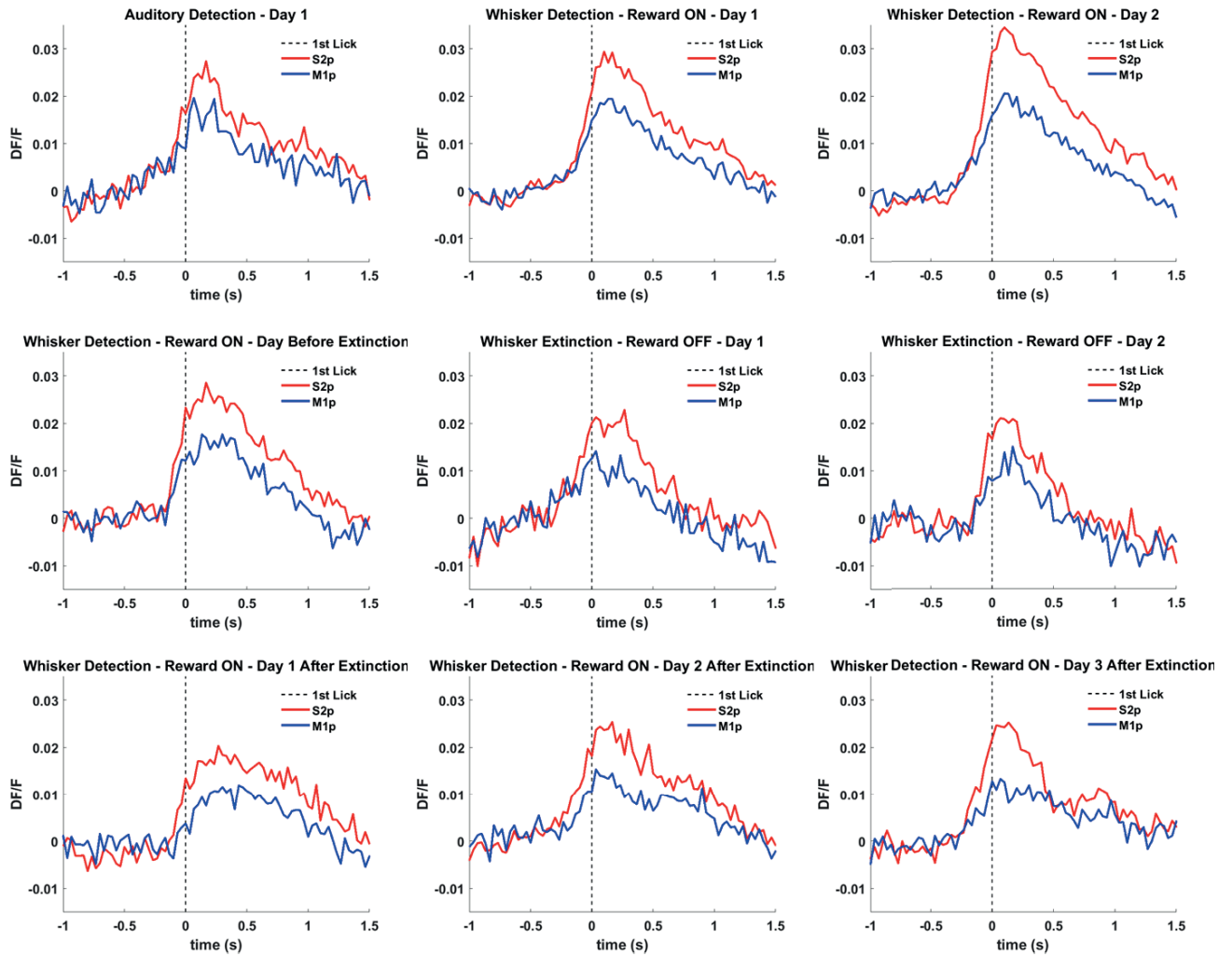


Figure 3.30: Lick triggered analysis: Grand average response of S2p and M1p neurons of L2/3 in wS1 on false alarm trials over training sessions across 6 mice. Dashed line indicates 1st lick event.

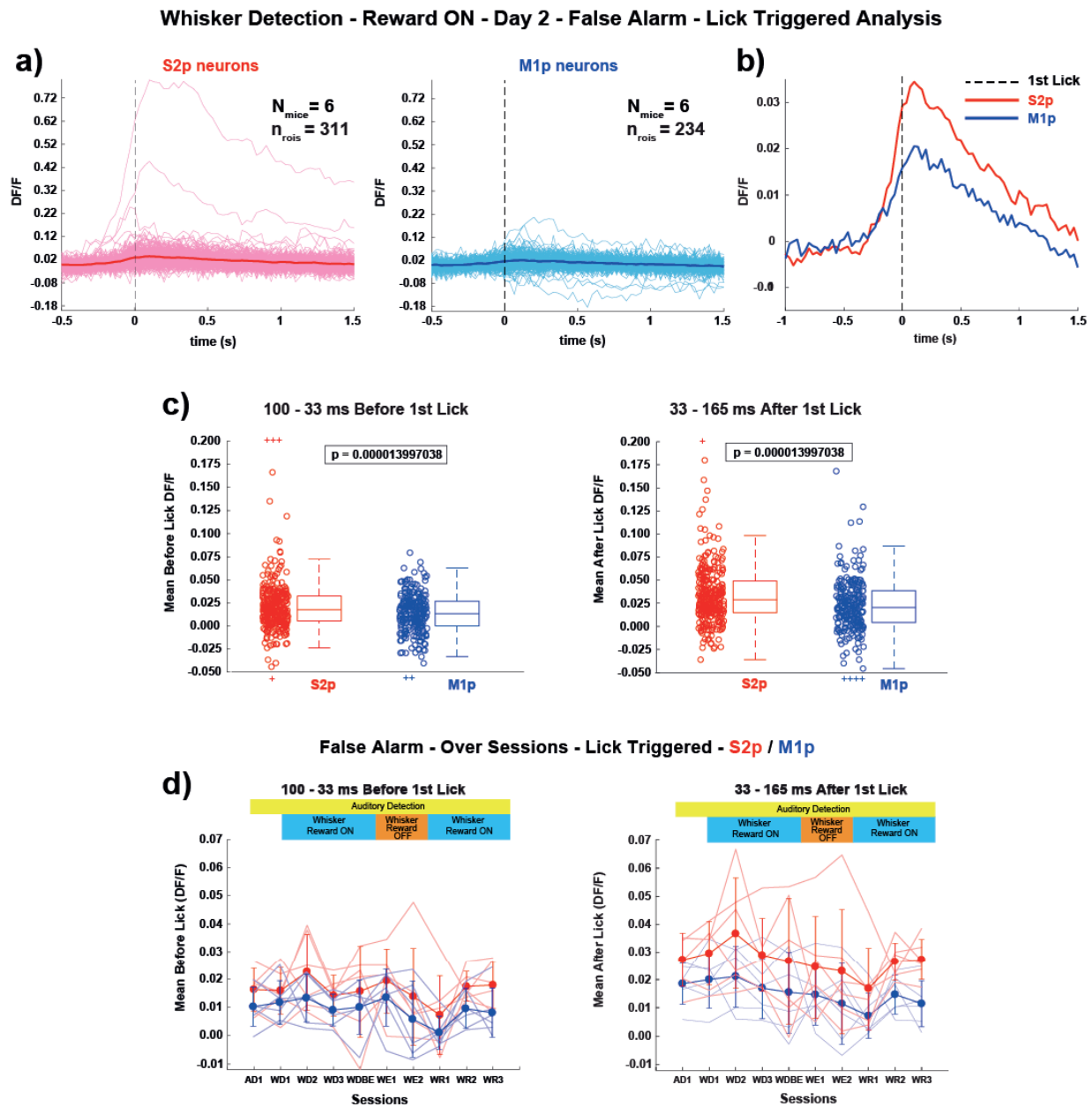


Figure 3.31: Single neurons analysis for S2p and M1p neurons of L2/3 in wS1 across 6 mice on a single training session (Day 2 of whisker detection) for false alarm trials. a) Overlaid average response traces of single S2p and M1p neurons. Thick line corresponds to grand average across all neurons. b) Overlaid grand average response of S2p and M1p neurons. c) Quantification of mean response before (100-33 ms) and after (33-165 ms) the 1st lick of single neurons. d) Longitudinal observation of mean response before and after the 1st lick of S2p and M1p neurons. Dashed line indicates the 1st lick event. In the box plots, the central line indicates the median, and the bottom and top edges of the box indicate the 25th and 75th percentiles, respectively. The whiskers show the most extreme data points not including outliers, and the outliers are indicated using the '+' symbol. Open circles represent individual neurons. Wilcoxon rank-sum unpaired test was used for statistical comparisons.

1.8 Discussion

In summary, I studied cortico-cortical dynamics in primary whisker S1 of mice during learning of a whisker and auditory detection task. At first mice were trained only in auditory stimulus detection. After mice reached good performance on the auditory detection, whisker stimuli were introduced in randomly interleaved trials. Licking in response to whisker stimuli was also rewarded, and mice rapidly learned to lick on both whisker and auditory trials. As soon as mice became experts in the detection of both sensory modalities, they underwent two days of reward extinction on whisker trials, in which mice learned to withhold licking in response to whisker stimulation. Finally, reward was reinstated in whisker trials, and most mice learned relatively quickly to lick after whisker stimulation. I used transgenic mice expressing GCaMP6f in L2/3 neurons combined with two-photon microscopy and retrograde labeling techniques, to chronically monitored the activity of excitatory layer 2/3 neurons in S1 projecting to M1p or S2p, while mice learned the behavioral task.

Chronic calcium imaging analysis demonstrated that L2/3 neuronal populations in S1 responded to both whisker and auditory stimulation, with whisker stimulus evoked responses been stronger and faster than for auditory stimulation. L2/3 neuronal responses in S1 correlated with task performance, and those responses remained relatively stable across most training sessions and under different reward conditions. Both S2p and M1p neurons exhibited smaller responses in amplitude compared to the whole L2/3 neuronal population, but similarly, responded to both whisker and auditory stimulation, with whisker stimulus evoked responses been stronger and faster than in auditory stimulation, while remaining stable across most training sessions and under different reward conditions.

When I compared S2p and M1p neurons in different trial types (whisker hit, whisker miss, auditory hit, auditory miss), a stronger response was evoked in S2p than M1p neurons that was correlated with task performance, and remained relatively stable across most training sessions and under different reward conditions. In particular, responses of S2p neurons in whisker hit trials were stronger than M1p neurons, and their difference remained relatively higher across all sessions and reward conditions. Calcium signals in whisker miss trials were slightly larger in S2p than M1p neurons, and this difference remained relatively stable across sessions. Likewise, in auditory hit trials, S2p responses were larger than M1p, and this difference remained stable across all training

sessions. However, in auditory miss trials there was no difference between S2p and M1p responses across all sessions and reward conditions.

When I investigated calcium responses in different phases during trial (very early, early, late, very late, and hyper late), S2p neurons displayed a larger response in all different phases than M1p neurons, as well as a higher mean peak response. The smallest difference observed in the very early phase (33 -132 ms), and the largest differences observed in the late (231-429 ms) and very late (429 - 1000 ms) phase after whisker deflection. In single neurons analysis, although both S2p and M1p neurons displayed a diversity of sensory evoked responses, on average these responses were higher in S2p neurons than M1p for all the different phases after whisker stimulation. S2p evoked responses remained higher than M1p response across all training sessions, but both displayed a progressive reduction in their peak responses as well as in late and very late phases. Furthermore, both S2p and M1p neurons responded during spontaneous licking, but the S2p neuronal response was larger than that for M1p neurons across sessions. Although both S2p and M1p neuronal responses were diverse during spontaneous licking, on average these responses were higher in S2p neurons than M1p and remained higher and relatively stable across sessions.

Prior experimental studies (Sato & Svoboda, 2010; Chen et al., 2013; Yamashita et al., 2013; Chen et al., 2015; Clancy et al., 2015; Yang et al., 2016; Yamashita & Petersen, 2016; Chen et al., 2016) investigated in vivo responses of S1 neurons that project to either S2 or M1 and have shown that these neurons have distinct intrinsic and task-related response properties. My results are in good agreement with a previous study, in which electrophysiological recordings were performed in S2p and M1p neurons of S1 during a whisker detection task in expert as well as in naïve mice (Yamashita & Petersen, 2016). In this study, whisker stimulation in expert mice, evoked the strongest response in S2p neurons correlated with task performance. In addition, the largest difference in activity during task performance between S2p and M1p neurons was observed during the lick period, which was 250-1000 ms upon whisker stimulation. These results are consistent with my findings, in which the strongest response was observed in S2p neurons and the largest difference between S2p and M1p responses displayed during the late (231-429 ms) and very late (429 - 1000 ms) phase after whisker deflection. However, in this electrophysiological study, whisker stimulation in naïve mice evoked the strongest response in M1p neurons correlated with task performance. Thus, task learning induced choice-related responses specifically in S2p neurons. This contrasts with my

results, in which whisker stimulation evoked stronger responses in S2p neurons from the very first day of whisker detection. Furthermore, in the electrophysiological study (Yamashita & Petersen, 2016), task learning induced enhanced activity during spontaneous licking only in S2p neurons. In contrast, in my results I found that spontaneous licking evoked responses in both S2p and M1p neurons, with S2p neurons exhibiting stronger responses across all training sessions. In another study, S2p and M1p neurons in S1 were monitored during the execution of a texture discrimination task, and has shown that S2p neurons encode the different textures more accurately, as well as exhibit stronger choice-related responses compared to M1p neurons (Chen et al., 2013). Learning of this task induced choice-related activity only in S2p neurons (Chen et al., 2015). I speculate that in my results, I did not observe task learning induced responses in S2p neurons, because in my task mice were exposed to an auditory detection task prior to the presentation of whisker detection in the behavioral paradigm. Therefore, mice were already engaged to a stimulus-reward association task, and they could rapidly learn the newly presented whisker-reward association within one session. The reason why I introduced the phase of only auditory stimulus detection prior to the introduction of the whisker detection, was that I wanted to establish a baseline licking behavior in mice, in order to exclusively focus my study on the whisker stimulus learning-related changes in S1 while excluding possible general effects of learning to lick in the reward spout. In addition, I was were interested to examine, how a second sensory modality is processed in S1, and how stable this is during learning.

Choice-related responses of S2p neurons in S1 that are acquired during learning might be inherited by a feedback pathway from S2 (Chen et al., 2016; Kwon et al., 2016; Yang et al., 2016). Imaging experiments in both S1 and S2 have shown that S1 encoded whisker stimulus better than S2, while S2 encoded better perceptual choice. Furthermore, imaging of S2 axons in S1 in mice performing a whisker detection task have demonstrated that choice-related information propagates from S2 to S1 enhancing choice-related responses in S1 (Kwon et al., 2016).

In the present study, I focused the analysis only on 6 out of 19 recorded animals, due to time limitation reasons. Future work should concentrate on the analysis of the first day of whisker stimulus detection on a trial-by-trial basis, in order to investigate possible learning-related changes that gradually develop over time in S2p and M1p neurons. Further investigation can be done on lick-triggered analysis of catch trials on the first phase of training, in which there is only auditory stimulus detection, on a day-by-day analysis

across sessions, as well as trial-by-trial analysis on the first auditory detection session. In my experiments, I used high-speed videography throughout training to film whisker position during task learning. Thus, analysis of these data will help us to investigate the influence of whisking behavior on neuronal activity during task learning. Finally, another part of the dataset that is interesting to be analysed is the calcium imaging recordings during psychophysical measurements, in which mice were trained for 2 to 3 sessions in three different whisker stimulus intensities. Hence, further work on the psychophysical measurements combined with neurometric analysis will help us to understand the impact of whisker stimulus intensity in neuronal responses of projection neurons in S1 during the execution of the detection task.

In future research, optogenetic inactivation of S1 during the whisker and auditory task is important to be conducted in order to examine the causal role of S1 in the execution of the task across the different reward conditions. In addition, it will be interesting to investigate specifically the causal roles of S2p neurons in S1 during the execution of the task. A recent anatomical study of long-range axonal projections of layer 2/3 neurons in S1, has shown that these neurons not only project to M1 and S2 areas, but also the dysgranular zone surrounding S1, perirhinal temporal association cortex, and striatum (Yamashita et al., 2018). Therefore, future experiments could investigate responses of L2/3 neurons in S1 projecting to perirhinal temporal association cortex or striatum during sensorimotor learning. Furthermore, an interesting future work could be the implementation of a modified version of the whisker and auditory detection task, in which after the initial auditory detection phase, mice can be introduced to whisker stimulation non-rewarded trials, and as soon as they learn to withhold licking in response to whisker stimulation, to start rewarding the whisker stimulus trials again. One can turn on and off reward multiple times, and study the effect of reward-based learning during these alterations.

An important limitation of the current study is that CTB might hinder GCaMP6f signals. This might explain the observation that calcium responses of the whole population of neurons were stronger compared to CTB labeled neurons. A control experiment to investigate this could be the *post-hoc* labeling of L2/3 neurons in S1 with CTB and the identification of the recorded neurons. Because two-photon microscopes have an elongated point spread function along the z-axis, the signals imaged in a given focal plane are contaminated by signals from above and below this plane. The fluorescence signal from a given ROI is thus usually contaminated by signals from surrounding neurites (axons and dendrites)

as well as nearby neuronal somata. Correcting for such out-of-focus contamination is particularly critical for calcium imaging experiments. In the current analysis, correction for neuropil contamination was not performed, thus it is an important step to be implanted in future analysis using available algorithms (Keemink et al., 2018; Dipoppa et al., 2018). In head-fixed mice, licking to obtain water reward produces stereotyped brain motion that might interfere with two-photon calcium imaging of neuronal activity. In the current analysis, movement-related artifacts were corrected *post-hoc* in the x-y plane for the acquired data. When movement was slow relative to the frame acquisition rate (~30 Hz), the image registration used in this analysis was sufficient to correct for lateral shifts. When faster movements occurred during frame scanning, more sophisticated algorithms are needed to correct for within-frame distortions (line-by-line motion correction, Dombek et al., 2007). However, motion correction along the z-axis is a more complex problem, thus it was not performed in this study. One possible future solution on this is the fast 3-D scanning using a piezoelectric focusing element (Andermann et al., 2010) or acousto-optic lenses (Katona et al., 2012). Another possible solution is the online optical correction of z-axis brain motion during two-photon imaging using refocusing with an electrically tunable lens (Chen et al., 2013). There are thus further investigations that need to be done in order to understand the functional differences between S2- and M1-projection neurons in L2/3 of S1.

Chapter 4

Conclusions

In this thesis, I studied the structure and function of a specific subset of cortico-cortical long-range projection neurons in mouse primary somatosensory whisker barrel cortex (S1).

In the first part of my thesis, I studied the projections of L2/3 neurons in S1 using transgenic mice and viral injections targeted to the center of C2 barrel column. Long-range axonal projections were found in cortex and striatum, but not in other subcortical brain areas. In particular, I found that L2/3 neurons in S1 densely projected to secondary whisker somatosensory cortex (S2) and primary/secondary whisker motor cortex (M1/2), in agreement with previous studies, (Miller et al., 2001; Hoffer et al., 2003, 2005; Aronoff et al., 2010; Zakiewicz et al., 2011). Lower density of axons was found in perirhinal temporal association cortex and striatum. In addition, another region in which axons were found is the PP, which is most likely part of the secondary visual cortex where visual and somatosensory information are integrated (Wang and Burkhalter, 2007; Wang et al., 2012; Olcese et al., 2013). Furthermore, axonal spots were observed in the dysgranular zone surrounding S1, consistent with previous research (Broser et al., 2008). Finally, sparse axonal projections were found in contralateral somatosensory cortex. However, further work is required to study in depth the structure of L2/3 projections. Future experiments must determine whether L2/3 projection neurons can be unambiguously divided into different classes and if so how many. Many neurons projected to multiple distant targets, and in future work it will be important to investigate the function of neurons with known axonal arborisations.

In the second part of my thesis, I studied the function of L2/3 neurons in S1 that project to either S2 or M1, which appeared to be two major and largely non-overlapping groups of S1 projection neurons. Only a few previous studies have investigated what the two pathways encode and their activity during learning of a sensorimotor task. (Sato and Svoboda, 2010; Chen et al., 2013, 2015; Yamashita et al., 2013; Kwon et al., 2016; Yamashita and Petersen, 2016). I found that stimulus-evoked responses were larger in neurons projecting to S2 compared to those projecting to M1. Signaling from S1 to S2 may therefore be more important for task performance compared to signaling from S1 to M1. Consistent with such a hypothesis, inactivation of either S1 or S2, but not M1, hinders performance in a closely-related whisker detection task (Le Merre et al., 2018). Interestingly, the responses of neurons in L2/3 of S1 appeared to be relatively little affected by reward contingencies. Neuronal activity in S1 therefore does not appear to strongly encode the value of the sensory stimulus, whereas this might be more strongly represented in higher brain areas such as mPFC and dCA1 (Le Merre et al., 2018). Future experiments should investigate other types of neurons in S1, which might be differently regulated across learning, and it will also be interesting to image neuronal activity in other brain areas.

In conclusion, this thesis contributes to our knowledge about the structure and function of specific types of cortical projection neurons in S1, helping to better understand how specific sensory information is routed to downstream areas for further processing during goal-directed behaviour and sensorimotor learning.

References

- Adesnik, H., and Scanziani, M. (2010). Lateral competition for cortical space by layer-specific horizontal circuits. *Nature* 464, 1155-1160. doi:10.1038/nature08935.
- Akemann, W., Léger, J.F., Ventalon, C., Mathieu, B., Dieudonné, S., and Bourdieu, L. (2015). Fast spatial beam shaping by acousto-optic diffraction for 3D non-linear microscopy. *Optics express* 23, 28191-28205. doi: /10.1364/OE.23.028191
- Akerboom, J., Rivera, J.D., Guilbe, M.M., Malave, E.C., Hernandez, H.H., Tian, L., Hires, S.A., Marvin, J.S., Looger, L.L., Schreier, E.R. (2009). Crystal structures of the GCaMP calcium sensor reveal the mechanism of fluorescence signal change and aid rational design. *J Biol Chem* 284, 6455-6464. doi: 10.1074/jbc.M807657200
- Akerboom, J., Chen, T. W., Wardill, T. J., Tian, L., Marvin, J. S., Mutlu, S., et al. (2012). Optimization of a GCaMP calcium indicator for neural activity imaging. *J. Neurosci.* 32, 13819-13840. doi: 10.1523/JNEUROSCI.2601-12.2012
- Akerboom, J., Carreras Calderon, N., Tian, L., Wabnig, S., et al. (2013). Genetically encoded calcium indicators for multi-color neural activity imaging and combination with optogenetics. *Frontiers in Molecular Neuroscience* 6:2. doi: 10.3389/fnmol.2013.00002
- Akram, M. A., Nanda, S., Maraver, P., Armananzas, R., and Ascoli, G. A. (2018). An open repository for single-cell reconstructions of the brain forest. *Sci. Data* 5:180006. doi: 10.1038/sdata.2018.6
- Alloway, K.D. (2007). Information Processing Streams in Rodent Barrel Cortex: The Differential Functions of Barrel and Septal Circuits. *Cereb. Cortex* 18, 979-989. doi: 10.1093/cercor/bhm138
- Andermann, M.L., and Moore, C.I. (2006). A somatotopic map of vibrissa motion direction within a barrel column. *Nat. Neurosci.* 9, 543-551. doi: 10.1038/nn1671

Andermann, M.L. (2010). Chronic cellular imaging of mouse visual cortex during operant behavior and passive viewing. *Frontiers of Cellular Neuroscience*. doi: 10.3389/fncel.2010.00003

Andermann, M. L., Kerlin, A. M., Roumis, D. K., Glickfeld, L. L., and Reid, R. C. (2011). Functional specialization of mouse higher visual cortical areas. *Neuron* 72, 1025–1039. doi: 10.1016/j.neuron.2011.11.013

Andermann, M.L., Gilfoy, N.B., Goldey, G.J., Sachdev, R.N., Wölfel, M., McCormick, D.A., Reid, R.C., Levene, M.J. (2013). Chronic cellular imaging of entire cortical columns in awake mice using microprisms. *Neuron* 80, 900–913. doi: 10.1016/j.neuron.2013.07.052

Aronoff, R., Matyas, F., Mateo, C., Ciron, C., Schneider, B., and Petersen, C. C. H. (2010). Long-range connectivity of mouse primary somatosensory barrel cortex. *Eur. J. Neurosci.* 31, 2221–2233. doi: 10.1111/j.1460-9568.2010.07264.x

Barth, A.L., and Poulet, J.F.A. (2012). Experimental evidence for sparse firing in the neocortex. *Trends Neurosci.* 35, 345–355. doi: 10.1016/j.tins.2012.03.008

Bosman, L.W.J., Houweling, A.R., Owens, C.B., Tanke, N., Shevchouk, O.T., Rahmati, N., Teunissen, W.H.T., Ju, C., Gong, W., Koekkoek, S.K.E. (2011). Anatomical Pathways Involved in Generating and Sensing Rhythmic Whisker Movements. *Front. Integr. Neurosci.* 5. doi: 10.3389/fnint.2011.00053

Brecht, M., Roth, A., and Sakmann, B. (2003). Dynamic receptive fields of reconstructed pyramidal cells in layers 3 and 2 of rat somatosensory barrel cortex. *J. Physiol.* 553, 243–226. doi: 10.1113/jphysiol.2003.044222

Broser, P., Grinevich, V., Osten, P., Sakmann, B., and Wallace, D. J. (2008). Critical period plasticity of axonal arbors of layer 2/3 pyramidal neurons in rat somatosensory cortex: layer-specific reduction of projections into deprived cortical columns. *Cereb. Cortex.* 18, 1588–1603. doi: 10.1093/cercor/bhm189

Bruno, R. M., Hahn, T. T., Wallace, D. J., de Kock, C. P., and Sakmann, B. (2009). Sensory experience alters specific branches of individual corticocortical axons during development. *J. Neurosci.* 29, 3172–3181. doi: 10.1523/JNEUROSCI.5911-08.2009

- Butts, D.A, Weng, C, Jin, J. (2007). Temporal precision in the neural code and the time-scales of natural vision. *Nature* 449, 92-95. doi:10.1038/nature06105
- Buzsaki, G. (2010) Neural syntax: cell assemblies, synapsesembles, and readers. *Neuron*, 68, 362-385. doi: 10.1016/j.neuron.2010.09.023.
- Cadwell, C. R., Palasantza, A., Jiang, X., Berens, P., Deng, Q., Yilmaz, M., et al. (2016). Electrophysiological, transcriptomic and morphologic profiling of single neurons using Patch-seq. *Nat. Biotechnol.* 34, 199–203. doi: 10.1038/nbt.3445
- Cetin, A., Komai, S., Eliava, M., Seeburg, P.H., and Osten, P. (2006). Stereotaxic gene delivery in the rodent brain. *Nat. Protoc.* 1, 31663173. doi:10.1038/nprot.2006.450
- Chapin, J. K., Sadeg, M., and Guise, J. L. (1987). Corticocortical connections within the primary somatosensory cortex of the rat. *J. Comp. Neurol.* 263, 326–346. doi: 10.1002/cne.902630303
- Chen, J. L., Carta, S., Soldado-Magraner, J., Schneider, B. L., and Helmchen, F. (2013). Behaviour-dependent recruitment of long-range projection neurons in somatosensory cortex. *Nature* 499, 336–340. doi: 10.1038/nature12236
- Chen, J.L., Andermann, M.L., Keck, T., Xu, N., Ziv, Y. (2013b). Imaging Neuronal Populations in Behaving Rodents: Paradigms for Studying Neural Circuits Underlying Behavior in the Mammalian Cortex. *Journal of Neuroscience* 33, 17631-17640. doi: 10.1523/JNEUROSCI.3255-13.2013
- Chen, J.L., Pfaffli, O.A., Voigt, F.F., Margolis, D.J., and Helmchen, F. (2013b). Online correction of licking-induced brain motion during two-photon imaging with a tunable lens. *J. Physiol.* 591, 4689-4698. doi: 10.1113/jphysiol.2013.259804
- Chen, T. W., Wardill, T. J., Sun, Y., Pulver, S. R., Renninger, S. L., Baohan, A., Svo-boda, K. et al. (2013). Ultrasensitive fluorescent proteins for imaging neural activity. *Nature* 499, 295-300. doi: 10.1038/nature12354
- Chen, J. L., Margolis, D. J., Stankov, A., Sumanovski, L. T., Schneider, B. L., and Helmchen, F. (2015). Pathway-specific reorganization of projection neurons in somatosensory cortex during learning. *Nat. Neurosci.* 18, 1101-1108. doi: 10.1038/nn.4046
- Chen, J.L., Voigt, F.F., Javadzadeh, M., Krueppel, R., Helmchen, F. (2016). Long-range

population dynamics of anatomically defined neocortical networks. *Elife* 5, e14679. doi: 10.7554/eLife.14679

Clancy, K.B., Schnepel, P., Rao, A.T., Feldman, D.E. (2015). Structure of a single whisker representation in layer 2 of mouse somatosensory cortex. *J. Neurosci.* 35, 3946-3958. doi: 10.1523/JNEUROSCI.3887-14.2015

Collot, M., Loukou, C., Yakovlev, A.V., Wilms, C.D., Li, D., Evrard, A., Zamaleeva, A., Bourdieu, L., et al., (2012). Calcium rubies: a family of red-emitting functionalizable indicators suitable for two-photon Ca^{2+} imaging. *Journal of the American Chemical Society* 134, 14923-14931. doi: 10.1021/ja304018d

Crochet, S., Poulet, J.F.A., Kremer, Y., and Petersen, C.C.H. (2011). Synaptic Mechanisms Underlying Sparse Coding of Active Touch. *Neuron* 69, 1160-1175. doi: 10.1016/j.neuron.2011.02.022

DeFelipe J. (2011), The evolution of the brain, the human nature of cortical circuits, and intellectual creativity. *Frontiers in Neuroanatomy* 5, 1-17. doi: 10.3389/fnana.2011.00029

Daigle, T. L., Madisen, L., Hage, T. A., Zeng, H., et al. (2018). A suite of transgenic driver and reporter mouse lines with enhanced brain-cell-type targeting and functionality. *Cell* 174, 465-480. doi: 10.1016/j.cell.2018.06.035

Dana, H., Mohar, B., Sun, Y., et al. (2016). Sensitive red protein calcium indicators for imaging neural activity. *eLife* 5, e12727. doi:10.7554/eLife.12727

Denk, W., Strickler, J. H., Webb, W. W. (1990). Two-photon laser scanning microscopy. *Science* 248, 73-76. doi: 10.1126/science.2321027

Deschênes, M., Veinante, P., and Zhang, Z. W. (1998). The organization of corticothalamic projections, reciprocity versus parity. *Brain Res. Brain Res. Rev.* 28, 286-308. doi: 10.1016/S0165-0173(98)00017-4

Deschenes, M., Urbain, N. (2009), Vibrissal afferents from trigeminus to cortices. *Scholarpedia*, 4(5):7454. doi:10.4249/scholarpedia.7454

Diamond, M. E., von Heimendahl, M., Knutsen, P. M., Kleinfeld, D., and Ahissar, E. (2008). 'Where' and 'what' in the whisker sensorimotor system. *Nat. Rev. Neurosci.* 9,

601–612. doi: 10.1038/nrn2411

Dipoppa, M., Ranson, A., Krumin, M., Pachitariu, M., Carandini, M., Harris, K.D. (2018). Vision and Locomotion Shape the Interactions between Neuron Types in Mouse Visual Cortex. *Neuron* 98, 602-615. doi.org/10.1016/j.neuron.2018.03.037

Dombeck, D. A., Khabbazi, A. N., Collman, F., Adelman, T. L. & Tank D. W. (2007). Imaging large-scale neural activity with cellular resolution in awake, mobile mice. *Neuron* 56, 43-57. doi: 10.1016/j.neuron.2007.08.003

Dombeck, D. A., Graziano, M. S., Tank, D. W. (2009). Functional clustering of neurons in motor cortex determined by cellular resolution imaging in awake behaving mice. *J. Neurosci.* 29, 13751-13760. doi: 10.1523/JNEUROSCI.2985-09.2009.

Douglas, R. J., Martin, K. A. C. (2007), Mapping the Matrix: The Ways of Neocortex. *Neuron* 56, 226-238. doi: 10.1016/j.neuron.2007.10.017

Economo, M. N., Clack, N. G., Lavis, L. D., Gerfen, C. R., Svoboda, K., Myers, E. W., et al. (2016). A platform for brain-wide imaging and reconstruction of individual neurons. *Elife* 5:e10566. doi: 10.7554/eLife.10566

Erzurumlu, R., Murakami, Y., Rijli, F. M. (2010). Mapping the face in the somatosensory brain- stem. *Nature Reviews Neuroscience* 11, 252-263. doi: 10.1038/nrn2804.

Estebanez, L., Bertherat, J., Shulz, D.E., Bourdieu, L., Léger, J.F. (2016). A radial map of multi-whisker correlation selectivity in the rat barrel cortex. *Nat Commun.* 7, 13528. doi: 10.1038/ncomms13528

Fabri, M., and Burton, H. (1991). Ipsilateral cortical connections of primary somatic sensory cortex in rats. *J. Comp. Neurol.* 311, 405–424. doi: 10.1002/cne.903110310

Feldmeyer, D., Lübke, J., and Sakmann, B. (2006). Efficacy and connectivity of intracolumnar pairs of layer 2/3 pyramidal cells in the barrel cortex of juvenile rats. *J. Physiol.* 575, 583–602. doi: 10.1113/jphysiol.2006.105106

Feldmeyer, D. (2012). Excitatory neuronal connectivity in the barrel cortex. *Front. Neuroanat.* 6. doi: 10.3389/fnana.2012.00024

Feldmeyer, D., Brecht, M., Helmchen, F., Petersen, C. C. H., Poulet, J. F. A., Staiger, J.

F., et al. (2013). Barrel cortex function. *Prog. Neurobiol.* 103, 3–27. doi: 10.1016/j.pneurobio.2012.11.002

Ferezou, I., Haiss, F., Gentet, L. J., Aronoff, R., Weber, B., and Petersen, C. C. H. (2007). Spatiotemporal dynamics of cortical sensorimotor integration in behaving mice. *Neuron* 56, 907–923. doi: 10.1016/j.neuron.2007.10.007

Fries, P. (2015) Rhythms for cognition: communication through coherence. *Neuron*, 88, 220–235. doi: 10.1016/j.neuron.2015.09.034

Frostig, R.D. (2009). *In Vivo Optical Imaging of Brain Function*. 2nd Edition. Frontiers in neuro- science, CRC Press.

Fuzik, J., Zeisel, A., Máté, Z., Calvigioni, D., Yanagawa, Y., Szabó, G., et al. (2016). Integration of electrophysiological recordings with single-cell RNA-seq data identifies neuronal subtypes. *Nat. Biotechnol.* 34, 175–183. doi: 10.1038/nbt.3443

Gdalyahu, A., Tring, E., Polack, P.O., Gruver, R., Golshani, P., Faselow, M.S., Silva, A.J., Trachtenberg, J.T. (2012). Associative fear learning enhances sparse network coding in primary sensory cortex. *Neuron* 75,121-132. doi: 10.1016/j.neuron.2012.04.035

Gentet, L.J., Avermann, M., Matyas, F., Staiger, J.F., and Petersen, C.C.H. (2010). Membrane Potential Dynamics of GABAergic Neurons in the Barrel Cortex of Behaving Mice. *Neuron* 65, 422-435. doi: 10.1016/j.neuron.2010.01.006

Gerstner, W., Kreiter, A. K., Markram, H. , and Herz, A.V.M. (1997). Neural codes: firing rates and beyond. *Proc. Natl. Acad. Sci.* 94, 12740-12741. doi: 10.1073/pnas.94.24.12740

Glickfeld, L. L., Andermann, M. L., Bonin, V., and Reid, R. C. (2013). Cortico-cortical projections in mouse visual cortex are functionally target specific. *Nat. Neurosci.* 16, 219–226. doi: 10.1038/nn.3300

Gobel, W., Helmchen, F. (2007), *In Vivo Calcium Imaging of Neural Network Function*. *Physiology* 22, 358-365. doi: 10.1152/physiol.00032.2007

Gong, H., Xu, D., Yuan, J., Li, X., Guo, C., Peng, J., et al. (2016). High-throughput dual-colour precision imaging for brain-wide connectome with cytoarchitectonic landmarks at

the cellular level. *Nat. Commun.* 7:12142. doi: 10.1038/ncomms12142

Goldey, G. J., Roumis D. K., Glickfeld, L. L., Kerlin, A. M., Reid, R., C., Bonin V., Schafer D. P., and Andermann, M. L., 2014. Removable cranial windows for long-term imaging in awake mice'. *Nature Protocols*, Vol.9 No. 11, 2515-2538. doi: 10.1038/nprot.2014.165

Greenberg, D. S., Houweling, A. R., Kerr, J. N. (2008). Population imaging of ongoing neuronal activity in the visual cortex of awake rats. *Nature Neuroscience* 11, 749-751. doi: 10.1038/nn.2140

Grewe, B.F., Langer, D., Kasper, H., Kampa, B.M., and Helmchen, F. (2010). High-speed in vivo calcium imaging reveals neuronal network activity with near-millisecond precision. *Nat. Methods* 7, 399-405. doi: 10.1038/nmeth.1453

Grewe, B.F., and Helmchen, F. (2009). Optical probing of neuronal ensemble activity. *Curr. Opin. Neurobiol.* 19, 520-529. doi: 10.1016/j.conb.2009.09.003

Grewe, B.F. and Helmchen, F. (2014). High-speed two-photon calcium imaging of neuronal population activity using acousto-optic deflectors. *Cold Spring Harbor Protocols*, 618-29. doi: 10.1101/pdb.prot081778

Grienberger, C., Konnerth, A. (2012). Imaging Calcium in Neurons. *Neuron* 73, 862-885. doi: 10.1016/j.neuron.2012.02.011

Grinvald, A., Lieke, E., Frostig, R. D., Gilbert, C. D., and Wiesel, T. N. (1986). Functional architecture of cortex revealed by optical imaging of intrinsic signals. *Nature* 324, 361–364. doi: 10.1038/324361a0

Grynkiewicz, G., Poenie, M., Tsien, R.Y. (1985). A new generation of Ca^{2+} indicators with greatly improved fluorescence properties. *J Biol Chem.* 260, 3440-50.

Guizar-Sicairos, M., Thurman, S. T., Fienup, J.R. (2008) "Efficient subpixel image registration algorithms," *Optics Letters* 33, 156-158. doi: 10.1364/OL.33.000156

Guo, Z. V., Li, N., Huber, D., Ophir, E., Gutnisky, D., Ting, J. T., et al. (2014). Flow of cortical activity underlying a tactile decision in mice. *Neuron* 81, 179–194. doi: 10.1016/j.neuron.2013.10.020

- Guo ZV, Li N, Huber D, Ophir E, Gutnisky D, Ting JT, Feng G, Svoboda K. (2014). Flow of cortical activity underlying a tactile decision in mice. *Neuron* 81:179-194. doi: 10.1016/j.neuron.2013.10.020
- Guo, C., Peng, J., Zhang, Y., Li, A., Li, Y., Yuan, J., et al. (2017). Single-axon level morphological analysis of corticofugal projection neurons in mouse barrel field. *Sci. Rep.* 7:2846. doi: 10.1038/s41598-017-03000-8
- Han, Y., Kebschull, J. M., Campbell, R. A. A., Cowan, D., Imhof, F., Zador, A. M., et al. (2018). The logic of single-cell projections from visual cortex. *Nature* 556, 51–56. doi: 10.1038/nature26159
- Harris, J. A., Hirokawa, K. E., Sorensen, S. A., Gu, H., Mills, M., Ng, L. L., et al. (2014). Anatomical characterization of Cre driver mice for neural circuit mapping and manipulation. *Front. Neural Circuits* 8:76. doi: 10.3389/fncir.2014.00076
- Harris, K. D., and Mrsic-Flogel, T. D. (2013). Cortical connectivity and sensory coding. *Nature* 503, 51–58. doi: 10.1038/nature12654
- Harris, K. D., and Shepherd, G. M. G. (2015). The neocortical circuit: themes and variations. *Nat. Neurosci.* 18, 170–181. doi: 10.1038/nn.3917
- Helmchen, F., Denk, W. (2005). Deep tissue two-photon microscopy. *Nat. Methods* 2, 932-940. doi:10.1038/nmeth818
- Heo, C., Park, H., Kim, Y., Baeg, E., Kim, H., Kim, S., Suh, M. (2016). A soft, transparent, freely accessible cranial window for chronic imaging and electrophysiology. *Nature Scientific Reports* 6, 27818. doi:10.1038/srep27818
- Hoffer, Z. S., Arantes, H. B., Roth, R. L., and Alloway, K. D. (2005). Functional circuits mediating sensorimotor integration: quantitative comparisons of projections from rodent barrel cortex to primary motor cortex, neostriatum, superior colliculus, and the pons. *J. Comp. Neurol.* 488, 82–100. doi: 10.1002/cne.20579
- Hoffer, Z. S., Hoover, J. E., and Alloway, K. D. (2003). Sensorimotor corticocortical projections from rat barrel cortex have an anisotropic organization that facilitates integration of inputs from whiskers in the same row. *J. Comp. Neurol.* 466, 525–544. doi: 10.1002/cne.10895

Holtmaat, A., Bonhoeffer, T., Chow, D.K., Chuckowree, J., De Paola, V., Hofer, S.B., Hubener, M., Keck, T., Knott, G., Lee, W.-C.A., et al. (2009). Long-term, high-resolution imaging in the mouse neocortex through a chronic cranial window. *Nat. Protoc.* 4, 1128-1144. doi: 10.1038/nprot.2009.89

Holtmaat, A., de Paola, V., Wilbrecht, L., Trachtenberg, J.T., Svoboda, K., Portera-Cailliau, C. (2012). Imaging neocortical neurons through a chronic cranial window. *Cold Spring Harbor Protocols* 6, 694-701. doi: 10.1101/pdb.prot069617

Holtmaat, A., Caroni, P. (2016). Functional and structural underpinnings of neuronal assembly formation in learning. *Nature Neuroscience* 19, 1553-1562. doi: 10.1038/nn.4418

Hoogland, P. V., Welker, E., and Van der Loos, H. (1987). Organization of the projections from barrel cortex to thalamus in mice studied with Phaseolus vulgaris leucoagglutinin and HRP. *Exp. Brain Res.* 68, 73–87. doi: 10.1007/BF00255235

Hoogland, P. V., Wouterlood, F. G., Welker, E., and Van der Loos, H. (1991). Ultrastructure of giant and small thalamic terminals of cortical origin: a study of the projections from the barrel cortex in mice using Phaseolus vulgaris leuco-agglutinin (PHA-L). *Exp. Brain Res.* 87, 159–172. doi: 10.1007/BF00228517

Houweling, A.R., and Brecht, M. (2007). Behavioural report of single neuron stimulation in somatosensory cortex. *Nature* 451, 65-68. doi:10.1038/nature06447

Hubel, D. H., Wiesel, T. N. (1962). Receptive fields, binocular interaction and functional architecture in the cat's visual cortex. *The journal of physiology* 160 (1), 106154.

Huber, D., Gutnisky, D. A., Peron, S., O'Connor, D. H., Wiegert, J.S., Tian, L., Oertner, T. G., Looger, L., Svoboda, K. (2012). Multiple dynamic representations in the motor cortex during sensorimotor learning. *Nature* 484, 473-478. doi: 10.1038/nature11039

Huber, D., Petreanu, L., Ghitani, N., Ranade, S., Hromádka, T., Mainen, Z., and Svoboda, K. (2008). Sparse optical microstimulation in barrel cortex drives learned behaviour in freely moving mice. *Nature* 451, 61-64. doi:10.1038/nature06445

Igarashi, K. M., Ieki, N., An, M., Yamaguchi, Y., Nagayama, S., Kobayakawa, K., et al. (2012). Parallel mitral and tufted cell pathways route distinct odor information to differ-

ent targets in the olfactory cortex. *J. Neurosci.* 32, 7970–7985. doi: 10.1523/JNEUROSCI.0154-12.2012

Inoue, M., Takeuchi, A., Horigane, S., Ohkura, M., Gengyo-Ando, K., Fujii, H., Kamijo, S., Takemoto-Kimura, S., Kano, M., Nakai, J., Kitamura, K., Bito, H.. (2015). Rational design of a high-affinity, fast, red calcium indicator R-CaMP2. *Nature Methods* 12, 64–70. doi: 10.1038/nmeth.3185

Kandel, E.R., et al (2011). *Principles of neural science* (New York: McGraw-Hill, Health Professions Division).

Kasthuri, N., Hayworth, K. J., Berger, D. R., Schalek, R. L., Conchello, J. A., Knowles-Barley, S., et al. (2015). Saturated reconstruction of a volume of neocortex. *Cell* 162, 648–661. doi: 10.1016/j.cell.2015.06.054

Katona, G., Szalay, G., Maak, P., Kaszas, A., Veress, M., Hillier, D., Chiovini, B., Vizi, E. S., Roska B. & Rozsa B. (2012). Fast two-photon in vivo imaging with three-dimensional random-access scanning in large tissue volumes. *Nat Methods* 9, 201–208. doi: 10.1038/nmeth.1851

Kebschull, J. M., Garcia da Silva, P., Reid, A. P., Peikon, I. D., Albeanu, D. F., and Zador, A. M. (2016). High-throughput mapping of single-neuron projections by sequencing of barcoded RNA. *Neuron* 91, 975–987. doi: 10.1016/j.neuron.2016.07.036

Keemink, S.W., Lowe, S. C., Pakan, J. M. P., Dylida, E., van Rossum M. C. W. & Rochefort N.L. (2018). FISSA: A neuropil decontamination toolbox for calcium imaging signals. *Nature Scientific Reports* 8, 3493 | doi:10.1038/s41598-018-21640-2

Kerlin, A. M., Andermann, M. L., Berezovskii, V. K., Reid, R. C. (2010). Broadly tuned response properties of diverse inhibitory neuron subtypes in mouse visual cortex. *Neuron* 67, 858–871. doi: 10.1016/j.neuron.2010.08.002

Kerr, J.N, Kock, C.P, Greenberg, D.S, Bruno, R.M, Sakmann, B, Helmchen, F. (2007). Spatial organization of neuronal population responses in layer 2/3 of rat barrel cortex. *Journal of Neuroscience* 27, 13316–13328. doi: 10.1523/JNEUROSCI.2210-07.2007

Kerr, J. N. D., Greenberg, D., Helmchen, F. (2005), Imaging input and output of neocortical networks in vivo. *PNAS* 102, 14063–14068. doi: 10.1073/pnas.0506029102

- Kim, U., and Ebner, F. F. (1999). Barrels and septa: separate circuits in rat barrels field cortex. *J. Comp. Neurol.* 408, 489–505. doi: 10.1002/(SICI)1096-9861(19990614)408:4<489::AID-CNE4>3.0.CO;2-E
- Kitamura, K., Judkewitz, B., Kano, M., Denk, W., and Häusser, M. (2008). Targeted patch-clamp recordings and single-cell electroporation of unlabeled neurons in vivo. *Nat. Methods* 5, 61–67. doi: 10.1038/nmeth1150
- Knopfel, T. (2012) Genetically encoded optical indicators for the analysis of neuronal circuits. *Nat Rev Neurosci* 13, 687-700. doi: 10.1038/nrn3293
- König, P., Engel, A.K., and Singer, W. (1996). Integrator or coincidence detector? The role of the cortical neuron revisited. *Trends Neurosci.* 19, 130-137. doi: 10.1016/S0166-2236(96)80019-1
- König K. (2000), Multiphoton microscopy in life sciences. *J Microsc.* 200, 83-104. doi: 10.1046/j.1365-2818.2000.00738.x
- Kopell, N.J., Gritton, H.J., Whittington, M.A., Kramer, M.A. (2014) Beyond the connectome: the dynamome. *Neuron*, 83, 1319–1328. doi: 10.1016/j.neuron.2014.08.016
- Koralek, K. A., Olavarria, J., and Killackey, H. P. (1990). Areal and laminar organization of corticocortical projections in the rat somatosensory cortex. *J. Comp. Neurol.* 299, 133–150. doi: 10.1002/cne.902990202
- Kremer, Y., Léger, J.F., Lapole, R., Honnorat, N., Candela, Y., Dieudonné, S., Bourdieu, L. (2008). A spatio-temporally compensated acousto-optic scanner for two-photon microscopy providing large field of view. *Optics express* 16, 10066-10076. doi: /10.1364/OE.16.010066
- Kremer, Y., Leger, J.-F., Goodman, D., Brette, R., Bourdieu, L. (2011). Late Emergence of the Vibrissa Direction Selectivity Map in the Rat Barrel Cortex. *J. Neurosci.* 31, 10689-10700. doi: 10.1523/JNEUROSCI.6541-10.2011
- Kwon, S. E., Yang, H., Minamisawa, G., and O'Connor, D. H. (2016). Sensory and decision-related activity propagate in a cortical feedback loop during touch perception. *Nat. Neurosci.* 19, 1243–1249. doi: 10.1038/nn.4356
- Larsen, D. D., and Callaway, E. M. (2006). Development of layer-specific axonal arbori-

zations in mouse primary somatosensory cortex. *J. Comp. Neurol.* 494, 398–414. doi: 10.1002/cne.20754

Larsen, D. D., Wickersham, I. R., and Callaway, E. M. (2008). Retrograde tracing with recombinant rabies virus reveals correlations between projection targets and dendritic architecture in layer 5 of mouse barrel cortex. *Front. Neural Circuits* 1:5. doi: 10.3389/neuro.04.005.2007

Lee, S.H, Kwan, A.C, Zhang, S., Phoumthipphavong, V., Flannery, J.G., Masmanidis, S.C., Taniguchi, H., Huang, Z.J., Zhang, F., Boyden, E.S., Deisseroth, K., Dan, Y. (2012) Activation of specific interneurons improves V1 feature selectivity and visual perception. *Nature* 488, 379-383. doi: 10.1038/nature11312

Lefort, S., Tómm, C., Floyd Sarria, J.-C., and Petersen, C.C.H. (2009). The Excitatory Neuronal Network of the C2 Barrel Column in Mouse Primary Somatosensory Cortex. *Neuron* 61, 301-316. doi: 10.1016/j.neuron.2008.12.020

Le Merre, P., Esmaeili, V., Charrière, E., Galan, K., Salin, P.A., Petersen, C.C.H., Crochet, S. (2018). Reward-based learning drives rapid sensory signals in medial pre-frontal cortex and dorsal hippocampus necessary for goal-directed behavior. *Neuron* 97, 83-91. doi: 10.1016/j.neuron.2017.11.031

Li N, Chen TW, Guo ZV, Gerfen CR, Svoboda K. (2015). A motor cortex circuit for motor planning and movement. *Nature* 519:51-56. doi: 10.1038/nature14178

Looger, L.L., and Griesbeck, O. (2011). Genetically encoded neural activity indicators. *Curr. Opin. Neurobiol.* 22, 18-23. doi: 10.1016/j.conb.2011.10.024

Lutcke, H. (2010). Optical recording of neuronal activity with a genetically-encoded calcium indicator in anesthetized and freely moving mice. *Front. Neural Circuits* 4:9. doi: 10.3389/fncir.2010.00009

Lutcke, H., Margolis, D.J., and Helmchen, F. (2013). Steady or changing? Long-term monitoring of neuronal population activity. *Trends Neurosci* 36. 375-384. doi: 10.1016/j.tins.2013.03.008

Madisen, L., Garner, A. R., Shimaoka, D., Chuong, A. S., Klapoetke, N. C., Li, L., et al. (2015). Transgenic mice for intersectional targeting of neural sensors and effectors with

high specificity and performance. *Neuron* 85, 942–958. doi: 10.1016/j.neuron.2015.02.022

Madisen, L., Zwingman, T. A., Sunkin, S. M., Oh, S. W., Zariwala, H. A., Gu, H., et al. (2010). A robust and high-throughput Cre reporting and characterization system for the whole mouse brain. *Nat. Neurosci.* 13, 133–140. doi: 10.1038/nn.2467

Mao, T., Kusefoglou, D., Hooks, B. M., Huber, D., Petreanu, L., and Svoboda, K. (2011). Long-range neuronal circuits underlying the interaction between sensory and motor cortex. *Neuron* 72, 111–123. doi: 10.1016/j.neuron.2011.07.029

Margolis, D.J., Lutcke, H., Schulz, K., Haiss, F., Weber, B., Kugler, S., Hasan, M.T., and Helmchen, F. (2012). Reorganization of cortical population activity imaged throughout long-term sensory deprivation. *Nat. Neurosci.* 15, 1539–1546. doi: 10.1038/nn.3240

Marshel, J. H., Garrett, M. E., Nauhaus, I., and Callaway, E. M. (2011). Functional specialization of seven mouse visual cortical areas. *Neuron* 72, 1040–1054. doi: 10.1016/j.neuron.2011.12.004

Matyas, F., Sreenivasan, V., Marbach, F., Wacongne, C., Barsy, B., (2010). Motor control by sensory cortex. *Science* 330, 1240–43. doi: 10.1126/science.1195797

Mayrhofer, J.M., Skreb, V., von der Behrens, W., Musall, S., Weber, B., and Haiss, F. (2013). Novel two-alternative forced choice paradigm for bilateral vibrotactile whisker frequency discrimination in head-fixed mice and rats. *J. Neurophysiol.* 109, 273–284. doi: 10.1152/jn.00488.2012

Mayrhofer, J.M., Haiss, F., Helmchen, F., Weber, B. (2015) Sparse, reliable, and long-term stable representation of periodic whisker deflections in the mouse barrel cortex. *Neuroimage* 115, 52–63. doi: 10.1016/j.neuroimage.2015.04.045

McCombs, J. E., Palmer, A. E. (2008), Measuring calcium dynamics in living cells with Genetically Encodable Calcium Indicators. *NIH Methods* 46, 152–159. doi: 10.1016/j.ymeth.2008.09.015

Miller, B., Blake, N. M., Erinjeri, J. P., Reistad, C. E., Sexton, T., Admire, P., et al. (2001). Postnatal growth of intrinsic connections in mouse barrel cortex. *J. Comp.*

Neurol. 436, 17–31. doi: 10.1002/cne.1050

Miyawaki, A., Llopis, J., Heim, R., et al. (1997) Fluorescent indicators for Ca²⁺ based on green fluorescent proteins and calmodulin. *Nature* 388, 882-887. doi: 10.1038/42264

Mountcastle, V.B. (1997). The columnar organization of the neocortex. *Brain* 120, 701-722

Narayanan, R. T., Egger, R., Johnson, A. S., Mansvelder, H. D., Sakmann, B., de Kock, C. P., et al. (2015). Beyond columnar organization, cell type- and target layer-specific principles of horizontal axon projection patterns in rat vibrissa cortex. *Cereb. Cortex* 25, 4450-4468. doi: 10.1093/cercor/bhv053

Ni, J., Chen, J. L (2017). Long-range cortical dynamics: a perspective from the mouse sensorimotor whisker system. *European Journal of Neuroscience* 46, 2315-2324. doi.org/10.1111/ejn.13698

Oberlaender, M., Boudewijns, Z. S., Kleele, T., Mansvelder, H. D., Sakmann, B., and de Kock, C. P. (2011). Three-dimensional axon morphologies of individual layer 5 neurons indicate cell type-specific intracortical pathways for whisker motion and touch. *Proc. Natl. Acad. Sci. U.S.A.* 108, 4188–4193. doi: 10.1073/pnas.1100647108

O'Connor DH, Peron SP, Huber D, Svoboda K. (2010). Neural activity in barrel cortex underlying vibrissa-based object localization in mice. *Neuron* 67, 1048-1061. Vibrissa-Based Object Localization in Head-Fixed Mice. *J. Neurosci.* 30, 1947-1967. doi: 10.1016/j.neuron.2010.08.026

O'Connor, D.H., Huber, D., Svoboda, K. (2009). Reverse engineering the mouse brain. *Nature* 461, 923-929. doi: 10.1038/nature08539

O'Connor, D.H., Hires, S.A., Guo, Z.V., Li, N., Yu, J., Sun, Q.Q., Huber, D., and Svoboda, K. (2013) Neural coding during active somatosensation revealed using illusory touch. *Nature neuroscience* 16, 958-965. doi: 10.1038/nn.3419

Oh, S. W., Harris, J. A., Ng, L., Winslow, B., Cain, N., Mihalas, S., et al. (2014). A mesoscale connectome of the mouse brain. *Nature* 508, 207–214. doi: 10.1038/nature13186

Olcese, U., Iurilli, G., and Medini, P. (2013). Cellular and synaptic architecture of multi-

sensory integration in the mouse neocortex. *Neuron* 79, 579–593. doi: 10.1016/j.neuron.2013.06.010

Onativia, J., Schultz, S. R., Dragotti, P. L. (2013). A finite rate of innovation algorithm for fast and accurate spike detection from two-photon calcium imaging. *J. Neural Engineering* 10. doi: 10.1088/1741-2560/10/4/046017

Pala, A., and Petersen, C. C. H. (2015). In vivo measurement of cell-type-specific synaptic connectivity and synaptic transmission in layer 2/3 mouse barrel cortex. *Neuron* 85, 68–75. doi: 10.1016/j.neuron.2014.11.025

Paredes, R.M., Etzler, J.C., Watts, L.T., Zheng, W., Lechleiter, J.D. (2008). Chemical calcium indicators. *Methods* 46, 143–151. doi: 10.1016/j.ymeth.2008.09.025

Paxinos, G., and Franklin, K. (2001). *The Mouse Brain in Stereotaxic Coordinates*, 2nd Edn. San Diego, CA: Academic Press.

Petersen, C. C. H. (2007). The functional organization of the barrel cortex. *Neuron* 56, 339–355. doi: 10.1016/j.neuron.2007.09.017

Peterlin, Z.A., Kozloski, J., Mao, B.Q., Tsiola, A., Yuste R. (2000). Optical probing of neuronal circuits with calcium indicators. *Proc Natl Acad Sci USA* 97, 3619–24. doi: 10.1073/pnas.97.7.3619

Petersen, C. C. H., Grinvald, A., and Sakmann, B. (2003). Spatiotemporal dynamics of sensory responses in layer 2/3 of rat barrel cortex measured in vivo by voltage-sensitive dye imaging combined with whole-cell voltage recordings and neuron reconstructions. *J. Neurosci.* 23, 1298–1309. doi: 10.1523/JNEUROSCI.23-04-01298.2003

Petersen, C.C.H. (2007). The Functional Organization of the Barrel Cortex. *Neuron* 56, 339–355. doi: 10.1016/j.neuron.2007.09.017

Petersen, C.C.H., and Crochet, S. (2013). Synaptic Computation and Sensory Processing in Neo-cortical Layer 2/3. *Neuron* 78, 28–48. doi: 10.1016/j.neuron.2013.03.020

Petreaanu, L., Gutnisky, D. A., Huber, D., Xu N., OConnor, D.H., Tian, L., Looger, L., Svoboda, K. (2012). Activity in motorsensory projections reveals distributed coding in somatosensation. *Nature* 489, 299–303. doi: 10.1038/nature11321

Petreaanu, L., Huber, D., Sobczyk, A., Svoboda, K. (2007). Channelrhodopsin-2-assisted circuit mapping of long-range callosal projections. *Nat. Neurosci.* 10, 663-668. doi: 10.1038/nn1891

Pichon, F., Nikonenko, I., Kraftsik, R., and Welker, E. (2012). Intracortical connectivity of layer VI pyramidal neurons in the somatosensory cortex of normal and barrelless mice. *Eur. J. Neurosci.* 35, 855-869. doi: 10.1111/j.1460-9568.2012.08011.x

Pinault, D. (1996). A novel single-cell staining procedure performed in vivo under electrophysiological control: morpho-functional features of juxtacellularly labeled thalamic cells and other central neurons with biocytin or Neurobiotin. *J. Neurosci. Methods* 65, 113–136. doi: 10.1016/0165-0270(95)00144

Pneumatikakis, E. A., Paninski, L. (2013), Sparse nonnegative deconvolution for compressive calcium imaging: algorithms and phase transitions, *NIPS Proceedings*, Part of: *Advances in Neural Information Processing Systems* 26.

Polley, D.B., Chen-Bee, C.H., and Frostig, R.D. (1999). Two directions of plasticity in the sensory- deprived adult cortex. *Neuron* 24, 623-637. doi: 10.1016/S0896-6273(00)81117-4

Pologruto T.A., Sabatini B.L., Svoboda K. (2003). ScanImage: flexible software for operating laser scanning microscopes. *BioMedical Engineering OnLine*, 2-13. doi: 10.1186/1475-925X-2-13

Purves, D., et al. (2008). *Neuroscience*, 4th Edition. Sinauer Associates.

Reig, R., and Silberberg, G. (2014). Multisensory integration in the mouse striatum. *Neuron* 83, 1200–1212. doi: 10.1016/j.neuron.2014.07.033

Renier, N., Adams, E. L., Kirst, C., Wu, Z., Azevedo, R., Kohl, J., et al. (2016). Mapping of brain activity by automated volume analysis of immediate early genes. *Cell* 165, 1789–1802. doi: 10.1016/j.cell.2016.05.007

Rocheffort, N.L., Jia, H., Konnerth, A. (2008). Calcium imaging in the living brain: prospects for molecular medicine. *Trends Mol. Med.* 14, 389-399. doi: 10.1016/j.molmed.2008.07.005

Roome, C. J., Kuhn, B. (2014). Chronic cranial window with access port for repeated

cellular manipulations, drug application, and electrophysiology. *Frontiers in Cellular Neuroscience* 8, 379. doi: 10.3389/fncel.2014.00379

Sachidhanandam, S., Sreenivasan, V., Kyriakatos, A., Kremer, Y., and Petersen, C.C.H. (2013). Membrane potential correlates of sensory perception in mouse barrel cortex. *Nat. Neurosci.* 16, 1671-1677. doi: 10.1038/nn.3532

Sachidhanandam, S., Sermet, B.S., Petersen, C.C.H. (2016). Parvalbumin-expressing GABAergic neurons in mouse barrel cortex contribute to gating a goal-directed sensorimotor transformation. *Cell Reports* 15, 700-706. doi: 10.1016/j.celrep.2016.03.063

Sage, D., Prodanov, D., Tinevez J.Y., FOx, A., Ablavsky, V. Ortiz, C. (2012) MIJ: A Java package for running ImageJ and Fiji within Matlab. EPFL Biomedical Imaging group

Sato, T.R., Gray, N.W., Mainen, Z.F., Svoboda, K., (2007). The functional microarchitecture of the mouse barrel cortex. *PLoS Biology* 5, 189. doi: 10.1371/journal.pbio.0050189

Sato, T. R., and Svoboda, K. (2010). The functional properties of barrel cortex neurons projecting to the primary motor cortex. *J. Neurosci.* 30, 4256–4260. doi: 10.1523/JNEUROSCI.3774-09.2010

Seiriki, K., Kasai, A., Hashimoto, T., Schulze, W., Niu, M., Yamaguchi, S., et al. (2017). High-speed and scalable whole-brain imaging in rodents and primates. *Neuron* 94, 1085–1100. doi: 10.1016/j.neuron.2017.05.017

Shadlen, M.N., Newsome, W.T. (1994). Noise, neural codes and cortical organization. *Current Opinion in Neurobiology* 4, 569-579.

Shepherd, G.M.G., Svoboda, K. (2005). Laminar and columnar organization of ascending excitatory projections to layer 2/3 pyramidal neurons in rat barrel cortex. *Journal of Neuroscience* 24, 5670-5679. doi: 10.1523/JNEUROSCI.1173-05.2005

Sippy, T., Lapray, D., Crochet, S., and Petersen, C. C. H. (2015). Cell-type-specific sensorimotor processing in striatal projection neurons during goal-directed behavior. *Neuron* 88, 298–305. doi: 10.1016/j.neuron.2015.08.039

- Smetters, D., Majewska, A., Yuste, R. (1999). Detecting action potentials in neuronal populations with calcium imaging. *Methods: A Companion to Methods Enzymol*, 215-221. doi: 10.1006/meth.1999.0774
- Sorensen, S. A., Bernard, A., Menon, V., Royall, J. J., Glattfelder, K. J., Desta, T., et al. (2015). Correlated gene expression and target specificity demonstrate excitatory projection neuron diversity. *Cerebral Cortex* 25, 433–449. doi: 10.1093/cercor/bht243
- Sreenivasan, V., Esmaeili, V., Kiritani, T., Galan, K., Crochet, S., and Petersen, C. C. H. (2016). Movement initiation signals in mouse whisker motor cortex. *Neuron* 92, 1368–1382. doi: 10.1016/j.neuron.2016.12.001
- Stosiek, C., Garaschuk, O., Holthöfer, K., and Konnerth, A. (2003). In vivo two-photon calcium imaging of neuronal networks. *Proc. Natl. Acad. Sci. USA* 100, 7319-7324. doi: 10.1073/pnas.1232232100
- Stüttgen, M.C., Schwarz, C., and Jäkel, F. (2011). Mapping spikes to sensations. *Front. Neurosci.* 5. doi: 10.3389/fnins.2011.00125
- Susaki, E. A., Tainaka, K., Perrin, D., Yukinaga, H., Kuno, A., and Ueda, H. R. (2015). Advanced CUBIC protocols for whole-brain and whole-body clearing and imaging. *Nat. Protoc.* 10, 1709–1727. doi: 10.1038/nprot.2015.085
- Svoboda, K., and Yasuda, R. (2006). Principles of Two-Photon Excitation Microscopy and Its Applications to Neuroscience. *Neuron* 50, 823-839. doi: 10.1016/j.neuron.2006.05.019
- Takehara, H., Nagaoka, A., Nohuchi, J., Akagi, T., Kasai, H., Ichiki, T. (2014). Lab-on-a-brain: Implantable micro-optical fluidic devices for neural cell analysis in vivo. *Sci. Rep.* 4, 6721, doi: 10.1038/srep06721
- Tian, L., Hires, S. A., Mao, T., Huber, D., Chiappe, M. E., Chalasani, S. H., et al. (2009). Imaging neural activity in worms, flies and mice with improved GCaMP calcium indicators. *Nat. Methods* 6, 875-881. doi: 10.1038/nmeth.1398
- Tian, L., Andrew, S., Hires, Looger, L.L. (2012). Imaging Neuronal Activity with Genetically Encoded Calcium Indicators. *Cold Spring Harbor Protoc.* 6, 647-656. doi: 10.1101/pdb.top069609

- Thévenaz, P., Ruttimann, U. E., and Unser, M. (1998). A pyramid approach to subpixel registration based on intensity. *IEEE Trans. Image Process.* 7, 27–41. doi: 10.1109/83.650848
- Tomer, R., Ye, L., Hsueh, B., and Deisseroth, K. (2014). Advanced CLARITY for rapid and high-resolution imaging of intact tissues. *Nat. Protoc.* 9, 1682–1697. doi: 10.1038/nprot.2014.123
- Tsien, R.Y. (1989). Fluorescent probes of cell signaling. *Annu. Rev. Neurosci.* 12, 227–253. doi: 10.1146/annurev.ne.12.030189.001303
- Tsytsarev, V., Pope, D., Pumbo, E., Yablonskii, A., and Hofmann, M. (2010). Study of the cortical representation of whisker directional deflection using voltage-sensitive dye optical imaging. *NeuroImage* 53, 233–238. doi: 10.1016/j.neuroimage.2010.06.022
- Varga, C., Golshani, P., and Soltesz, I. (2012). Frequency-invariant temporal ordering of interneuronal discharges during hippocampal oscillations in awake mice. *Proc. Natl. Acad. Sci. U.S.A.* 109, E2726–E2734. doi: 10.1073/pnas.1210929109
- Veinante, P., and Deschênes, M. (2003). Single-cell study of motor cortex projections to the barrel field in rats. *J. Comp. Neurol.* 464, 98–103. doi: 10.1002/cne.10769
- Veinante, P., Lavallée, P., and Deschênes, M. (2000). Corticothalamic projections from layer 5 of the vibrissal barrel cortex in the rat. *J. Comp. Neurol.* 424, 197–204. doi: 10.1002/1096-9861(20000821)424:2<197::AID-CNE1>3.0.CO;2-6
- Vogelstein, J. T., Packer, A.M., Machado, T. A., Sippy, T., Babadi, B., Yuste, R., Paninski, L. (2010), Fast non-negative deconvolution for spike train inference from population calcium imaging, *J Neurophysiology* 104, 3691–704. doi: 10.1152/jn.01073.2009
- Wang, Q., and Burkhalter, A. (2007). Area map of mouse visual cortex. *J. Comp. Neurol.* 502, 339–357. doi: 10.1002/cne.21286
- Wang, Q., Sporns, O., and Burkhalter, A. (2012). Network analysis of corticocortical connections reveals ventral and dorsal processing streams in mouse visual cortex. *J. Neurosci.* 32, 4386–4399. doi: 10.1523/JNEUROSCI.6063-11.2012

Welker, E., Armstrong-James, M., Bronchti, G., Ourednik, W., Gheorghita-Baechler, F., Dubois, R., et al. (1996). Altered sensory processing in the somatosensory cortex of the mouse mutant barrelless. *Science* 271, 1864–1867. doi: 10.1126/science.271.5257.1864

Welker, E., Hoogland, P. V., and Van der Loos, H. (1988). Organization of feedback and feedforward projections of the barrel cortex: a PHA-L study in the mouse. *Exp. Brain Res.* 73, 411–435. doi: 10.1007/BF00248234

White, E. L., and DeAmicis, R. A. (1977). Afferent and efferent projections of the region of mouse Sml cortex which contains the posteromedial barrel subfield. *J. Comp. Neurol.* 175, 455–482. doi: 10.1002/cne.901750405

Woolsey, T. A., and Van der Loos, H. (1970). The structural organization of layer IV in the somatosensory region (SI) of mouse cerebral cortex. The description of a cortical field composed of discrete cytoarchitectonic units. *Brain Res.* 17, 205–242. doi: 10.1016/0006-8993(70)90079-X

Wu, J., Abdelfattah, A.S., Miraucourt, L.S., Kutsarova, E., Ruangkittisakul, A., Zhou, H., Ballanyi, K., Wicks, G., Drobizhev, M., Rebane, A., Ruthazer, E.S., Campbell, R.E. (2014). A long Stokes shift red fluorescent Ca²⁺ indicator protein for two- photon and ratiometric imaging. *Nature Communications* 5, 5262. doi: 10.1038/ncomms6262

Xu, N.L., Harnett, M.T., Williams, S.R., Huber, D., OConnor, D.H., Svoboda, K., Magee, J.C. (2012) Nonlinear dendritic integration of sensory and motor input during an active sensing task. *Nature* 492, 247-251. doi: 10.1038/nature11601

Yamashita, T., Pala, A., Pedrido, L., Kremer, Y., Welker, E., and Petersen, C. C. H. (2013). Membrane potential dynamics of neocortical projection neurons driving target-specific signals. *Neuron* 80, 1477–1490. doi: 10.1016/j.neuron.2013.10.059

Yamashita, T., and Petersen, C. C. H. (2016). Target-specific membrane potential dynamics of neocortical projection neurons during goal-directed behavior. *Elife* 5:e15798. doi:10.7554/eLife.15798

Yamashita, T., Vavladeli, A., Pala, A., Galan, K., Crochet, S., Petersen, S. S. A., and Petersen, C. C. H. (2018). Diverse Long-Range Axonal Projections of Excitatory Layer

2/3 Neurons in Mouse Barrel Cortex. *Front. Neuroanatomy* 12, 33, doi: 10.3389/fnana.2018.00033

Yang, H., Kwon, S. E., Severson, K. S., and O'Connor, D. H. (2016). Origins of choice-related activity in mouse somatosensory cortex. *Nat. Neurosci.* 19, 127–134. doi: 10.1038/nn.4183

Zakiewicz, I. M., van Dongen, Y. C., Leergaard, T. B., and Bjaalie, J. G. (2011). Workflow and atlas system for brain-wide mapping of axonal connectivity in rat. *PLoS ONE* 6:e22669. doi: 10.1371/journal.pone.0022669

Zeng, H., and Sanes, J. R. (2017). Neuronal cell-type classification: challenges, opportunities and the path forward. *Nat. Rev. Neurosci.* 18, 530–546. doi: 10.1038/nrn.2017.85

Zhang, Z. W., and Deschênes, M. (1997). Intracortical axonal projections of lamina VI cells of the primary somatosensory cortex in the rat: a single-cell labeling study. *J. Neurosci.* 17, 6365–6379. doi: 10.1523/JNEUROSCI.17-16-06365.1997

Zhao, Y., Araki, S., Wu, J., Teramoto, T., Chang, Y.F., Nakano, M., Abdelfattah, A.S., Fujiwara, M., Ishihara, T., Nagai, T., Campbell, R.E. (2011). An expanded palette of genetically encoded Ca²⁺ indicators. *Science* 333, 1888–1891. doi: 10.1126/science.1208592

Zingg, B., Hintiryan, H., Gou, L., Song, M. Y., Bay, M., Bienkowski, M. S., et al. (2014). Neural networks of the mouse neocortex. *Cell* 156, 1096–1111. doi: 10.1016/j.cell.2014.02.023

Curriculum Vitae

Dimitra Angeliki Vavladeli

Contact

Information	Name: Dimitra Angeliki Vavladeli	Voice: +41-76-2197905
	Address: Reusswinkelweg 14	E-mail: aggelvavla@gmail.com
	Zip Code: CH-5620	Citizenship: Greek
	Country: Switzerland	

Education **Ecole Polytechnique Federale de Lausanne (EPFL)**, School of Life Sciences (SV), Brain Mind Institute (BMI), Laboratory of Sensory Processing (LSENS), Lausanne

Ph.D. Neurosciences, started September 2013 - expected defense August 2018

- Thesis Topic: Two-photon calcium imaging of neocortical projection neurons in whisker somatosensory cortex during goal-directed sensorimotor learning
- Advisor: Professor Carl Petersen

University College London (UCL), Department of Mechanical Engineering, London

M.Sc., Biomaterials and Tissue Engineering, September 2011 - September 2012

- Grade: Distinction
- Thesis Topic: A multi-scale bond-graph approach of a comprehensive cardio-respiratory control model using fuzzy-controllers
- Advisor: Professor Vanessa Díaz

National Technical University of Athens (NTUA), School of Applied Mathematics and Physics Sciences, Greece

B.Sc., Physics Engineer, September 2011

- Diploma in Optoelectronics and Laser, Material Mechanics, Grade: 6.89
- Thesis Topic: A finite elements analysis of a constitutive model of cancellous bone under large strains
- or: Professor Dimitrios Eftaxiopoulos

Research Interests

Technical Skills

Extensive hardware and software experience on laser-scanning fluorescence microscopy and in vivo and in-vitro imaging techniques

Microscopy: Two-photon microscopy, confocal microscopy, light microscopy, fluorescent microscopy, chronic time-lapse imaging in-vivo, widefield imaging, intrinsic optical imaging

Animal manipulation: Handling, feeding and brain surgical manipulation of transgenics and wild type mice

Cellular biology: Tracing techniques using either anterograde or retrograde fluorescent compounds (AAV-virus, Retro-virus, CTB, etc.) by in-vivo intracranial injection cranial window implantation

Experimental surgical procedures: Stereotaxic injections in mice of different substances as well as cell and virus, cranial window implantation for long-term imaging of brain function in adult mice, intraperitoneal/subcutaneous/intramuscular injection treatments and trimethoprim for genetic tracing in CRE genetic modified mice

Histology: Whole animal perfusion for brain tissue fixation in mice, vibratome sectioning, staining, mounting

Data Processing: Big data processing techniques and tools, image processing tools and algorithms development, signal processing using Matlab and ImageJ
Instrumentation and Control: LabVIEW, 20Sim, ANSYS

Programming: Matlab, Mathematica, SIDOPs+, Java, FreeFem++, HTML

Applications: LATEX, Microsoft Office, ImageJ, Adobe Photoshop and Illustrator and other common productivity packages for Windows, OS X, and Linux
platforms Operating Systems: Microsoft Windows XP/2000/Vista/7/10, Apple OS X, Linux

Teaching Experience

- *Biomechanics of the Cardiovascular System, teaching assistant, M.Sc in Biomedical Engineering, Prof. Nikolaos Stergiopoulos, February - June, 2014*
- *Neuroscience II: Cellular Mechanisms of Brain Function, teaching assistant, M.Sc in Neuroscience, Prof. Carl Petersen, September - February, 2014-2015*
- *Edx online course: Cellular mechanisms of brain function, teaching assistant, Prof. Carl Petersen, September – February 2015-2016*

<i>Student supervision</i>	<i>Supervision of M.Sc. students on experimental neuroscience and image processing projects</i>
<i>Conferences Participated</i>	<ul style="list-style-type: none"> • <i>The Barrel Cortex Function, 19th - 20th May, 2016</i> <i>VU University Amsterdam, the Netherlands</i> <i>Poster: Two-photon calcium imaging of neocortical projection neurons in mouse whisker primary somatosensory cortex during goal-directed sensorimotor learning</i> • <i>Federation Of European Neuroscience Societies (FENS) 11th Annual meeting, 7th - 11th</i> <i>July, 2018</i> <i>CityCube Berlin, Germany</i> <i>Poster: Two-photon calcium imaging of neocortical projection neurons in whisker somatosensory cortex during goal-directed sensorimotor learning</i>
<i>Publications</i>	<p><i>Vavladeli et al., (2018). Diverse Long-Range Axonal Projections of Excitatory Layer 2/3 Neurons in Mouse Barrel Cortex, Frontiers in Neuroanatomy, Volume 12, Article 33. doi 10.3389/fnana.2018.00033</i></p> <p><i>Vavladeli, A. and Petersen, C. C. H. (In preparation). Two-photon calcium imaging of neocortical projection neurons in mouse whisker primary somatosensory cortex during goal-directed sensorimotor learning</i></p>